Simulation of Photoelectrochemical CO_2 Conversion to Useful Chemicals

Miss Aroonroj Chaosukho

การจำลองกระบวนการแปลงคาร์บอนไดออกไซด์เป็นสารเคมีที่มีประโยชน์ด้วยวิธีไฟฟ้าเคมีทางแสง

น.ส.อรุณโรจน์ เชาว์สุโข

จุฬาลงกรณ์มหาวิทยาลัย

CHULALONGKORN UNIVERSITY

วิทยานิพนธ์นี้เป็นส่วนหนึ่งของการศึกษาตามหลักสูตรปริญญาวิศวกรรมศาสตรมหาบัณฑิต
สาขาวิชาวิศวกรรมเคมี ภาควิชาวิศวกรรมเคมี
คณะวิศวกรรมศาสตร์ จุฬาลงกรณ์มหาวิทยาลัย
ปีการศึกษา 2565

Thesis Title	Simulation of Photoelectrochemical CO$_2$ Conversion to Useful Chemicals
By	Miss Aroonroj Chaosukho
Field of Study	Chemical Engineering
Thesis Advisor	Assistant Professor Paravee Vas-Umnuay, Ph.D.

Accepted by the FACULTY OF ENGINEERING, Chulalongkorn University in Partial Fulfillment of the Requirement for the Master of Engineering

.... Dean of the FACULTY OF ENGINEERING

(Professor SUPOT TEACHAVORASINSKUN)

THESIS COMMITTEE

.... Chairman

(Professor SOORATHEP KHEAWHOM, Ph.D.)

.... Thesis Advisor

(Assistant Professor Paravee Vas-Umnuay, Ph.D.)

.... Examiner

(Assistant Professor Palang Bumroongsakulsawat, Ph.D.)

.... External Examiner

(Assistant Professor Weekit Sirisaksoontorn, Ph.D.)

อรุณโรจน์ เชาว์สุโข : การจำลองกระบวนการแปลงคาร์บอนไดออกไซด์เป็นสารเคมีที่มีประโยชน์ด้วยวิธีไฟฟ้าเคมีทางแสง. (Simulation of Photoelectrochemical CO_2 Conversion to Useful Chemicals) อ.ที่ปรึกษาหลัก : ผศ. ดร.ปารวี วาศน์อำนวย

กระบวนการไฟฟ้าเคมีทางแสงสำหรับปฏิกิริยารีดักชั่น CO_2 (CO_2 reduction reaction: CO_2 RR) เป็นหนึ่งในวิธีที่สามารถนำ CO_2 นำไปใช้ประโยชน์ คาร์บอนมอนอกไซด์ (CO) และฟอร์เมตไอออน (HCOO⁻) เป็นผลิตภัณฑ์ที่น่าสนใจ ที่ได้จาก CO_2 RR ดังนั้นขนาดรูปแบบและจัดเรียงตัวส่วนประกอบของ PEC cell จึงมีบทบาทสำคัญที่ส่งผลต่อประสิทธิภาพของเซลล์และผลผลิตที่ได้จาก CO_2 RR ในงานนี้ ความสัมพันธ์ของอุทกพลศาสตร์ของของไหลและจลนพลศาสตร์ของประจุระหว่างขั้วโฟโตอิเล็กโทรดทางฝั่งแอโนดที่ใช้ TiO_2 เป็นสารกึ่งตัวนำ และขั้วเคาน์เตอร์อิเล็กโทรดทางฝั่งแคโทดที่ใช้ SnO_2 เคลือบบนขั้วที่มีชั้นสำหรับแพร่ก๊าซ (Gas diffusion electrode: GDE) ถูกนำมาศึกษาโดยใช้ COMSOL Multiphysics (5.6) สำหรับเซลล์ไฟฟ้าฟ้าเคมีทางแสงที่มีรูปแบบการจัดเรียงส่วนประกอบที่แตกต่างกัน ภายใต้สภาวะการทำงานเดียวกัน เซลล์ไฟฟ้าฟ้าเคมีทางแสงที่มีรูปแบบ Microfluidic flow cell (MFC) with a zero-gap anode ที่ใช้ค่าสัมบูรณ์ศักย์ไฟฟ้าของเซลล์ 1.5 V และค่าหนาแน่นกระแส 10 A•m^{-2} ที่ขั้วโฟโตอิเล็กโทรดได้ค่าการเลือกเกิดของผลิตภัณฑ์ของ HCOO⁻ เท่ากับ 0.62 ประสิทธิภาพแบบฟาราเดย์ของ HCOO⁻ ร้อยละ 68.6 และประสิทธิภาพทางพลังงานของ HCOO⁻ ร้อยละ 60.4 ดังนั้น MFC with a zero-gap anode เป็นตัวเลือกโมเดลที่ดีที่สุดสำหรับการผลิต เนื่องจากสามารถแก้ไขข้อจำกัดการถ่ายโอนมวลสารและการสูญเสียโอห์มมิก จากการควบครึ่งเซลล์ของรูปแบบ MFC และ Membrane electrode assembly flow cell (MEAFC) นอกจากนี้ผลจากการจำลองยังแสดงว่าที่ ความหนาแน่นกระแส 1.0 mA•cm^{-2} ความยาวเซลล์ (L_{cell}) 1.5 cm ความกว้างของช่องก๊าซ (W_g) 1.5 mm และความกว้างของช่องอิเล็กโทรไลต์ (W_l) 2.0 mm เป็นค่าที่เหมาะสมสำหรับระบบนี้

สาขาวิชา	วิศวกรรมเคมี	ลายมือชื่อนิสิต ....
ปีการศึกษา	2565	ลายมือชื่อ อ.ที่ปรึกษาหลัก ....

6370333021 : MAJOR CHEMICAL ENGINEERING

Aroonroj Chaosukho : Simulation of Photoelectrochemical CO_2 Conversion to Useful Chemicals. Advisor: Asst. Prof. Paravee Vas-Umnuay, Ph.D.

Photoelectrochemical (PEC) CO_2 reduction reaction (CO_2 RR) is one of the possible solutions to reduce CO_2 emissions. Among a variety of products derived from CO_2 RR, CO, and $HCOO^-$ are found to be interesting chemicals. The geometry and arrangement of the main components of PEC cells play important roles in the cell performance of CO_2 RR. In this study, a correlation of hydrodynamics and kinetics on the TiO_2-photoanode and SnO_2-GDE, used as a cathode, was investigated by COMSOL Multiphysics by controlling operating conditions for 2-dimensional different PEC cell configurations. The Microfluidic flow cell (MFC) with a zero-gap anode with a zero-gap anode provided selectivity of 0.62 $HCOO^-$, faradaic efficiency of 68.6% $HCOO^-$, and energy efficiency of 60.4% $HCOO^-$ which were achieved with applied absolute cell voltage at 1.5 V and 1.0 mA•cm^{-2} photocurrent density on the TiO_2 photoanode. Therefore, MFC with a zero-gap anode was chosen as the optimal design overcoming the limitation of mass transfer and ohmic overpotential loss by integrating half-cells of the MFC and membrane electrode assembly flow cell (MEAFC) configurations. Moreover, the results showed 1.0 mA•cm^{-2} of current density, 1.5 cm of cell length (L_{cell}), 1.5 mm of gas channel width (W_g), and 2.0 mm of electrolyte channel width (W_l) which were the optimum values for this system.

Field of Study:	Chemical Engineering	Student's Signature	....
Academic Year:	2022	Advisor's Signature	....

ACKNOWLEDGEMENTS

TABLE OF CONTENTS

จุฬาลงกรณ์มหาวิทยาลัย

CHULALONGKORN UNIVERSITY

LIST OF TABLES

LIST OF FIGURES

Chapter 1

INTRODUCTION

1.1 Background

Global climate change leads to the rise in global temperature caused by the greenhouse effect. The greenhouse effect occurs when greenhouse gases are growing and these gases in the earth's atmosphere trap the sun's heat. Greenhouse gases (GHGs) consist of water vapor, carbon dioxide (CO_2), methane (CH_4), nitrous oxide (N_2O), hydrofluorocarbons (HFCs), perfluorocarbons (PECs), and sulfur hexafluorides (SF_6), respectively. CO_2 is counted as the major concentration of greenhouse gases out of water vapor [1]. CO_2 is emitted from many sources such as fossil fuel combustion for energy conversion and transportation, industrial processes, and land-use change. In the 2010s, the world emitted CO_2 from fuels over 35.13 billion tones each year and now emits over 34 billion tones each year [2]. In addition, the higher dissociation energy for breaking the C=O bond supports the stability of CO_2 molecules, therefore, resulting in the complexity of CO_2 reduction. Chemical products from the CO_2 reduction reaction (CO_2 RR) can be used in various chemical industries and developed into many useful products. Carbon monoxide (CO) and formate ion ($HCOO^-$) can be used in a wide range of applications, for example, CO is used in the Fisher-Tropsch process to produce liquid hydrocarbons, and $HCOO^-$ is used as a material in dyeing and tanning industries. CO and $HCOO^-$ are interesting and useful chemicals from CO_2 RR due to their value growth and market size [3, 4]. To completely overcome the difficult challenge for CO_2 RR, various alternative methods consist of thermochemical, biochemical, electrochemical, photochemical, and photoelectrochemical (PEC) processes. Among these, the PEC process has been used to solve the difficult challenge for CO_2 RR due to the advantages in energy consumption and operating under ambient conditions through the integration of renewable solar energy and external electric field [5].

However, the efficiency of PEC CO_2RR should be concerned for PEC cells design through many effects such as light intensity, operating mode (batch system and continuous flow system), operating conditions (temperature, pressure, flow rate, and cell voltage), bandgap (type of semiconductors), pH (type of electrolyte), product separator (type of ion-exchange membrane), and cell configurations. The PEC cell configurations refer to the main components consisting of photoelectrode, counter-electrode, electrolyte, and product membrane. The geometric configuration and arrangement of these components have been simulated to observe the performance and productivity of CO_2RR [6, 7]. B. Endrodi et al. [8] showed zero-gap membrane electrolyzer cells for CO_2 RR through a multilayer CO_2 electrolyzer stack. The electrolyzer cell was an arrangement of gas diffusion electrode (GDE), anode catalyst layer (ACL), bipolar plate (BPP), and an anion exchange membrane (AEM) in sequence. The pressurized CO_2 gas feed and GDEs were applied in a continuous flow electrolyzer to solve the low solubility of CO_2 and offer a high surface area for CO_2 RR. Therefore, direct-fed CO_2 gas in parallel to a multilayer electrolyzer stack could improve about 95% faradaic efficiency (FE) of CO formation in which a partial current density of CO could be up to 300 mA cm^{-2}. In addition, the efficiency of CO_2 conversion was increased up to 40% when the arrangement of multilayer CO_2 electrolyzer stacked in the series direction due to off-gas (remnant CO_2 reactant) was continued flew to sequence layers.

To demonstrate the performance and productivity of CO_2 RR, through the PEC cells, the PEC cells were designed and arranged in different configurations namely 1) microfluidic flow cell (MFC), 2) membrane electrode assembly flow cell (MEAFC), and 3) microfluidic flow cell (MFC) with a zero-gap anode. These configurations were simulated under identical operating conditions. Besides, the optimum geometric configurations of the main components were also identified through simulation. The results are shown through CO_2 conversion, selectivity,

faradaic efficiency (FE), and the energy efficiency (EE) of products as the performance indicators of the PEC process of CO_2RR.

1.2 Objectives

1. To study computational modeling of the PEC process of CO_2 RR to produce CO and $HCOO^-$ using COMSOL Multiphysics (5.6).

2. To investigate and compare the effects of different configurations of PEC cells through behaviors of CO_2 conversion, selectivity, faradaic efficiency, and the energy efficiency of CO_2 RR to CO and $HCOO^-$ when operating under identical conditions.

1.3 Scopes of research

COMSOL Multiphysics (5.6) was used to model and simulate the PEC process for CO_2 RR to CO and $HCOO^-$. The model was assumed to be operated at a steady-state condition. Both gas and liquid feeds were treated as ideal and incompressible fluids transported through diffusion and convection. In addition, the model was validated with a system that has similar conditions through the previous research papers.

1.3.1 Controlled variables

The main components were specified for PEC CO_2 RR to obtain selected products under ambient operating conditions, and GDEs were applied for two electrodes. The n-type semiconductor or titanium dioxide (TiO_2) was used as a photocatalyst for back-illumination of the photoanode compartment while tin (IV) oxide (SnO_2) was used as an electrocatalyst for CO_2 RR of the cathode compartment, respectively. The Nafion-117 was used as a proton exchange membrane (PEM) to separate the PEC cell and transfer protons (H^+) from the anodic to the cathodic compartment. The anolyte and catholyte channels were fed with potassium hydroxide KOH) and potassium bicarbonate ($KHCO_3$) under a controlled concentration and flow rate to sustain the pH of the system. The supplied energy for

CO_2 RR was controlled through applied photocurrent density to overcome the thermodynamics of CO_2 RR.

1.3.2 The 2-dimensional model of PEC cell configurations

The main components with the specific thickness of the PCE cell were arranged in the x-direction with different positions. The 2-dimensional model of the PEC cell was operated under a continuous flow of reactants and electrolytes that entered from bottom to top in the y-direction in laminar flow. The description of different configurations of PCE cells are designed namely as follows: microfluidic flow cell (MFC), 2) membrane electrode assembly flow cell (MEAFC), and 3) microfluidic flow cell (MFC) with a zero-gap anode as shown in figure 1.
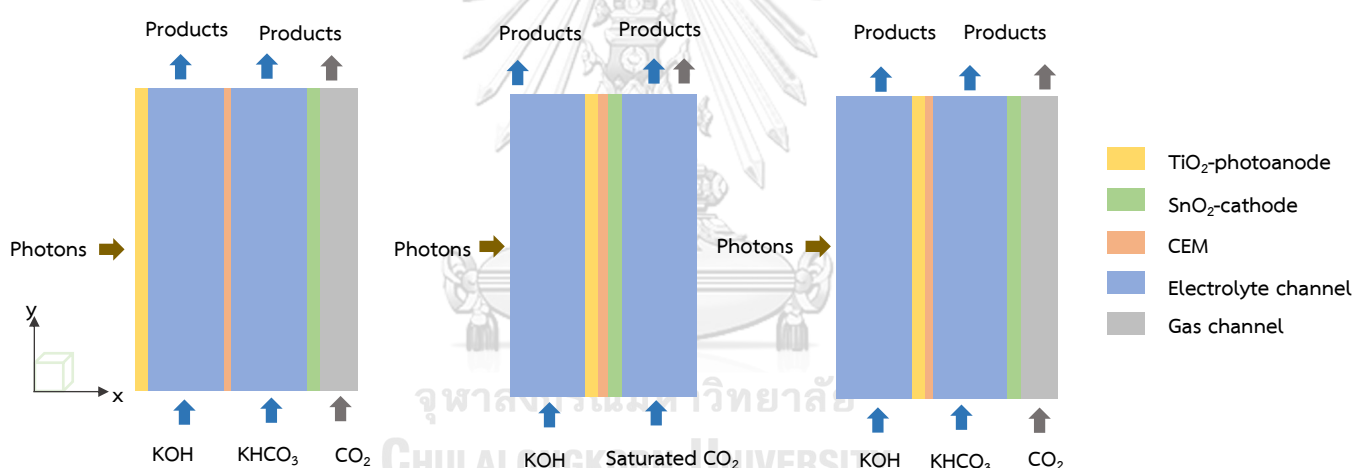
Figure 1. Diagram of different PEC cell for CO_2 RR.

1. Microfluidic flow cell (MFC)

The 6 domains of MFC were assembled from left to right side in x-direction including TiO_2-photoanode, anolyte channel, PEM, catholyte channel, SnO_2-cathode, and gas channel, respectively. CO_2 in the gas phase was fed to SnO_2-cathode through the gas feed channel while KOH and $KHCO_3$ were fed in the anolyte and catholyte channels, respectively. The compartment between the anode and the cathode was inserted using PEM to prevent the crossing over of the products in PEC cells.

2. Membrane electrode assembly flow cell (MEAFC)

The 5 domains of MEAFC were assembled from left to right side in x-direction including the anolyte channel, TiO_2-photoanode, membrane, SnO_2-cathode, and catholyte channel respectively. Saturated CO_2 and $KHCO_3$ were fed to the catholyte channel while KOH was fed to the anolyte channel. The compartment between the anode and the cathode was inserted using PEM to prevent the crossing over of the products in PEC cells.

3. Microfluidic flow cell (MFC) a zero-gap anode

The 6 domains of MFC with a zero-gap anode were assembled from left to right side in x-direction including the anolyte channel, TiO_2-photoanode, membrane, catholyte channel, SnO_2-cathode, and gas channel, respectively. CO_2 in the gas phase was fed to SnO_2-cathode through the gas feed channel while KOH and $KHCO_3$ were fed in the anolyte and catholyte channels, respectively. The compartment between the anode and the cathode was inserted using PEM to prevent the crossing over of the products in PEC cells.

1.3.3 Performance indicators

1. CO_2 conversion (X_{CO_2})

CO_2 conversion is defined as a ratio of the amount of CO_2 reactant that can be reacted to chemical products to the amount of CO_2 reactant.

2. Selectivity (S)

Selectivity is the number of moles of interested product formed per the number of moles of overall products formed.

3. Faradaic efficiency (FE)

FE represents the amount of fuel consumption with the amount of obtained current. The FE for PEC CO_2 reduction can be defined as a ratio of the current that promotes CO_2 conversion into chemical fuels to the received current.

4. Energy efficiency (EE)

        EE is the amount of the electric energy that is supplied to the cell for interested product formation.

1.3.4 Variables affecting PEC cell for CO_2 RR

In order to study variables affecting system efficiency, the physics models in the simulation were used to evaluate the variation of the factors that affecting PEC cell for CO_2 RR.

1. Physics model validation

        To validate the accuracy of physics model for simulation, the correlation of FE and absolute cell voltage curve which absolute cell voltage was varied between 1.5 – 3.5 V.

2. Arrangement of PEC cell configuration

        To evaluate the effect of arrangement of PEC cell on cell performance, the different PEC cell configurations consist of MFC, MEAFC, and MFC with a zero-gap anode were simulated under specific controlled variables.

3. Light intensity

        To evaluate the effect of energy consumption on cell performance, light intensity ($mW \cdot cm^{-2}$) was applied in a form of photocurrent density of 0.1, 0.5, 1.0, 5.0, 10.0, and 15.0 $mA \cdot cm^{-2}$ with specific boundary electric potential initial value.

4. PCE cell length

        To evaluate the effect of surface area of PEC cell on cell performance, PEC cell lengths of 1.0, 1.5, 3.0, 4.0, 6.0, 8.0, and 10.0 cm were varied with specific controlled PEC cell height.

5. Gas channel width

    To evaluate the effect of geometric configuration of PEC cell on cell performance, gas channel widths of 1.0, 1.5, 2.0, 3.0, 4.0, 5.0, 6.0 and 8.0 mm were varied with specific controlled surface area of PEC cell.

6. Electrolyte channel width

    To evaluate the effect of geometric configuration of PEC cell on cell performance, electrolyte channel widths of 1.0, 1.5, 2.0, 3.0, 4.0, 5.0, 6.0 and 8.0 mm were varied with specific controlled surface area of PEC cell.

1.4 Expect outputs

1. Apply conservative equation and kinetics expression of the PEC process for CO_2 RR to CO and $HCOO^-$ in computational modeling through COMSOL Multiphysics (5.6).

2. Evaluate domination of each PEC cell configuration by using CO_2 conversion, selectivity, faradaic efficiency, and energy efficiency behaviors from the PEC process of CO_2 RR to CO and $HCOO^-$.

3. Apply optimum PEC cell configuration for scaling up in CO_2 conversion industries.

Chapter 2

THEORETICAL BACKGROUND AND LITERATURE REVIEW

2.1 Global climate change and greenhouse gases

Global climate change can be measured from the climate over a long period which results from an increase in greenhouse gases in the atmosphere. Global climate change and greenhouse gases are the important data that should be concerned.

2.1.1 Global climate change
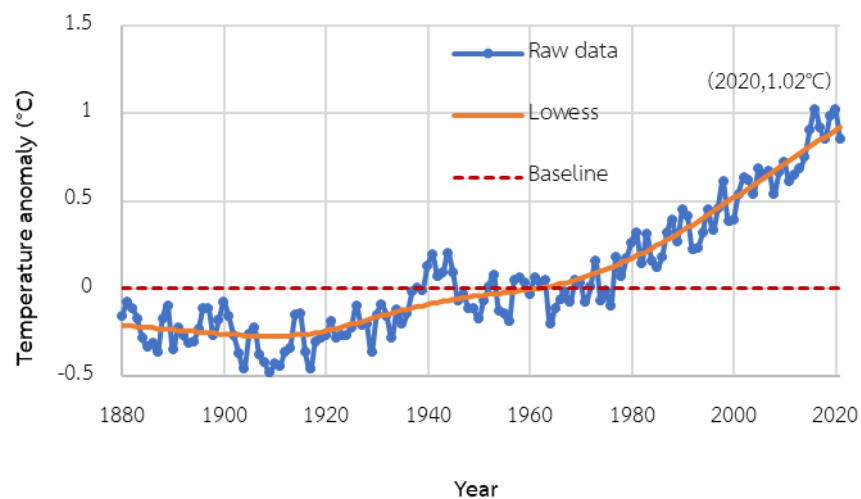
Figure 2. The annual global temperature anomaly (℃) [9].

Global climate change refers to a weather variation in the long-term initiated by the greenhouse effect and the increase of greenhouse gases (GHGs). The effect of global climate change can lead to many phenomena, in which the different forms of warning signs had been occurring such as higher sea levels, algal blooms, wildfire, and air pollution [10].

From figure 2, the NASA Goddard Institute for Space Studies (GISS) collected global temperature to perform a model of surface temperature analysis (GISTEMP v4) and estimated annual global surface temperature anomalies, in which the optimum baseline period of temperature from 1951 to 1980 is fixed, referred from NASA's analysis. The global surface temperature variation was plotted through raw data and

locally weighted scatterplot smoothing (Lowess) data to observe the trend of temperature anomaly. In 2016 and 2020, maximum temperature anomalies could increase to 1 degree celsius, which was the highest record since the industrial revolution in 1980. Moreover, the trend of global temperature anomaly is still increasing at present [9].

2.1.2 Greenhouse gases

The GHGs are gases existing in the atmosphere that can trap and emit heat in the infrared range. Although the optimum existence of GHGs promotes warming on the earth's surface to maintain temperature and prevent our life from dangerous solar radiation, excess concentration of GHGs causes an important role in global climate change. The major GHGs include water vapor, carbon dioxide (CO_2), methane (CH_4), nitrous oxides (NO_x), hydrofluorocarbons (HFCs), perfluorocarbons (PECs), and sulfur hexafluoride (SF_6) [11].
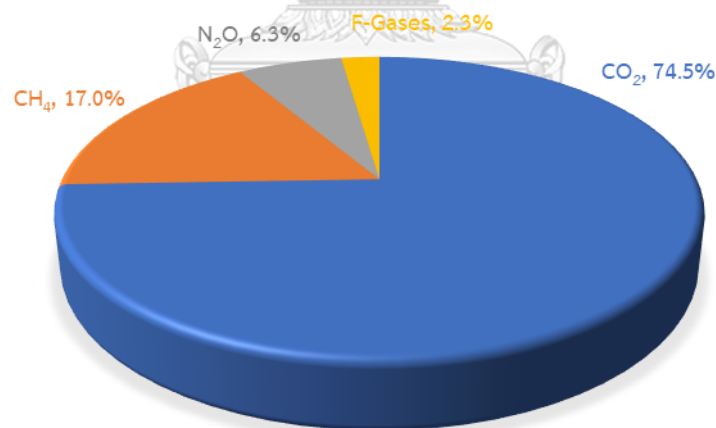
Figure 3. World greenhouse gas emission in 2018 [12].

From figure 3, the total GHGs emission in 2018 was estimated at 48.9 Gt CO_2eq which emission of each gas can be represented by using CO_2eq or carbon dioxide equivalents multiply by its 100-year global warming potential (GWP) value. Among the GHGs, the amount of CO_2 emission is around 36.4 Gt CO_2eq or 74.5% of GHGs emissions [13].

2.2 CO_2

Due to CO_2 being the major gas of GHGs that is causing global warming, CO_2 emission also relates to the concentration GHGs in the atmosphere. Therefore, the properties of CO_2 are studied to define the optimum strategies for CO_2 reduction.

2.2.1 CO_2 Emission

In 2020, the trend of the amount of global CO_2 emission from fuels decreased because the COVID-19 pandemic has impacted global economic activities. However, the overall trend of global CO_2 emission from fuels has increased, reaching 34 billion tons per year as shown in figure 4 [2].
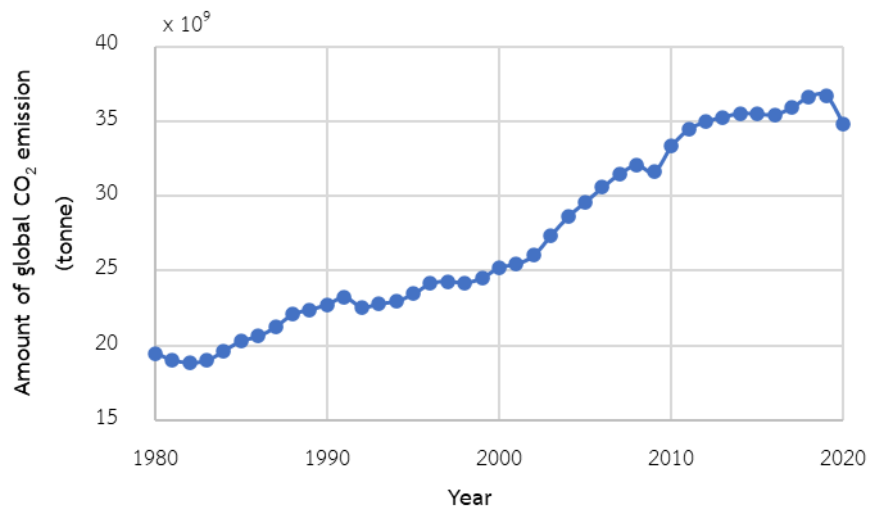
Figure 4. Global CO_2 emission from fossil fuels [2].
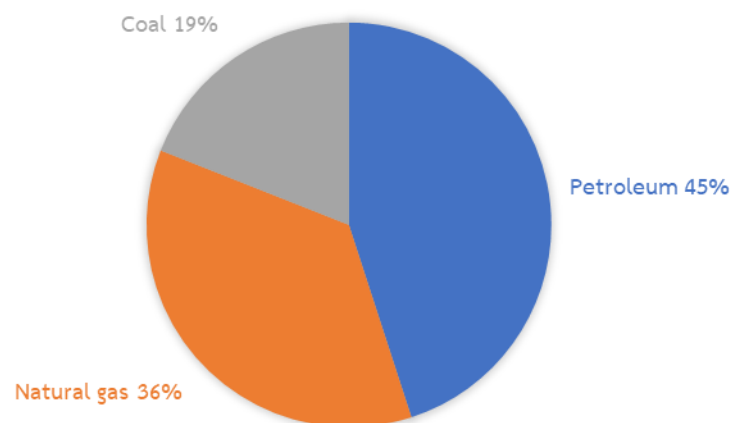
Figure 5. U.S. energy-related CO_2 emissions by source in 2020 [14].
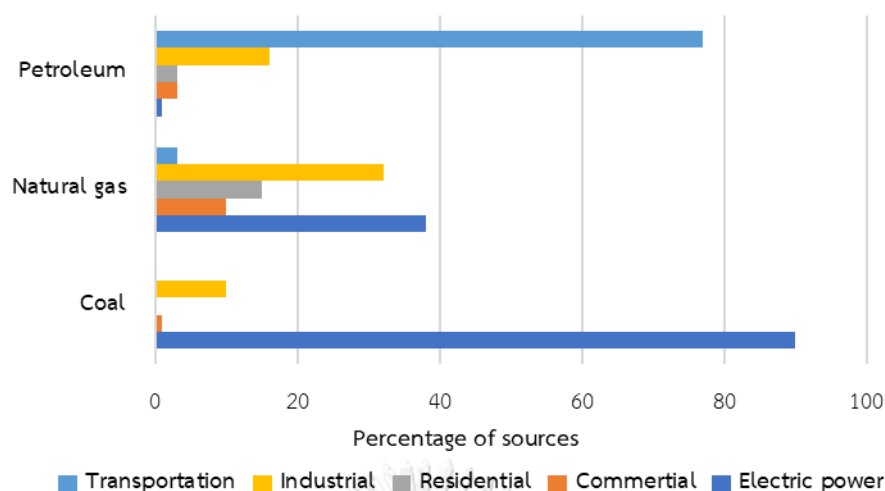
Figure 6. U.S. CO_2 emissions from energy consumption by source and sector in 2020 [15].

The U.S. energy information administration [14] shows the total amount of total annual U.S. energy-related CO_2 emission in 2020 was 4,571 million metric tons. The primary source of CO_2 emissions could be obtained from fossil fuel combustion derived from petroleum, natural gas, and coal. The fraction of fossil fuel as shown in figure 5.

Moreover, figure 6 presents the fraction of end-use sectors provided by fossil fuel combustion including non-electric power and electric power sectors. Non-electric power was used in many human activities consisting of transportation, industrial, residential, and commercial [15].

2.2.2 Properties of CO_2

Carbon dioxide (CO_2) is a chemical compound that covalent bonding of two atoms of oxygen with one atom of carbon. The stability of CO_2 molecules is presented because double bonds of compound (O=C=O) provide symmetric structure and 8 valence electrons of carbon follow Octet's rule. The dissociation energy for breaking the C=O bond (~750 kJ mol^{-1}) is higher than other chemical bonding such as the C-H bond (~430 kJ mol^{-1}) and the C-C bond (~336 kJ mol^{-1}) resulting in high energy consumption is required. In addition, CO_2 is a gas at normal

temperature and pressure due to the nonpolar properties of molecules. Therefore, high barriers of properties and low solubility of CO_2 can inherent CO_2 conversion to value-added products [4, 16].

The chemical products derived from the highest chemical state (+4) of carbon atom in CO_2 reduction such as carbon monoxide (CO), formic acid (HCOOH), formaldehyde (CH_2O), methanol (CH_3OH), and methane (CH_4) indicate the higher positive value of $\Delta G°$ when compared with water splitting reaction which is shown in table 1.

Table 1. Some of the possible thermodynamic reactions of CO_2 reduction, the standard enthalpy ($\Delta H°$), Gibbs free energy ($\Delta G°$), and redox potential (E°) [4, 5].

Reaction	$\Delta H°$ (kJ mol^{-1})	ΔG (kJ mol^{-1})	$\Delta E°$ (V)
$H_2O(l) \rightarrow H_2(g) + 1/2O_2(g)$	286	237	1.23
$CO_2(g) \rightarrow CO(g) + 1/2\ O_2(g)$	283	257	1.33
$CO_2(g) + H_2O(l) \rightarrow HCOOH(l) + 1/2O_2(g)$	270	286	1.48
$CO_2(g) + H_2O(l) \rightarrow CH_2O(l) + O_2(g)$	563	522	1.35
$CO_2(g) + 2H_2O(l) \rightarrow CH_3OH(l) + 3/2O_2(g)$	727	703	1.21
$CO_2(g) + 2H_2O(l) \rightarrow CH_4(g) + 2O_2(g)$	890	818	1.06

The relation between standard Gibbs free energy change ($\Delta G°$) and the standard cell potential ($\Delta E°$) of reduction reaction can be identified by using Eq. (1) [4].

$$\Delta E° = -\frac{\Delta G°}{n F}$$
Eq. (1)

where $\Delta E°$ is the standard cell potential derived from the difference of standard

potential between two $\left(\Delta E° = E_1° - E_2°\right)$ (V)

$\Delta G°$ is the standard Gibbs free energy change

n is the number of electrons transferred for the balanced redox couple

F is the Faraday constant (coulombs mol^{-1})

The higher positive value of ΔG° presents more endothermic reaction, the reaction of CO_2 reduction to CH_3OH and CH_4 that are hydrocarbon fuels have highly endothermic status when compared with water-splitting reaction. Hence, conclude that CO_2 RR is more thermodynamically unfavorable at ambient temperature.

Therefore, the effect of thermodynamic reactions of CO_2 reduction is concerned to design the optimum operating conditions for specified products. Tables 2 and 3 show redox potentials of CO_2 RR to some of the possible value-added products that were evaluated under room temperature, 1 atm for gases, and activity of 1 for the solute.

Table 2. Some of the possible products and thermodynamics of water splitting reaction and CO_2 RR, standard electrode potentials (E°) based on normal hydrogen electrode (NHE) at pH=7 [4].

Reaction	Products	ΔE° (V) vs. NHE at pH7
$2H^+ + 2e^- \rightarrow H_2$	Hydrogen	-0.41
$H_2O + 2h^+ \rightarrow 1/2O_2 + 2H^+$	Oxygen	0.82
$CO_2 + e^- \rightarrow CO_2^{\bullet-}$	$CO_2^{\bullet-}$ intermediate	-1.9
$CO_2 + 2H^+ + 2e^- \rightarrow CO + H_2O$	Carbon monoxide	-0.53
$CO_2 + 2H^+ + 2e^- \rightarrow HCOOH$	Formic acid	-0.61
$CO_2 + 4H^+ + 4e^- \rightarrow CH_2O + H_2O$	Formaldehyde	-0.48
$CO_2 + 6H^+ + 6e^- \rightarrow CH_3OH + H_2O$	Methanol	-0.38
$CO_2 + 8H^+ + 8e^- \rightarrow CH_4 + 2H_2O$	Methane	-0.21

Table 3. Some of the possible products and thermodynamic half-reaction of CO_2 RR, standard electrode potentials (E°) based on standard hydrogen electrode (SHE) at pH=7 [17].

Half-reaction of CO_2 reaction	Products	E° (V) vs. SHE at pH7
$CO_2(g) + H_2O(l) + 2e^- = CO(g) + 2OH^-$	Carbon monoxide	-0.520
$CO_2(g) + 2H_2O(l) + 2e^- = HCOOH(l) + 2OH^-$	Formic acid	-0.610
$CO_2(g) + 3H_2O(l) + 4e^- = CH_2O(l) + 4OH^-$	Formaldehyde	-0.480
$CO_2(g) + 5H_2O(l) + 6e^- = CH_3OH(l) + 6OH^-$	Methanol	-0.380
$CO_2(g) + 6H_2O(l) + 8e^- = CH_4(g) + 8OH^-$	Methane	-0.240
$2CO_2(g) + 10H_2O(l) + 14e^- = C_2H_6(g) + 14OH^-$	Ethane	-0.270
$2CO_2(g) + 9H_2O(l) + 12e^- = C_2H_5OH(l) + 12OH^-$	Ethanol	-0.33
$2CO_2(g) + 8H_2O(l) + 12e^- = C_2H_4(g) + 12OH^-$	Ethylene	-0.34
$3CO_2(g) + 13H_2O(l) + 18e^- = C_3H_7OH(l) + 18OH^-$	Propanol	-0.320

The reference electrode potentials of half-reactions can be mentioned as a hydrogen electrode that provides a normal hydrogen electrode (NHE) and a standard hydrogen electrode (SHE). The platinum (Pt) electrode is used for both referenced electrodes, but the difference between NHE and SHE is based on potential measurement in a specified solution. While NHE measures potential in 1 N (normal concentration, for protons: 1 N = 1 M) acid solution, SHE measures potential in an ideal solution. However, SHE can be concluded current standard of zero potential because temperature variation is constant [18].

The first procedure of CO_2 RR is a reduction of one electron to $CO_2^{\bullet-}$ intermediate that has the highest negative E° (-1.9 V vs. NHE at pH=7) and is often investigated in this procedure as a rate-limiting step. To convert CO_2 to a particular product, excess voltage than E° or energy input is required to activate the reaction. The role of redox potentials from half-reactions in tables 2 and 3 is represented by the minimum voltages for CO_2 RR motivation.

Although the specific reactions are achievements, high-efficiency catalysts are desired because multielectron transfer suppresses the selectivity of value-added products [3, 17].

2.2.3 Chemical products from CO_2 RR

The economic analysis is considered to manage significant problems from the previous section, including the large redox potential of one electron to $CO_2^{\cdot-}$ intermediate and multielectron transfer. The economic analysis relates to operating costs and earnings from the production process. Table 4 shows the estimated market price, market size, and annual global production in USD: United States Dollars [3].

จุฬาลงกรณ์มหาวิทยาลัย

CHULALONGKORN UNIVERSITY

Table 4. Estimated market price (in USD/kg), normalized price (in USD/electron), market size (in USD/year), and annual global production (in million tons of CO_2/year; Mtons) of major CO_2 reduction products [19, 20].

Products	Number of required electrons	Market price ($/kg)	Normalized price ($/electron) x 10^3	Estimate market size ($/year)	Global production (Mtons/year)
Carbon monoxide (syngas, CO)	2	0.06	0.8	2.7-3.2	150.0
Carbon monoxide (CO)	2	0.6	8.0	-	-
Formic acid (HCOOH)	2	0.74	16.1	0.62	0.6
Methanol (CH_3OH)	6	0.58	3.1	54	110.0
Methane (CH_4)	8	0.18	0.4	-	250.0
Ethylene (C_2H_4)	12	1.30	3.0	155-248	140.0
Ethanol (CH_3CH_2OH)	12	1.00	3.8	-	77.0
N-propanol ($CH_3CH_2CH_2OH$)	18	1.43	4.8	-	0.2

Table 5. Some applications of major CO_2 reduction products [3, 20].

Products	Applications
Carbon monoxide (CO)	- Fuels and fuel additives - Plasticizer
Formic acid (HCOOH)/Formate (HCOO⁻)	- Food additives - Bleaching agent
Methanol (CH_3OH)	- Fuel and fuel additives - Plastics industry
Methane (CH_4)	- Fuels and fuel additives - Hydrogen production
Ethylene (C_2H_4)	- Precursor to polymers - Petroleum production
Ethanol (CH_3CH_2OH)	- Fuels and related products - Medical antiseptic, beverage
N-propanol ($CH_3CH_2CH_2OH$)	- Fuels and fuel additives - Paint and coating additives

From tables 4 and 5, CO and HCOOH/ HCOO⁻ are interesting products because of their market growth rate and a variety of applications. Technavio [21] presented the global carbon monoxide alarm market from 2021 to 2025 which end-user includes industrial, commercial, and residential. The compound annual growth rate (CAGR) of the carbon monoxide alarm market from 2021 to 2025 is almost 8%. Besides, the incremental growth is predicted to be $305.50 million. CO is also known as a key reaction intermediate on the route to C_{2+} compounds which CO can be used in many applications such as fuel gas mixture with hydrogen for industrial, production of various chemicals (acids, esters, and alcohols) [22]. Likewise, as per Fact.MR [23] offered the global market research for the compound annual growth rate (CAGR) of formic acid from 2021 to 2031 equals 4%. The market size value of formic acid in 2020 was informed at $1.5 billion and in 2031 is estimated to be $3 billion. HCOOH/HCOO⁻ can be used in many applications such as the

pharmaceutical industry, textile industry, rubber production, and animal feed. Moreover, HCOOH/ HCOO$^-$ is widely used as a catalyst in the production of various chemicals.

2.3 Strategies of CO$_2$ utilization

Many strategies for CO$_2$ conversion were developed due to the increase in CO$_2$ concentration which is the major fraction of GHGs. The obstacle in thermodynamic and kinetic properties of CO$_2$ molecules leads chemical and physical routes to be applied to utilized CO$_2$ materials. In this study, chemical routes are concerned wherewith CO$_2$ is direct conversed. Many chemical routes have been studied that are related to thermochemical, biochemical, electrochemical, and photoelectrochemical [5].

2.3.1 Thermochemical CO$_2$ conversion
1. Hydrogenation technology

The hydrogenation technology is the major destination of thermochemical CO$_2$ conversions, H$_2$ is used as a co-reactant to reduce stable molecules like CO$_2$. A large amount of energy input is also acquired to provide value-added products such as CO, CH$_3$OH, CH$_4$, and C$_{2+}$ at relatively low temperatures (≤523 K) [24].

Methanol (CH$_3$OH) is widely used as fuel for internal combustion so increasing demand in the global market occurs. However, a suitable catalyst is required to define strong equilibrium limitations by 220-250 °C to produce CH$_3$OH via thermal CO$_2$ hydrogenation operating under high pressure of syngas (50-100 bars) which shows in reaction (1) [25].

$$CO_2 + 3H_2 \rightarrow CH_3OH + H_2O, \Delta H°_{298K} = -49.8 \text{ kJ/mol} \qquad (1)$$
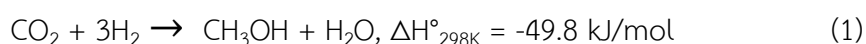
X. Jiang et al. [26] presented the progress of CO$_2$ hydrogenation to CH$_3$OH through heterogeneous catalysis. The catalytic performance and long-term stability are represented as performance indicators of diverse catalysts consisting of metals, metal oxides, and intermetallic compounds. Moreover, mechanics and kinetics are

investigated to realize the importance of catalysts on CO_2 hydrogenation to the CH_3OH process.

2. Reforming technology

Thermochemical for reforming CO_2 to syngas (mixture of H_2 and CO) is a high-cost technique because the rare metals consisting of Pt, Pd, Ir, Rh, Ru, Co, and Ni are used to catalyze the methanation of syngas after CO_2 and CH_4 are adsorbed that still sought high temperature to thermodynamically unfavorable of CO_2 molecules which shows in reaction (2) [27, 28].

$$CH_4 + CO_2 \leftrightarrow 2CO + 2H_2, \Delta H°_{298K} = +247 \text{ kJ/mol} \tag{2}$$

CO_2 is consumed as an oxidizing agent in the dry methane reforming process. However, this process still has significant problems such as low selectivity and the deactivation of catalysts from coke deposition which is shown in reaction (3) methane cracking and (4) reverse boundary reaction [27, 28].

$$CH_4 \leftrightarrow C + 2H_2, \Delta H°_{298K} = +74.9 \text{ kJ/mol} \tag{3}$$

$$2CO \leftrightarrow C + CO_2, \Delta H°_{298K} = -172.4 \text{ kJ/mol} \tag{4}$$
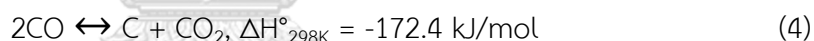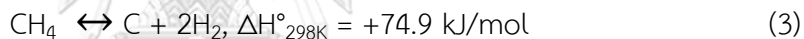
Apart from applying proper catalysts that have good performance for operating at high-temperature conditions, solar energy could be used to solve a large amount of energy input. The tri-reforming process integrated methane steam reforming in reaction (5), methane partial oxidation in reactions (6) to (7), and CO_2 reforming of methane, there are other alternatives to avoid coke deposition for the methanation process [29].

$$CH_4 + HO_2 \leftrightarrow CO + 3H_2, \Delta H°_{298K} = +206 \text{ kJ/mol} \tag{5}$$

$$CH_4 + 0.5O_2 \leftrightarrow CO + 2H_2, \Delta H°_{298K} = -36 \text{ kJ/mol} \tag{6}$$

$$CH_4 + 2O_2 \leftrightarrow CO_2 + 2H_2O, \Delta H°_{298K} = -880 \text{ kJ/mol} \tag{7}$$
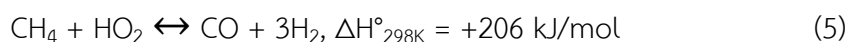
P. Livingston et al. [30] proffered a technology to reduce CO_2 through gamma radiation. The CO_2 was pressed underground in the deep wells, then liquid with high pressure was injected. This technology is environmentally friendly for CO production, reduction of fossil fuels consumption, and prevention of the deposited problem.

Nevertheless, economics and safety are considered more studied because H_2 is used as a reductant so fractional distillation is required to recover the valuable feedstock chemical and a fully instrumented cooling pond is required to support radiation safety.

3. Mineralization technology

The CO_2-mineralization technology produces carbonates through the reaction between CO_2 with alkaline-earth metals for example calcium oxide (CaO) and magnesium oxide (MgO) that is major fractions of industrial solid waste (ISW). Natural minerals and industrial solid waste (ISW) such as coal fly ash, steel slag, phosphogypsum, and blast furnace slag are utilized as raw materials for CO_2 mineralization technology.

$$(Ca,Mg)SiO_3 \text{ (s)} + CO_2 \text{ (g)} \rightarrow (Ca,Mg)CO_3 \text{ (s)} + SiO_2 \qquad (8)$$

From mineral carbonation reaction (8) is a spontaneous exothermic and thermodynamically favorable process. To produce carbonates, silicate rocks are often employed as host rocks since provide a less reasonable cost for the products separation unit. At present, CO_2 mineralization has been achieved in the laboratory through the injection of CO_2 to host rock at ambient temperature and pressure. Moreover, the possibility and long-term sustainability are needed to be studied to scale up for mineral carbonation [31, 32].

2.3.2 Electrochemical CO_2 conversion

The electrochemical technology is widely used in the water-splitting and CO_2 RR where the reaction occurs at the interface of electrode/electrolyte. To drive the thermodynamically stable molecule of CO_2, the electrochemical CO_2 RR required an electrolyte as a proton donor a suitable electrocatalyst that is deposited on the electrode surface and an external electric field that is overpotential for a specific reaction. Besides, an ion-exchange membrane may assemble between two electrodes as a separator unit of products [5].

When CO_2 molecules are adsorbed on the working electrode, the structure of linear CO_2 molecules is reformed to active form due to sluggish kinetics of electrochemical reduction. Also, reformation of CO_2 structure will produce overpotential on first electron transfer motivation. Electrocatalysts still have been studied to improve the selectivity of CO_2 electrochemical reduction. X. Chang et al. [33] proposed that apart from Cu used as an electrocatalyst for CO production, many electrocatalysts were examined namely metals (Sn, Pd, Cu, Pt, etc.), layered transition metal dichalcogenides (WS_2, $MoSe_2$, and MoS_2), and heteroatom-functionalized carbonaceous catalysts (N-doped carbon nanofibers and graphene quantum dots).

2.3.3 Photoelectrochemical CO_2 conversion
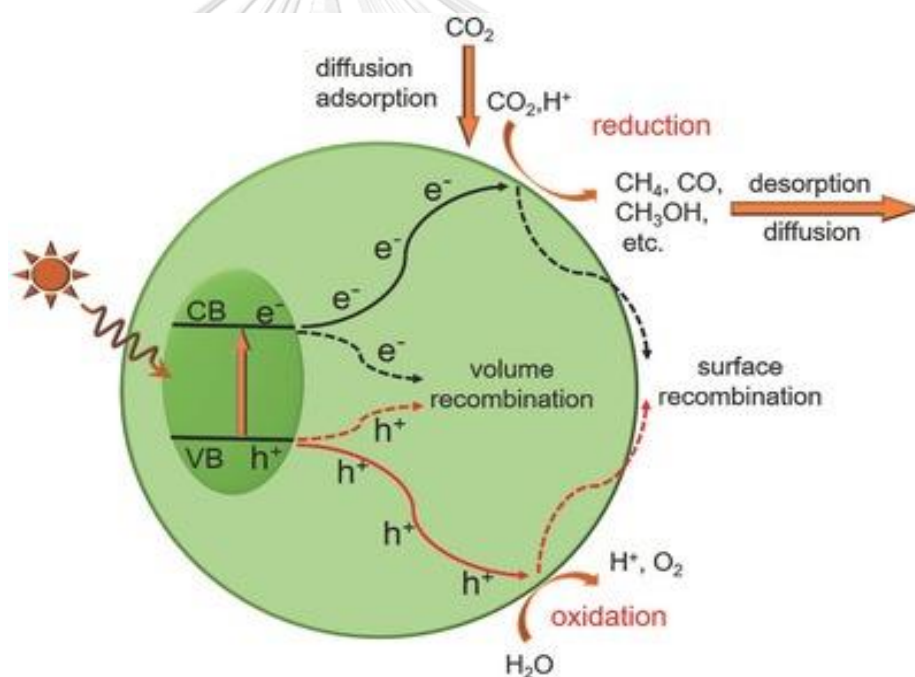
Figure 7. Schematic showing the five fundamental steps in photocatalytic CO_2 reduction [5, 34].

To improve the selectivity of CO_2 RR, PEC for CO_2 RR applied solar energy as renewable energy consumption and external electric field. The PEC process for CO_2 utilization can follow five steps that were shown in figure 7, including light absorption, charge separation, CO_2 adsorption, surface redox reaction, and product

desorption. First, the photons are absorbed on a photoelectrode surface that is deposited by a photocatalyst made of suitable semiconductors before electron and hole pairs are produced. Then, photogenerated electrons and holes separate and electrons transfer from the photoelectrode surface to the redox electrode surface where molecules of CO_2 were absorbed while holes are accumulated at the photoelectrode compartment. CO_2 reduction and oxygen evolution reactions (OER) occur at the redox-electrode and photoelectrode, respectively. Finally, the products from CO_2 and OER are desorbed after the process is complete [5, 34]. Some possible half-reaction of OER at anode compartments and CO_2 reduction at cathode to formic acid is shown in reactions (9) to (11), respectively. In addition, hydrogen evolution reaction (HER) is the side reaction of CO_2 reduction is also shown in reaction (12) [35].

Anode: $$semiconductor \rightarrow h^+ + e^- \tag{9}$$

OER: $$2OH^- \rightarrow 0.5O_2 + H_2O + 2e^- \tag{10}$$

Cathode: CO_2 RR: $$CO_2 + H_2O + 2e^- \rightarrow HCOO^- + OH^- \tag{11}$$

HER: $$2H_2O + 2e^- \rightarrow H_2 + 2OH^- \tag{12}$$
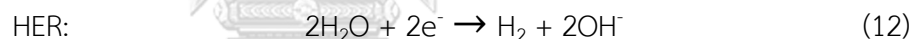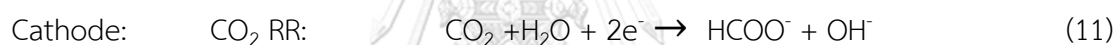
Because of cooperation and the advantages of solar energy and electrolysis reaction, the PEC process can operate under mild conditions, consume less input energy, and work under environmentally friendly. To add extra supplements, the PEC cell for CO_2 RR could be coordinated with other applications. Z. Zheng et al. [36] presented the applied progress of PEC cells in different functions comprising wastewater treatment coupled with H_2 production, wastewater treatment coupled with H_2O_2 production, wastewater treatment coupled with desalination, electricity supplied from wastewater treatment, and wastewater treatment coupled with CO_2 reduction. The PEC cells improved efficiency by replacing suspended photocatalysts with synthesized photocatalysts on photoelectrode and applying low voltage on counter-electrode. For the multifunction of PEC CO_2 reduction, the excess electrons were transferred to the cathode compartment to reduce CO_2 while pollutants were degraded by accumulated holes in the anode compartment.

Although PEC CO_2 reduction coupled with wastewater treatment can produce high-value products and treat wastewater, the effect of PEC cells configuration and components including photoelectrodes, counter-electrodes, supporting aqueous electrolyte, ion exchange membrane, and applied voltages requires more research to scale up the technology into industry process.

2.3.4 Biochemical CO_2 conversion

Biological CO_2 RR involves applying enzymes as catalyst that can improve selectivity and efficiency. The high purity feedstocks of biochemical of CO_2 RR are not desired due to the impurity of the process not toxicity to an enzyme [5]. In addition, the integration of enzyme catalysis with solar energy can solve the high demand for an energy input of CO_2 RR.

J. Milano et al. [37] offered an alternative to reduce fossil fuel consumption, the photosynthetic microorganisms are biological processes related to CO_2 RR by utilizing solar energy for chemical energy. The microorganisms such as microalgae required minimum nutrients, and the biomass contents were dried and converted to fuel by other strategies. However, cultivation areas and the costs of the harvesting stages are still a limitation for CO_2 utilization.

From various CO_2 conversion routes, each route has different advantages and disadvantages that are appropriate for specific value-added products can be concluded in figure 8 and table 6.
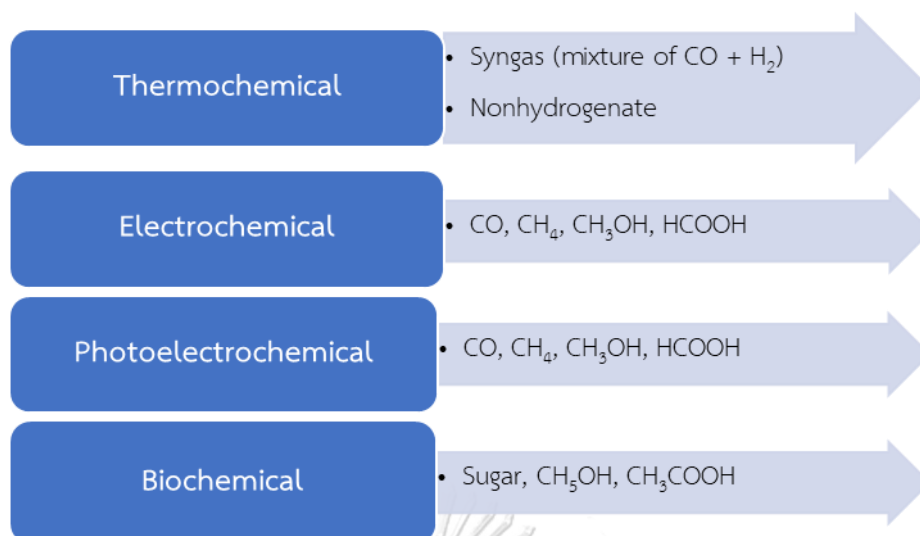
Figure 8. Main products from various CO_2 conversion routes [38]

Table 6. Advantages and disadvantages of various CO_2 conversion routes [39].

CO_2 conversion routes	Advantages	Disadvantages
Thermochemical	- High value-added products such as syngas can be reformed into liquid fuel.	- Require a large amount of energy. - Deactivation of catalysts.
Electrochemical	- Can be operated at room temperature. - Easily to scale up. - Products can use as a source of electricity generation.	- High-cost production - Short catalyst lifetime - The external electric field is required.
Photoelectrochemical	- Renewable energy consumption - Can be operated under mild conditions. - Low-cost production - Environmentally friendly - Low external electrical consumption	- Low yield production - Selectivity depended on various factors. - Difficult to separate catalyst
Biochemical	- Less energy input is required. - High selectivity	- Low efficiency - Future research is needed.

2.4 Conceptual design of photoelectrochemical CO_2 RR

To improve the performance of the PEC CO_2 process, the effective factors like light intensity, operating mode (batch reaction system and continuous flow reaction system), operating conditions (temperature, pressure, flow rate), bandgap (type of semiconductors as photocatalyst), pH (type of electrolyte), product separator (type of ion-exchange membrane), and cell configurations were reviewed in many pieces of research for laboratory scale. The arrangement and PEC cell geometric configuration of the main components include photoelectrode, counter-electrode, electrolyte, and ionic conducting membrane which are still challenging for investigation in the laboratory and pilot plant, therefore, the numerical study for CO_2 reduction should be applied to model and simulate the process [40].

2.4.1 Design of PEC cell

1. H-type cell

The H-type cell operates via a batch reaction system that is widely used on a laboratory scale. This cell configuration is less expensive because of its easy operation and abundant materials of electrodes. Normally, the H-type cell is assembled with 2 chambers of cathode and anode compartments which are separated using an ionic conducting exchange membrane to provide high purity of products from the reaction. Besides, three electrodes are also assembled consisting of the working electrode (WE), reference electrode (RE), and counter-electrode (CE), the WE and RE exist in the cathode compartment while CE exists in the anode compartment which H-type as shown in figure 9 [20, 41].
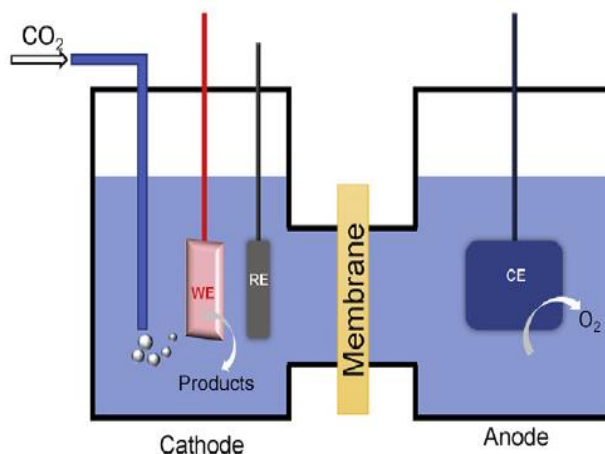
Figure 9. H-type cell [41].

Before CO_2 is fed as liquid feedstock that requires dissolution in catholyte, this technology still acquired low conversion efficiency. To obtain higher performance, the longer electrolysis time and smaller electrode compartment should be concerned.

To increase conversion efficiency, K. P. Kuhl et al. [42] proposed the modified H-type cell maximizing the ratio of the electrode surface area to electrolyte volume (S/V). This strategy adjusted the form of electrodes in the conventional H-type cell to the plate to support with bulk catalysts that working and counter electrodes were placed in parallel directions at a small distance which as shown in figure 10. The results showed higher conversion efficiency because the uniform distribution of voltages has occurred.
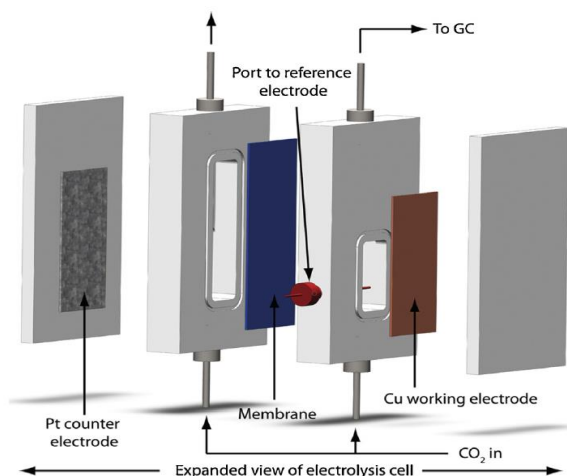
Figure 10. Modified H-type cell [20].

Although the ratio of the electrode surface area to electrolyte volume (S/V) was solved, the low solubility of CO_2 in the liquid phase still hinders the high conversion of CO_2 RR [42].

2. Microfluidic flow cell (MFC)

A microfluidic flow cell (MFC) provides continuous operation to increase the conversion of CO_2 RR which as shown in figure 11. MFC solves mass transfer problems via feed as continuous flow to obtain a high reaction rate into the feedstock chamber that attaches to the backside of the cathode, besides the electrolyte chamber is located between the cathode and anode compartments [41].
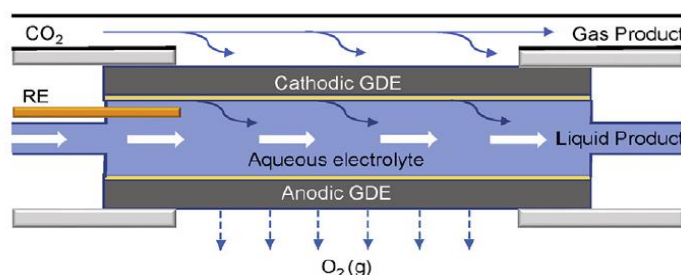
Figure 11. Microfluid flow cell (MFC) [41].

For this flow cell, CO_2 in the gas phase is supplied into the gas chamber before being reduced at the interface of the catalyst/electrolyte layer. However, the low conversion occurred due to the transfer of CO_2 being limited. Therefore, a gas

diffusion electrode (GDE) is employed as electrodes to override the problem. GDE consists of three sections including a catalytic layer (CL), a gas diffusion layer (GDL), and a gas flow field. Applying GDE can improve the conversion of reaction because the hydrophobic property of GDL can hinder the clogging of electrolytes in the pores and support the transport of CO_2 to the CL. Although the results from more chance for direct contact can increase selectivity due to the pH from electrolyte promoting the suitable environment for CO_2 RR, the MFC is not easy to scale up due to the effect of different pressure on the structure [41].

The ionic conducting membrane is used to provide a more suitable environment for CO_2 RR that increases the selectivity of CO_2 RR. The ion exchange membrane is located between catholyte and anode chambers to separate products and prevent the accumulation of ions which as shown in figure 12 [43].
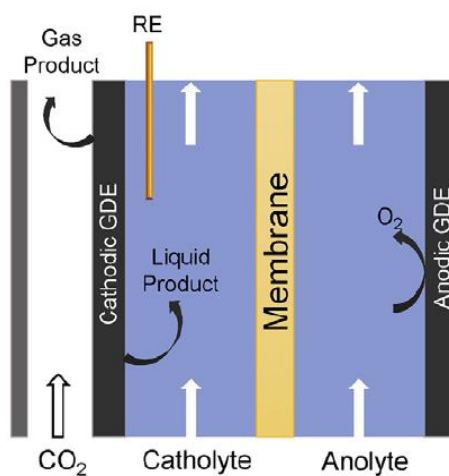
Figure 12. Membrane-based flow cell or polymer electrode membrane flow cell [40].

The ionic conducting membrane or polymer electrode membrane can sort into anion exchange membrane (AEM), cation exchange membrane (CEM), and bipolar membrane (BPM). The AEM serves to allow anions transfer from cathode to anode compartment, while the CEM conducts cations from anode to cathode, thus BPM allows cations and anion transfer to cathode and anode, respectively. Although

the existence of PEM can offer high selectivity, the PEM also causes a large ohmic loss and impurities production that decreases the performance of the PEC cell [43].

3. Membrane electrode assembly (MEA) flow cell

From the large ohmic loss between two electrodes and impurities production in catholyte in the polymer electrode membrane flow cell, the polymer electrode membrane flow cell rearranged the configuration of two electrodes to solve these problems. The configuration of membrane electrode assembly (MEA) flow cell sets to reduce the distance between the location of two electrodes which as shown in figure 13 [44].
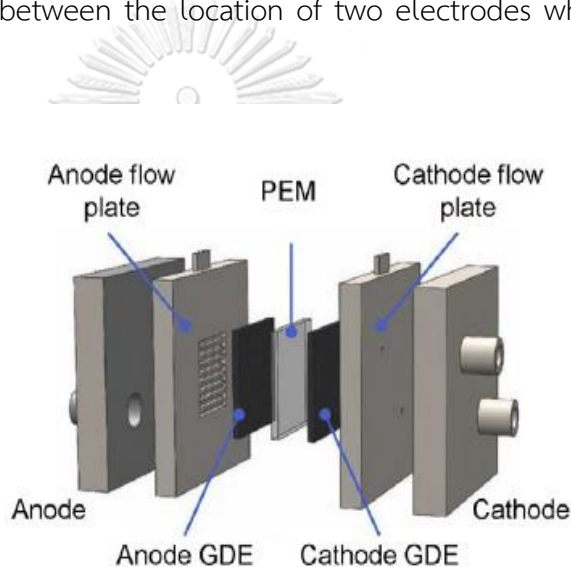
Figure 13. Membrane electrode assembly flow cell (MEAFC) [41].

Apart from the rearrangement of two electrodes, the MEA can serve both phases of reactants. The routes of reactant feeding are classified into (i) CO_2 dissolved in liquid catholyte/ liquid anolyte, (ii) CO_2 in the gas phase/liquid electrolytes (catholyte and anolyte), and (iii) humidified gases fed to both electrodes. For humidified gases fed to both electrodes, external saturation of CO_2 and two liquid electrolytes are applied which CO_2 is saturated by using a pump to continuously circulate through liquid catholyte. The schematic diagram of CO_2 RR to ethylene applied humidified gases fed to both electrodes which is shown in figure 14 [45].
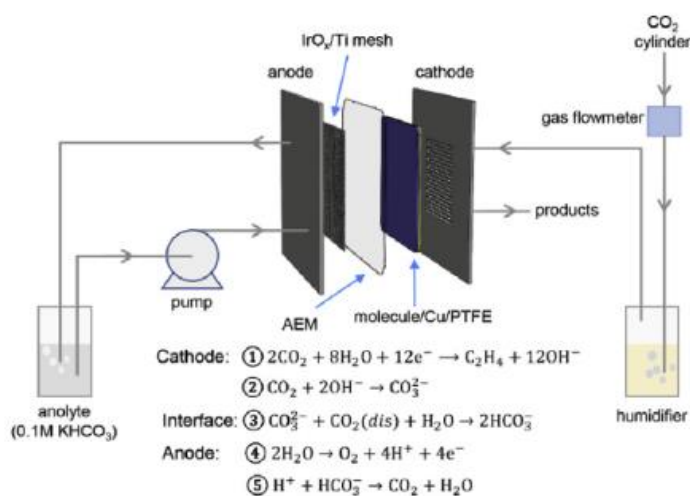
Figure 14. Schematic diagram of the reduction CO_2 to ethylene using MEAFC [45].

A large amount of ohmic loss and low solubility of CO_2 can be solved via applying MEA flow cell leads to improve selectivity and performance of the PEC CO_2 RR system, this configuration is appropriate for scaling up. But, the reference electrode (RE) is not used, so an external electric field is required for MEA flow cells [45].

4. Solid electrolysis cell (SOEC)

Besides remodeling the PEC cell configuration, the effect of operating conditions should be concerned. Some value-added products are appropriate to operate under high-temperature conditions. The solid electrolysis cell (SOEC) used a solid electrolyte to transfer carrier ions coupled with porous anode and cathode which as shown in figure 15 [20].
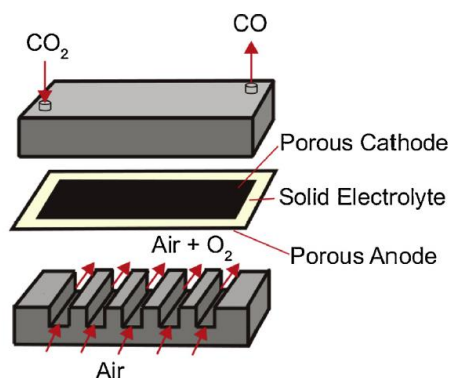
Figure 15. Solid electrolysis cell (SOEC) [20].

Applying SOEC for high-temperature reactions requires heat that can be consumed as waste heat, this process can decrease external electrical field and drive kinetics of reactions to provide high conversion of CO_2 RR. But the SOEC limits the multiple products from CO_2 RR due to high-temperature results in immediate desorption of some species occurring [20, 46].

From the study of PEC cell design, the advantages and disadvantages were summarized in table 7.

Table 7. The advantages and disadvantages of each reactor design [20, 41, 47].

Type of reactor design		Advantages	Disadvantages
H-type cell (Batch)	H-type cell	- Low cost - Widely uses on a laboratory scale. - Wide range of electrode	- Mass transport limitation - Less liquid products cannot be detected.
	Modified H-type cell	- High S/V ratio to define liquid products.	- Electrodes form limitation - Bubble formation hinders mass transport.
Flow cell	MFC	- High reaction rate - Improve mass transport - Provide suitable environments	- Different pressure across cell - Ohmic loss
	MEA flow cell	- Low ohmic loss - Solve low solubility of CO_2 in an aqueous solution. - Avoid bubble formation.	- Require an external electric field - High overpotential leads to corrosion problems.
	SOEC	- Can operate at high temperature. - High reaction rate	- Multiple products limitation

2.4.2 Performance indicators of PEC CO_2 RR

To define the optimum operating conditions, the PEC CO_2 RR was examined in different operating conditions and cell configurations due to various effective factors of the system such as light intensity, bandgap, flow rate, geometric PEC cell, and other operating conditions. The efficiency performance of PEC CO_2 RR can be expressed in various forms including CO_2 conversion, faradaic efficiency, current density, and energy efficiency as based indicators for comparing the performance of PEC CO_2 RR in various conditions.

1. CO_2 conversion

CO_2 conversion (X_{CO_2}) is defined as a ratio of the amount of CO_2 reactant that can be reacted to chemical products to the amount of CO_2 reactant. For continuous processes, X_{CO_2} can be calculated by Eq. 2.

$$X_{CO_2} = \frac{F_{CO_2,0} - F_{CO_2}}{F_{CO_2,0}}$$
Eq. (2)

where $F_{CO_2,0}$ is the initial molar flow rate of CO_2 (mol/s)

F_{CO_2} is the final molar flow rate of CO_2 (mol/s)

2. Selectivity of desired product

Selectivity (*S*) is the number of moles of interested product formed per the number of moles of overall products formed. Selectivity can be calculated by Eq. 3.

$$S = \frac{\text{Moles formed of interested product}}{\text{Moles formed of overall products}}$$
Eq. (3)

3. Faradaic efficiency (FE)

Faradaic efficiency (FE) indicates the amount of fuel consumption with the amount of obtained current. The FE for PEC CO_2 reduction can be defined as a ratio of the current that promotes CO_2 conversion into chemical fuels to the received current. In addition, FE also shows the amount of electric consumption to produce desired products over the amount of charge transfer in the system, which can be calculated by Eq. (4) [6].

$$FE(\%) = \frac{e_{output}}{e_{input}} \times 100\%$$

$$= \frac{n \text{ (mol)} \times y}{\frac{Q \text{ (Coulomb)}}{F(\frac{\text{Coulomb}}{\text{mol}})}} \times 100\% \qquad \text{Eq. (4)}$$

where n is the number of moles of the desired product

y is the number of electrons needed to convert CO_2 into the desired product

Q is the calculated electric charge (Coulomb)

F is the Faraday constant (96485 Coulombs/mols of desired product)

The high FE can be mentioned to the high selectivity of CO_2 RR to desired products, resulting in low cost due to the unnecessary product separation unit.

4. Current density

The current density or density of an electric current represents the amount of electric charge flow (amperes) per the projected area of the photoelectrode (unit: cm^2). The amount of electric charge transfer in the reaction is directly proportional to the number of products that occurred, or reactants consumed. When current density increases, it can refer to the consumption rate of reactants that is increasing. In particular, when the partial current density increases, it can refer to the increase in production rate of products concerned [47].

5. Energy efficiency (EE)

The energy efficiency (EE) of the interested product is the amount of the electric energy that is supplied to the cell for interested product formation, which can be calculated by Eq. (5) [6].

$$EE(\%) = \frac{\text{Productivity (mol s}^{-1})\cdot\Delta H^{\circ}_{comb}(\text{J mol}^{-1})}{I_{cell}(A)\cdot E_{cell}(V)} \times 100$$

$$= FE(\%) \times \frac{E_{therm}(V)}{E_{cell}(V)} \qquad \text{Eq. (5)}$$

where ΔH°_{comb} is the combustion energy under standard conditions

E_{therm} is the thermoneutral voltage

2.5 Components of PEC cell

As well as the effect of the arrangement of PEC cell configuration, the component of the PEC cell is considered because the PEC reaction occurs on the interface of electrode and electrolyte. The suitable environment on the PEC cell should provide for high efficiency of PEC CO_2RR. After this, the components of the PEC cell including photoelectrode, electrochemical electrode, and electrolyte are reviewed to study the effects of each component on the efficiency of electrochemical CO_2RR.

2.5.1 Photoelectrode

The electrode can define as an electrical conductor which employs electric currents carrying to the non-metallic section that is an electrolyte, a semiconductor, and air. Besides, the photoelectrode which is applied for light absorption and free electron and hole transportation, types of photoelectrode are classified by configuration and mechanism of charge carriers, as described below:
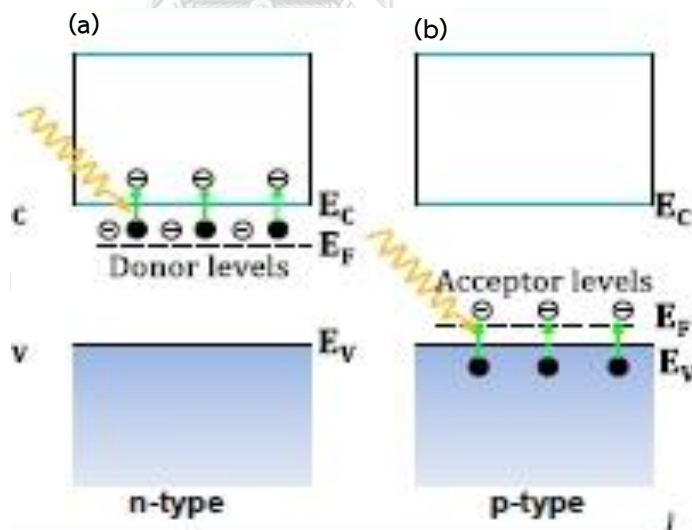
Figure 16. The schematic of charge carrier mechanism of photoelectrochemical cell (PEC) based on (a) n-type semiconductor and (b) p-type semiconductor [48].

Note: E_v, E_c, and E_F denote energy levels of valence band, conduction band, and Fermi energy level, respectively. Fermi level is the highest energy level of an energy at absolute zero temperature or the surface level where electrons do not have enough energy to rise above.
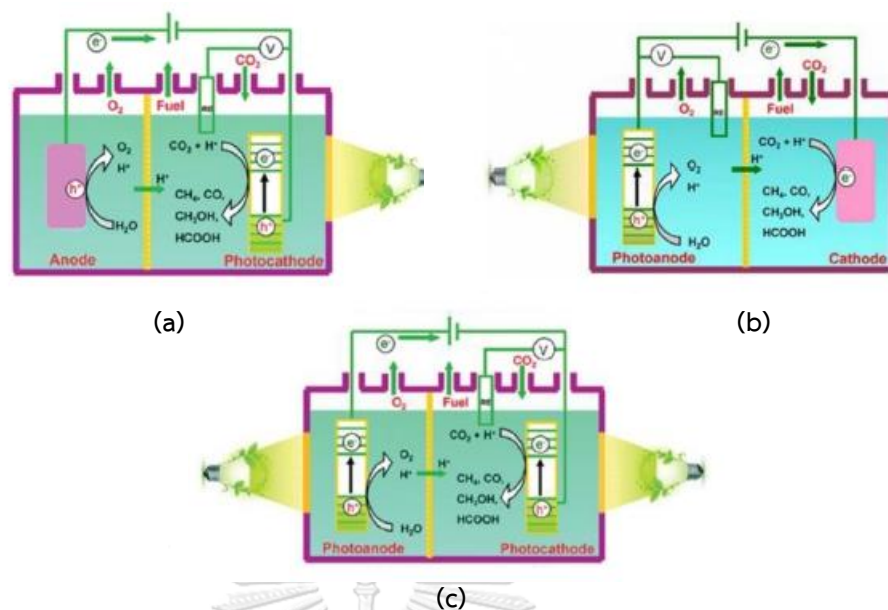
Figure 17. The schematics of (a) P-type semiconductor as photocathode (b) N-type semiconductor as photoanode and (c) Z-scheme with semiconductors as photocathode-photoanode [24].

1. Photocathode-Dark anode

From figures 16(a) and 17(a), the p-type semiconductor and metal are applied as photocathode and dark anode, respectively. The p-type semiconductor which is one of the extrinsic semiconductors has negative potential higher than the half-cell reduction reaction. The major charge carrier of p-type semiconductors is holes (h^+) or acceptor impurity doped, electrons transfer from p-type semiconductors to reducing surface and holes move back to the interface of photocathode/electrolyte. The Femi level of the p-type semiconductors locates close to the top of valance band (VB) which is less than the intrinsic semiconductor. The efficiency of p-type semiconductors is relatively low; therefore, a bias potential is required for the half-cell oxidation reaction. The metal-doped on intrinsic semiconductors of p-type such as boron (B), aluminium (Al), gallium (Ga), lead (Pb), Ag (silver), Au (aurum), Pd (palladium), Cu (Copper), and Ni (nickel) [24]. However, p-type semiconductors are costly, less stable, and toxic, thus, are still challenging to improve the efficiency of p-type semiconductors as photocathodes.

The p-type semiconductors as photoelectrode have been studied in many experiments to obtain more positive potential for oxidation reaction. For example, S. Kaneco et al. [49] presented the efficiency of PEC CO_2 RR in which CO_2 was saturated in a methanol-based electrolyte using a flow cell configuration. The flow cell with a methanol-based electrolyte of this experiment comprised a p-InP photocathode immersed in LiOH as catholyte, Ag/AgCl sat KCl as reference electrode, Nafion-117 as ion exchange membrane, and Pt-dark anode immersed in KOH as anolyte, respectively. In addition, 5000 W of Xe lamp (λ>300nm) was illuminated on the p-InP photocathode. The p-InP photocathode immersed in methanol-based electrolyte applied more positive potential versus the reference electrode to obtain desired products when compared with other metallic electrode systems. The results showed 41.5% and 15.0% faradaic efficiencies of CO and $HCOO^-$ were presented at -2.5 V vs. Ag/AgCl sat KCl, respectively.

Moreover, X. Huang et al. [50] demonstrated PEC CO_2 RR through $Ru(bpy)_2dppz$-Co_3O_4/CA as a p-type semiconductor photocathode with graphite plate as a dark anode. The hybrid interface of the photocathode of this experiment included Co_3O_4, $Ru(bpy)_2dppz$-, and CO_2 were supplied for light energy harvesting, mediation of the electron transportation, and substrate activation. For energy supply, the Xe lamp (λ>420nm) was illuminated on Co_3O_4, $Ru(bpy)_2dppz$ photocathode. The results showed the FE of $HCOO^-$ at -0.60 V vs. NHE reached 86% which consumed more positive than the thermodynamic potential of CO_2RR to $HCOO^-$.

In conclusion, the p-InP photocathode immersed in a methanol-based electrolyte can reduce the electrical energy consumption of PEC CO_2 RR which is a good offer for scaling up to industrial production.

2. Photoanode-Dark cathode

From figures 16(b) and 17(b), the n-type semiconductor and metal are applied as photoanode and dark cathode, respectively. The n-type semiconductor which is one of the extrinsic semiconductors requires low external bias to support the half-cell reduction reaction. The major charge carrier of n-type semiconductors is electrons (e⁻) or donor impurity doped, holes transfer from n-type semiconductors to the oxidizing surface and electrons move to bulk which back to the interface of cathode/electrolyte. The Femi level of the n-type semiconductors locates close to the bottom of conduction band (CB) which is more than the intrinsic semiconductor. The efficiency of n-type semiconductors is relative to the concentration of electrons more than the band gap; therefore, n-type semiconductors respond to current conduction. The metal-doped on intrinsic semiconductors of n-type such as phosphorus (P), arsenic (As), antimony (Sb), and bismuth (Bi). The n-type semiconductors are inexpensive, earth-abundant, and highly stable [24]. Although, the good activity of electrocatalyst on the dark cathode is desired to obtain high product selectivity from this configuration.

The activity of photocatalysts and electrocatalysts was focused to obtain high efficiency of PEC cells and high selectivity for CO_2RR. G. Magesh et al. [51] proposed PEC systems for CO_2 RR via flow cell configuration which using WO_3 as a photoanode, electrocatalysts of CO_2 RR as a cathode, and KCl as an electrolyte operated under the illumination of a 500 W Hg lamp (λ>420nm). The WO_3 was utilized due to high activity and stability for oxygen evolution reaction (OER). The electrocatalysts of CO_2 RR were Cu and Sn/SnO_x which were utilized due to high selectivity for CO_2 RR to CH_4 and CO and HCOO, respectively. The results via the PEC system of WO_3 photoanode with Cu cathode indicated a 67% FE_{CH_4} at -0.75 V vs. RHE while WO_3 photoanode with Sn/SnO_x cathode indicated a 15.9% FE_{CO} and 27.5% FE_{HCOOH} at -0.80 V vs. RHE. In addition, I. E. Irem et al. [52] improved the efficiency of PEC CO_2RR using TiO_2 photoanode and Sn-GDE cathode operated under the illumination of a 300

W Xe lamp. To increase the concentration and mass transfer of substrate, the gaseous CO_2 was direct fed Sn-GDE cathode to the filter-press flow cell. The results demonstrated 64% FE_{HCOOH} and 70% EE_{HCOOH} when a 1.2 V bias potential is applied.

To summarize, the overall efficiency of the photoanode-dark cathode system depends on efficiency from both half-cell oxidation and reduction. The low bias potential under visible light irradiation is enough to drive the overall efficiency of the photoanode-dark cathode system.

3. Photocathode-Photoanode

From figure 17(c), the integration of two photoelectrodes also known as Z-scheme including the p-type semiconductor and n-type semiconductor for CO_2 reduction and H_2O oxidation. The p-type semiconductor or photoanode should have negative potential higher than n-type semiconductor or photocathode to provide electrons transportation from photoanode to photocathode. The photocathode and photoanode can excite holes and electrons, respectively. The Z-scheme configuration is self-biased with potential voltage supporting from the difference value between of Femi levels of photocathode and photoanode [53]. Therefore, the suitable semiconductors are required for Z-scheme to approve the half-cell reactions.

Because without bias potential configuration, the evolution of PEC through Z-scheme configuration was investigated with many photocatalysts to accomplish high efficiency. T. Morikawa et al. [54] offered a novel hybrid photocatalyst for PEC applied to photoanode-photocathode or Z-scheme configuration. Novel hybrid photocatalysts consisting of TiO_2 which was employed as a photoanode and InP/Ru complex was employed as a photocathode for water oxidation and CO_2 RR, respectively. Under free electrical bias potential and simulated light illumination conditions (1 sun, Air mass 1.5), the FE of $HCOO^-$ could reach 75% at -0.6 V vs. NHE. Besides, B. Weng et al. [55] represented high catalytic activity for PEC through Z-scheme configuration. To obtain TiO_2 NWs@CoP/CN as a photoanode and Si

NWs@CoP/CN as a photocathode, the CoP wrapped with porous N-doped carbon network (CoP/CN) nanocatalyst was consumed to coated TiO_2 nanowires (TiO_2 NWs) and p-type Si nanowires (Si NWs). The bifunctional of CoP/CN is high activity and stability for water oxidation and CO_2 RR, also the FE of CO could reach 90% at -0.15 V vs. RHE.

　　　　To conclude from the previous literature reviews, the Z-scheme without external electric bias plays an important role in saving energy consumption for the PEC system. However, the proper semiconductor photoelectrodes should be concerned to prevent side products from high potential providing.

　　　　Lastly, to illustrate the difference between photoelectrode configurations, advantages and disadvantages, a summary of the literature reviews is shown in tables 8 to 10.

Table 8. The difference between p-type semiconductor and n-type semiconductor [24].

	Photocathode-Dark anode (P-type semiconductor)	Photoanode-Dark cathode (N-type semiconductor)
Also known as	Acceptor impurity	Donor impurity
Major charge carriers	h^+	e^-
Minor charge carriers	e^-	h^+
Doped group	Group III elements. For example: B, Ga, Al, and Ni etc.	Group V elements. For example: P, As, Sb, and Bi etc.

Table 9. Advantages and disadvantages of different photoelectrode configurations [24, 53].

Photoelectrode configurations	Advantages	Disadvantages
Photocathode-Dark anode (P-type semiconductor)	- Use lower the doping elements - High product selectivity	- Costly elements - Less stable in aqueous solutions - High toxicity - Require a large bias potential
Photoanode-Dark cathode (N-type semiconductor)	- Inexpensive elements - Made of earth-abundant elements - Highly stable in aqueous solutions - Low toxicity - Offer high mobility of electrons	- Require a bias potential - Low product selectivity
Photoanode-Photocathode (Z-scheme)	- Operate without external electrical energy	- Complex design reactor - May occur backward reaction due to reversibility of ionic mediator

Table 10. Summary of the literature reviews of different photoelectrode configurations.

Anode	Cathode	Main products	Operating conditions	Efficiency	Ref.
Photocathode-Dark anode (P-type semiconductor)					
Pt	p-InP	CO; HCOO$^-$	Reactant: CO$_2$ saturated in methanol, Anolyte/Catholyte: 300 mol·m^{-3} KOH/LiOH in methanol, Light source: 5000 W Xe lamp (λ>300nm), Electrode potential: -2.5 V vs. Ag/AgCl sat KCl	FE$_{CO}$: 41.5% FE$_{HCOOH}$: 15.0%	S. Kaneco et al. (2006), [49]
Graphite plate	Ru(bpy)$_2$dppz-Co$_3$O$_4$/CA	HCOO$^-$	Light source: Xe lamp (λ>420nm), Electrode potential: -0.60 V vs. NHE	FE$_{HCOO^-}$: 86%	X. Huang et al. (2016), [50]
Photoanode-Dark cathode (N-type semiconductor)					
WO$_3$	Sn/SnO$_x$	CO; HCOOH	Light source: 500 W Hg lamp (λ>420nm), Electrode potential: -0.80 V vs. RHE	FE$_{CO}$: 15.9% FE$_{HCOOH}$: 27.5%	G. Magesh et al. (2014), [51]
TiO$_2$	Sn-GDE	HCOO$^-$	Light source: 300 W Xe lamp, Applied bias potential: 1.20 V	FE$_{HCOO^-}$: 40-65%	I. E. Irtem et al. (2017), [52]
Photoanode-Photocathode (Z-scheme)					
TiO$_2$	InP/Ru complex	HCOO$^-$	Light source: 1 sun (AM 1.5), Applied bias potential: 0 V, Electrode potential: -0.6 V vs. NHE	FE$_{HCOO^-}$: 75%	T. Morikawa et al. (2012), [54]
TiO$_2$ NWs@CoP/CN	Si NWs@CoP/CN	CO; CH$_4$	Electrode potential: -0.15 V vs. RHE	FE$_{CO}$: 90%	E. Weng et al. (2016), [55]

For this study, the photoanode-dark cathode configuration was applied because it can reduce the external bias consumption and sustain stability in aqueous solutions. The photoanode are made of a thin film of metal oxide supported on a transparent conducting oxide (TCO).

The photocatalysts are light absorbing materials that induce chemical reactions. The properties of photocatalysts can affect PEC performance because photocatalyst can convert solar energy or light energy into electrical energy which can promote high potential on the cathode surface [56]. The good properties of photoactive semiconductor used as photoanode for chemical conversion application should have high negative potential than the potential of interested half-cell reaction to thermodynamically support oxidation and reduction reactions of hole and electron, respectively. Moreover, the activity, conductivity, and stability of the photocatalyst should be high enough to promote the half-cell reaction on photoelectrode [57].

Titanium dioxide (TiO_2) is the one of the n-type semiconductors and the most common photocatalyst due to its wide band gap (3.20, 3.02, and 2.96 eV for anatase, rutile, and brookite phases, respectively), high resistance to photo-corrosion, non-toxicity, earth abandon, and low production cost [58, 59].

The applied bias potential is required for CO_2 conversion to chemical products with high faradaic efficiencies. Many researchers investigated TiO_2 as a photoanode. K. Kobayashi et al [56] revealed the experimental of conventional flow cell PEC CO_2 RR to CO. The TiO_2 semiconductor was used as a photoanode to absorb photocurrent from simulated UV illumination using 300 W Hg lamp and Ni phthalocyanine (NiPc) catalyst deposited on GDE as a cathode. In addition, 0.1 M Na_2SO_4 and 1 M Na_2SO_4 were consumed as anolyte and catholyte, respectively. The results presented FE of CO reaching 98% under UV light illumination and -0.8 V of bias potential.

Utilization of TiO_2-photoanode can increase electrode potential on the cathode due to the supply of high electrical energy. The properties of TiO_2-photoanode are wide band gap energy and a high level of the conduction band, thus, the demand of photon absorption is high for electrons excitation to the conduction band of photoelectrode [57, 58]. However, the geometries of TiO_2-photoanode like length and thickness should be concerned to reduce resistance at photoelectrode and overall ohmic polarization loss of the PEC system.

2.5.2 Electrochemical electrode

The cathodic electrode is used as an electrochemical electrode in this study. The electrocatalyst for CO_2 RR should have high activity, electrical conductivity, selectivity, and stability in aqueous solutions operated under ambient operating conditions. Tables 2 and 3 indicated the products from multistep of CO_2 RR depending on electrode potential. To obtain desired products, the intermediate species from CO_2 RR such as $CO_2^{\cdot -}$ should be adsorbed and stabilized on the catalyst surface. Besides, the products from CO_2 RR such as CO and $HCOO^-$ should be smoothly desorbed from the active surface of the catalyst. Therefore, the electrocatalysts for CO_2 RR were considered to achieve high product selectivity. The categories of electrocatalysts for CO_2 RR can be divided using types of metal elements consisting of transition metal elements (Sc, Ti, Cr, Mn, Fe, Co, Ni, Cu, Zn, Mo, Cd, Ta, and Hg), noble metal elements (Pd, Ag, Ir, Pt, and Au), and p-block elements (Al, Ga, In, Sn, Sb, Tl, Pb, and Bi) [52, 60]. By the way, the categories of electrocatalysts for CO_2RR can be divided using occurring products which were clarified as shown below:
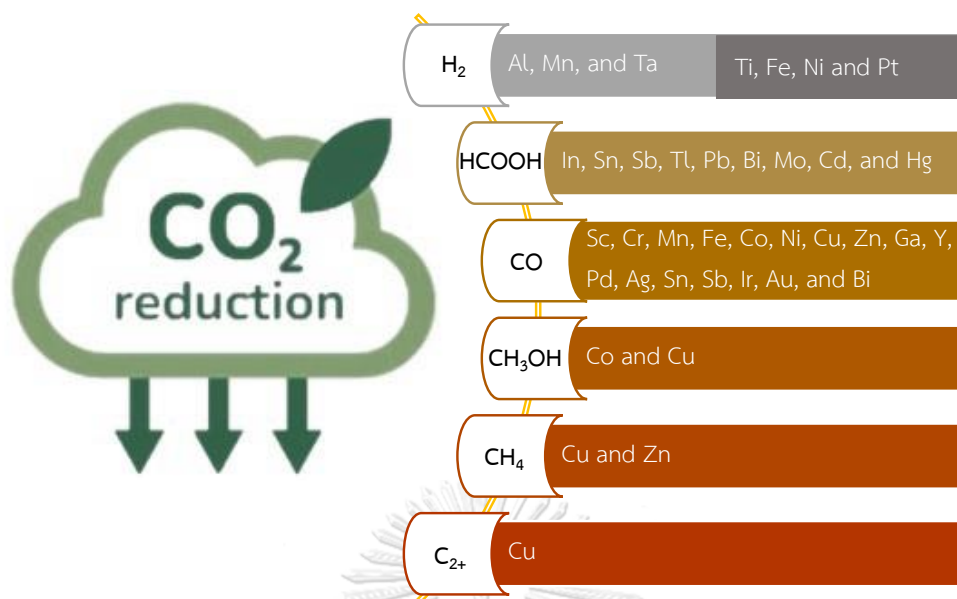
Figure 18. The categories of electrocatalysts for CO_2 RR [52, 60].

1. The electrocatalysts for CO_2 RR to H_2

Apart from multi-carbon products, H_2 is also a side product from CO_2RR which is shown in reaction (12). The electrocatalysts that involve hydrogen evolution reaction (HER) are separated into inert and semi-inert. The inert electrocatalysts for HER which are not affecting reaction rate though operating conditions are adjusted comprising of Al, Mn, and Ta. Likewise, the semi-inert electrocatalysts for HER which affect the reaction rate when operating conditions are adjusted comprising of Ti, Fe, Ni, and Pt [52, 60].

2. The electrocatalysts for CO_2 RR to HCOOH

The electrocatalysts for CO_2 RR to formate ion, $HCOO^-$ (or HCOOH when operating in the acidic electrolyte) consist of In, Sn, Sb, Tl, Pb, Bi, Mo, Cd, and Hg. These electrocatalysts have high electrode potential to adsorb and stabilize intermediate species ($CO_2^{\cdot-}$) before reducing to desired products [52, 60].

3. The electrocatalysts for CO$_2$ RR to CO

The electrocatalysts for CO$_2$RR to CO consist of Sc, Sr, Mn, Fe, Co, Ni, Cu, Zn, Ga, Y, Pd Ag, Sn, Sb, Ir, au, and Bi. To break the C-O bond, the electrode potential of these electrocatalysts is greater than HER but less than CO$_2$ RR to HCOOH. Besides, the catalyst should easily desorb CO from the active surface [52, 60].

4. The electrocatalysts for CO$_2$ RR to C$_x$H$_y$O$_z$

The multi-carbon products include CH$_4$, C$_{2+}$, alcohols and aldehydes consisting of Co, Cu, and Zn. The activity of these electrocatalysts provides optimum CO adsorption and hydrogenation of adsorbed CO to CHO intermediate to obtain C$_x$H$_y$O$_z$, especially Cu [52, 60].

The interested electrocatalysts for CO$_2$ RR to HCOO$^-$ are in the 2nd category in which the widely used catalysts include In, Sn, Pb, Bi, and Hg. These elements are compared to specify the suitable catalyst for CO$_2$ RR to HCOO$^-$ which are shown in table 11.

Table 11. The properties of the widely used electrocatalyst for CO$_2$ RR to HCOO$^-$ [61, 62].

Property \ Catalyst	Physical characteristics at ambient conditions	Density (kg·m^{-3})	GHS hazard statements	Market price ($/kg)
In	Lustrous silvery solid metal	7.31 ×10^3	Not	222-225
Sn	Silvery white solid metal	7.28 ×10^3	Not	12-25.39
Pb	Silvery white or grayish solid metal	11.35 ×10^3	Slight	1.86-2.27
Bi	Silvery white solid metal	9.78 ×10^3	Not	15-39
Hg	Silvery white liquid metal	13.53 ×10^3	Acute	32-100

Note: GHS also known as Globally Harmonized System of Classification and Labelling of Chemicals

From table 11, the toxicity of In, Sn, Pb, and Bi are less toxic or even nontoxic than Hg when considered chemical hazards through GHS. In addition, the market prices of Sn, Pb, and Bi are quite minimal when compared with In and Hg.

Sn-based electrocatalysts are widely used in CO_2 RR to $HCOO^-$ due to their high selectivity and inexpensive. For example, D. Kopljar et al. [63] produced $HCOO^-$ at high current densities through a microfluidic flow cell (MFC) electrolyzer using Sn and SnO_2 deposited on gas diffusion electrodes (GDEs) were used as cathodes. First, nanoparticles of Sn and SnO_2 were examined to define characteristics and activities when coating on GDEs. From ex situ characterization, the diameter of SnO_2 nanospheres is wider than the diameter of Sn nanospheres. The activities of Sn-GDE and SnO_2-GDE which controlled mass loading (0.35 mg•cm^{-2}) were compared through current densities. The onset electrode potentials vs. Ag/AgCl of CO_2 RR derived from using SnO_2-GDE is -1.29 V and Sn-GDE is -1.92 V. The current densities of CO_2 RR derived from using SnO_2-GDE and Sn-GDE as cathode at onset potential vs. Ag/AgCl were 385±19 mA•cm^{-2} and 216±6 mA•cm^{-2}. Moreover, the production rates of $HCOO^-$ derived from 1-hour electrolysis using SnO_2-GDE and Sn-GDE as cathodes at onset potential vs. Ag/AgCl are 14.9±0.8 mmol•$m^{-2}s^{-1}$ and 7.4±0.6 mmol•$m^{-2}s^{-1}$, respectively. This experiment shows the FE of $HCOO^-$ could reach 79.00±3.13% and 70.00±3.99% for SnO_2-GDE and Sn-GDE as cathodic electrodes. D. Thuy et al. [64] spent tin oxide (SnO_2) nanospheres as electrocatalysts on CO_2 RR to $HCOO^-$. To define the effect of calcination temperature, SnO_2 nanoparticles were investigated through flow cell configuration. The higher calcination temperature could increase the diameter of SnO_2 nanocrystals, SnO_2 nanospheres calcined at 500°C was selected as electrocatalyst because of their ability to prevent agglomeration and provide a large surface area. In addition, SnO_2 nanospheres were deposited on a gas diffusion electrode (GDE) which was used as a cathode operating in a membrane electrode assembly (MEA) electrolyzer. The FE and current density of $HCOO^-$ could reach

75±6% and 500 mA•cm^{-2} at 1.41 V of equilibrium cell potential over 24 hours of electrolysis.

The high surface and activity of SnO_2 nanospheres can support the reason for scaling up the industrial production of CO_2 RR to HCOO$^-$. Besides the performance of catalysts, the configuration of the MEA electrolyzer that has direct feeding gaseous CO_2 to the cathode and alkaline environments also improves the current density and selectivity of HCOO$^-$.

2.5.3 Gas diffusion electrodes (GDEs)

The major limitations of the electrolyzer assembled with a planar electrode are low solubility of gaseous CO_2 in liquid electrolytes resulting in decreasing CO_2 conversion. Applying gas diffusion electrodes (GDEs) can improve the current density CO_2 conversion by solving the solubility of gaseous CO_2 in liquid electrolyte limitation and facilitating the transportation of reactive species to active sites [65, 66]. The schematic of GDE is shown in figure 19.
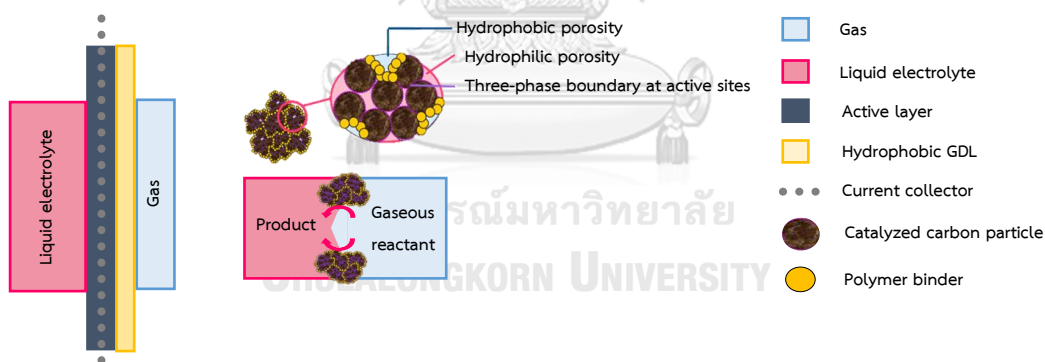
Figure 19. The schematic of GDE [67].

GDEs are porous electrodes made of assembling of porous catalyst layer with diffusion media. To support the three-phase interface (gas, liquid, and solid), GDEs comprise hydrophilic and hydrophobic sides. The three-phase interface is the contact boundary of the gaseous reactant, the liquid electrolyte, and the solid electrode. The hydrophilic side is dominant in the catalyst layer which provides the transport of ionic species and maximizes the active sites as a three-phase interface. And the

hydrophobic side is dominant in the diffusion layer which hinders flooding and blockage of the gas diffusion layer [68].

The usage examples of GDE on the electrochemical system, K. Wu et al. [69] demonstrated the computational modeling of the electrochemical CO_2 reduction to CO which this half-cell model at the cathode was simulated to evaluate the effective operating and design parameters of the microfluidic flow cell (MFC). The GDEs assembled with graphite current collector were used as electrodes for gaseous CO_2 feeding. The Pt blank-anode, aqueous KCl as electrolyte channel, and Ag-cathode were horizontally sandwiched in rectangular forms respectively. The electrochemical gaseous CO_2 RR model was assumed in isothermal and steady-state simulation through kinetics of charge species, mass, and momentum conservations. The current densities (CD) from the half-cell model were consistent with the experimental results. The results showed CD was improved, and faradaic efficiency (FE) was deduced when the negative applied voltage at the cathode was increased. Although increasing the feed concentration of CO_2 could increase the CD and FE, deducing of CO_2 conversion occurred. In addition, the longer cell was directly proportional to increasing CO_2 conversion, but the CD and FE were decreased. Y. Fu et al. [70] demonstrated a hierarchical SnO_2 microsphere coated on GDE (HMS- SnO_2/GDE) as an electrode for CO_2 RR to $HCOO^-$ in aqueous solutions. The operating of the flow cell electrolyzer at -1.7 V vs. SHE could allow 62% FE_{HCOO^-} over 12 hours of electrolysis. The synthesis of self-assembled SnO_2 microsphere catalysts via hydrothermal can improve the catalytic activity, coating catalysts on GDE also contributes to expanding surface area, decreasing the resistance between the gas-liquid interface and the catalyst surface, and hindering hydrogen evolution reaction (HER) by faster kinetics reaction.

Apart from that, the arrangement of GDE also impacts the performance of the electrochemical cell. H. Yang et al. [71] developed a new design configuration of the electrochemical cell to convert CO_2 to pure formic acid (HCOOH). The deionized (DI)

water substituted salt additions as an electrolyte and GDEs were used in the new design of an electrochemical cell that is divided into three compartments including an anode, center, and cathode compartments assembled in vertical following in a sequence from left to right. The cathode compartment was maintained in the alkaline environment to offer a reaction of CO_2 with DI water to formate ion ($HCOO^-$) by assembling an anion exchange membrane with GDE while a CEM was assembled in an anode compartment for O_2 and protons (H^+) production. Moreover, DI water was fed to the center compartment using strong acid cation exchange media for the reaction of $HCOO^-$ and H^+ derived from cathode and anode compartments respectively. The results showed the high current densities of 5-20 wt% HCOOH production equaled 140 mA•cm^{-2} when low applied voltage ($\sim$3.5 V) is consumed. In addition, the high performance of this configuration could be presented through 500 hours of the experiment set up that can conclude scaling up to the industrial process.

However, the GDEs are currently widely used in electrochemical systems, and the improvement of GDE is still concerned to reduce the limitation of mass transportation that affect selectivity and stability of electrochemical reactions.

2.5.4 Electrolyte

The CO_2 RR occurs between the interface of the electrode/electrolyte. The roles of electrolytes directly affect the efficiency of the electrochemical system. Electrolytes are substances that carry ionic species when dissolved in water [72]. The effective factors of electrolytes in an electrochemical system consist of concentration, pH, cations, and anions [73] which are given in detail as bellows.

1. Concentration

The optimum concentration of electrolyte can provide the high current efficiency of CO_2 RR. The dissociation of electrolyte performs the ions in solution, hydroxide ion (OH^-) also obtain from dissociation reaction. The charge transfer

resistance (R_{ct}) and the thickness of the electrical double layer (EDL) of the electrode can be reduced by absorbing on OH^- an active surface. The concentration of OH^- is increased when the supply has a higher electrolyte concentration [72, 73].

Q. Wang et al. [74] studied the effect of electrolyte concentration on CO_2 RR to $HCOO^-$ proceeding with direct gaseous CO_2 feeding to Sn-GDE cathode with $KHCO_3$ solution as a liquid electrolyte. The $KHCO_3$ solutions were varied concentrations of 0.1, 0.3, 0.5, 0.7, and 0.9 M under the applied bias potential of -1.8 V. The tendency of partial current densities of $HCOO^-$ increased when 0.1 M to 0.5 M $KHCO_3$ solutions were consumed. While the tendency of partial current densities of $HCOO^-$ decreased when 0.5 M to 0.9 M $KHCO_3$ solutions were consumed. Moreover, the variation of faradaic efficiencies of $HCOO^-$ when varied concentrations of $KHCO_3$ solutions were the same trend as partial current densities. The maximum partial current density and FE of $HCOO^-$ revealed 17.43±2.60 mA•cm^{-2} and 78.60±0.11% with consumption of 0.5 M $KHCO_3$ solution.

Similar to S. V. Kenis et al. [75] regarded variation of electrolyte concentration to the current efficiency of CO_2 RR. The conversion of CO_2 to CO in a flow cell assembled by Fe porphyrin mixed with carbon black deposited on carbon paper support as a cathode. The current density of CO was increased when the concentration of KOH electrolyte increased. The excess 2 M KOH electrolyte did not possess the higher current densities of CO.

Although the higher concentration of electrolyte can induce more CO_2 RR, the mass transfer limitation interrupts the higher current efficiency since the excess electrolyte concentration. Therefore, the optimum electrolyte concentration is required to save cost when scaling-up industries are performed.

2. Potential hydrogen (pH)

The influence of the pH of the electrolyte on electrochemical CO_2 RR is high because the OH^- on the electrode interface can be neutralized using bicarbonate buffers. The OH^- is a product from CO_2 RR and HER, the local environment on the electrode surface of CO_2 RR can be changed by the concentration of OH^- [72, 73]. The influence of pH can be described in equilibrium reactions of the CO_2 and bicarbonate which is shown in reactions (13) to (17).

$$CO_2 \text{ (g)} \leftrightarrow CO_2 \text{ (aq)}, \qquad K_s = 30 \text{ mol}^1 \cdot m^{-3} \cdot bar^{-1} \qquad (13)$$

$$CO_2 \text{ (aq)} + H_2O \leftrightarrow H_2CO_3, \qquad K_{eq} = 1.7 \times 10^{-3} \qquad (14a)$$

$$H_2CO_3 \leftrightarrow H^+ + HCO_3^-, \qquad pK_a = 3.6 \qquad (14b)$$

$$CO_2 \text{ (aq)} + H_2O \leftrightarrow H^+ + HCO_3^-, \qquad pK_a = 6.4 \qquad (14c)$$

$$HCO_3^- \leftrightarrow H^+ + CO_3^{2-}, \qquad pK_a = 10.3 \qquad (15)$$

When pH>7,

$$CO_2 + OH^- \leftrightarrow HCO_3^- \qquad (16)$$
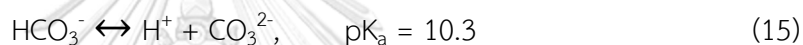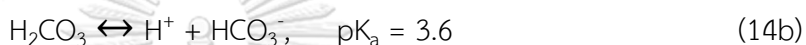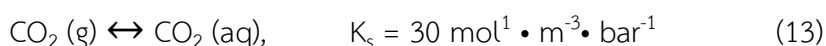
The neutralization of OH^- on the electrode surface.

$$HCO_3^- + OH^- \leftrightarrow H_2O + CO_3^2 \qquad (17)$$
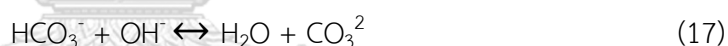
From reactions (14a) and (14c), the CO_2 hydration can form bicarbonate buffer (HCO_3^-), but the rates of reactions are very low which results in a very low concentration of H_2CO_3. However, the formation rate of HCO_3^- is high along reaction (16) when the pH of the electrolyte is more than 10. Besides, the HCO_3^- and CO_3^{2-} are assumed in the balance due to the deprotonation rate is being high along reactions (14b), (15), and (17). Therefore, when the pH of the electrolyte is higher than 10, the amount of HCO_3^- consumed as a proton donor is enough for CO_2 RR.

Because $KHCO_3$ solution is a buffer electrolyte which uses to sustain the local environment and neutral OH^- from CO_2 RR as shown in the equilibrium reaction. The CO_2 RR to $HCOO^-$ is hindered when a low concentration of $KHCO_3$ solution or weak buffer solution is employed since pH of the local environment is high. The high concentration of $KHCO_3$ solution or strong buffer solution can sustain pH of the local environment and improve ionic conductivity [72, 73]. However, the optimum

concentration of $KHCO_3$ solution is required for CO_2 RR to $HCOO^-$ because the excess concentration of $KHCO_3$ solution provides a hydrogen evolution reaction (HER).

The experiment was exposed by Y. Fu et al. [70] with feeding saturated CO_2 in aqueous electrolytes at -1.5 V vs. SHE. To convert CO_2 to $HCOO^-$ in aqueous solutions, the flow cell including Pt foil, SnO_2/GDE, and Nafion-117 were used as anode, cathode, and membrane, respectively. The faradaic efficiency of $HCOO^-$ when consuming an H_2O electrolyte with CO_2 bubbling showed only 1.0%. The faradaic efficiency and concentration showed 56.02% and 260 mg•L^{-1} when 0.5 M $KHCO_3$ electrolyte replaced pure water-electrolyte. Although, a large amount of liquid CO_2 is performed when consuming H_2O electrolyte with CO_2 bubbling but providing hydrogen ions from H_2O as an aqueous electrolyte is not enough to conduct $HCOO^-$ production on the active surface. On the contrary, 0.5 M $KHCO_3$ electrolyte can the large amount of liquid CO_2 and HCO_3^- which can enhance mass transfer diffusion and electrolytic conductivity of CO_2 RR to of $HCOO^-$ on the electrode surface.

However, the other buffer solutions were concerned to define the optimum performance of the CO_2 RR system. J. B. Vennekötter, et al. [76] examined the effect of the local environment on electrolyte to the electrochemical system. To compare the effects of pH on CO_2 conversion to CO were operated using a two-sided buffered cell. The two-sided buffered cell with directly supply gaseous CO_2 was assembled Ag-GDE as a cathode, catholyte, CEM, 0.05M H_2SO4 as anolyte, and TiO_2 coated on Pt as an anode in the x-direction from left to right. The different cathodic electrolytes displayed pHs variation consisting of a 0.5 M K_2SO_4 electrolyte (pH≤4), 0.1 M $KHCO_3$ + 0.5 M K_2SO_4 electrolyte (pH≈6.8), 1.0 M $KHCO_3$ electrolyte (pH≈8), and 2.0 M $KHCO_3$ electrolyte (pH≈8.8). The results indicated the negative cathodic potentials were decreased when increasing pHs which related to the ionic strength of the electrolyte were supplied. For instance, the FEs of CO 90% were obtained when -1.0 V vs RHE 0.5 M K_2SO_4 electrolyte, -0.95 V vs RHE 0.1 M $KHCO_3$ + 0.5 M K_2SO_4 electrolyte, -0.80 V vs RHE 1.0 M $KHCO_3$ electrolyte, and -0.81 V vs RHE 2.0 M $KHCO_3$ electrolyte. The

higher pH of the electrolyte could reduce the consumption of applied electric energies on the cathode.

The buffer solutions present the ionic strength of electrolytes. The high electrolytic conductivity of HCO_3^- displays the ohmic loss minimization in the electrolyte which leads to reducing the cathodic potential. Besides, the electrode overpotential also decreases when the cathodic electrode is used as the working electrode.

3. Cation

The effect of ionic species in the electrolyte is investigated as a function of the electrolyte composition. The significant effect of cation is derived from cation size on the product distributions of CO_2 RR [72, 73]. According to the experiment of J. Resasco et al. [77], the alkali metal cations in the electrolyte were investigated on electrochemical CO_2 to $HCOO^-$ and CO regardless of the effects of concentration and pH of the electrolyte. The polycrystalline Ag and Sn were used as electrocatalysts. The current densities of $HCOO^-$ and CO were increasing when the alkaline metal cations in the electrolyte increased ($Li^+ < Na^+ < K^+ < Rb^+ < Cs^+$). In the same way, S. Sato et al. [78] proposed electrochemical CO_2 RR with less energy consumption which used the integration of Mn-complex/multiwalled carbon nanotubes (Mn complex/MWCNT) as a cathode with K^+ cation. The integration of Mn-complex/MWCNT with K^+ cation could stabilize CO_2 taken in active sites of the electrocatalyst.

As a result, when the cation is adsorbed on the electrocatalyst surface, the cation is served as a catalyst promoter. The cation with a larger size provides a weak hydration shell of the cation which facilitates cation adsorption on the catalyst surface. Hence, the catalytic activity and selectivity can be improved by offering the electrocatalyst with a larger size of cation.

4. Anion

Anions from the dissociation of electrolyte also affect the performance of product selectivity from CO_2 RR system. From the previous details, the OH^- and HCO_3^- in alkaline electrolyte can hinder the HER because of providing high electrical conductivity and ohmic loss minimization [73, 75]. S. S. Bhargavaet al. [79] showed effect of electrolyte composition on electrochemical CO_2 RR to CO. The degree of variation of FE_{CO} relies on the anions as $Cl^- \approx CO_3^{2-} < HCO_3^- \leq OH^-$. And the degree of variation of current density of CO relies on the anions as $Cl^- < HCO_3^- < CO_3^{2-} < OH^-$. Thus, the anion which has a stronger pH-based overpotential demand provided the higher effect on current density of CO. While the anion which has a stronger specific adsorption on the electrode surface provided the higher effect on FE of CO.

The influences of other anions such as perchlorate, sulfate, phosphate, and borate on CO_2 RR to H_2 and CH_4 were also studied. M. N. Jackson et al. [80] investigated the effect of borate buffer and phosphate buffer on the Au electrode. The borate buffer and phosphate buffer were consumed as proton donors for CO_2 RR to H_2. The existence of phosphate buffer could support the HER as a proton donor better than water, but in case that borate buffer did not. Besides, the appearance of perchlorate buffer and sulfate buffer as proton donors did not support HER and CH_4. It appears that the role of the weak buffer anions which serve as a proton donor can utilize to suppress HER and CH_4 in electrochemical CO_2 reduction.

2.6 Literature reviews

To simulate the behavior of PEC CO_2 RR, the effective factors of the system were studied through many types of research. Literature reviews can provide the optimum operating conditions to model and simulate via COMSOL Multiphysics (5.6). The literature reviews were described as follows and summarized in table 12.

Table 12. Summary of literature reviews.

Main characteristics	Electrodes	Operating conditions	Main products	Efficiency	Ref.
Electrochemical reaction via MFC without membrane [Modeling]	Anode: Pt Cathode: Cu_2O-ZnO-GDE	Reactant: CO_2 saturated, Anolyte: 0.5 M $KHCO_3$, Catholyte: 0.5 M $KHCO_3$ with flow rate 20 ml/min	CH_3OH	Average error: 20.2%	Y. Kotb et al (2017), [81]
PEC reaction via flow cell assembled with based membrane cathode [Experiment]	Photoanode: WO_3/$BiVO_4$ Cathode: Ag nano cube-based membrane	Reactant: CO_2 in the gas phase, Anolyte/Catholyte: $KHCO_3$ (pH=3), Light source: 300 W Xw arc lamp, Applied voltage: >1.2 V	CO	EE: 92.1%	W. Lu et al (2020), [82]
Electrochemical reaction via MFC assembled GDE cathode and ionic liquid electrolyte [Modeling]	Anode: Pt blank, Cathode: Bi-Sn GDE	Reactant: CO2 in the gas phase, Anolyte/Catholyte: 1-ethyl(-3-methyl imidazolium tetra-fluoroborate ([EMIM][BF_4]) with flow rate 0.7 ml/min Membrane: H^+	HCOOH	Current density (CD): 60 mA/cm^2, FE: 98%, Conversion: 80%	C. Akan et al. (2019), [83]

Table 12. Summary of literature reviews (Cont.).

Main characteristics	Electrodes	Operating conditions	Main products	Efficiency	Ref.
PEC reaction via MFC, the effect of light intensity and cathode-GDE geometry [Experiment]	Photoanode: TiO$_2$ Cathode: Sn-GDE	Reactant: CO$_2$ saturated, Anolyte: 0.5 M NaOH, Catholyte: 0.5 M NaHCO$_3$, Light source: 500 mw•cm^{-2}, Applied voltage: 1.2 V Anode/Cathode area: 1:5	HCOO$^-$	FE HCOO: 64.0% EE HCOO: 70.0%	E. Irtem et al. (2017), [84]
PEC reaction via MFC, the effect of light intensity and flow rate of CO$_2$ [Modeling]	Photoanode: TiO$_2$ on FTO Cathode: Sn-GDE on carbon paper	Reactant: CO$_2$ saturated, Anolyte: 0.5 M NaOH, Catholyte: 0.5 M NaHCO$_3$, Light source: 100 mw•cm^{-2}, Applied voltage: 1.2 V Anode/Cathode area: 1:5	HCOO$^-$	High CO$_2$ flow rate: CD was increased while conversion decreased.	X. Luo et al. (2019), [35]

Table 12. Summary of literature reviews (Cont.).

Main characteristics	Electrodes	Operating conditions	Main products	Efficiency	Ref.
PEC reaction via MEA flow cell assembled with photoanode and dark cathode [Experiment]	Photoanode: TiO_2 Cathode: Cu	Reactant: CO_2 saturated, Anolyte/Catholyte: 0.1 M KOH, Light source: UV LED (100 mW•cm^{-2}), Applied voltage: >1.2 V	CH_3OH, CH_5OH	FE CH_3OH: 16.2% EE CH_3OH: 5.2% FE CH_5OH: 23.2% FE CH_5OH: 6.8%	S. Castro et al. (2020), [85]
PEC reaction via H-type cell assembled with Z-scheme (photoanode+photocathode) [Experiment]	Photoanode: TiO_2 on Pt Photocathode: InP/Ru complex	Reactant/Electrolyte: $NaHCO_3$ with flow rate 0.01 mol/l, Light source: AM 1.5G Reaction time: 24 h	$HCOO^-$	FE: >70%	T. Arai et al. (2011), [86]

The operating conditions and geometric configurations of PEC cells are also important effects on the efficiency of the process such as ion exchange membrane, gas diffusion electrode (GDE), liquid electrolyte, type of semiconductor, light intensity, flow rate, and arrangement of main components. The example of literature should be reviewed to provide the optimum parameters for modeling and simulation of the PEC CO_2 RR in the optimum.

Y. Kotb et al. [81] proposed the results from a simulation of the numerical model of electrochemical reduction of CO_2 to CH_3OH using COMSOL Multiphysics through the finite element method. The microfluidic flow cell was separated into 3 portions including the Cu_2O-ZnO gas diffusion electrode as a cathode, platinized titanium as an anode, and membrane. CO_2 was saturated and fed together with 0.5 M $KHCO_3$ as catholyte at the inlet of the cathode and 0.5 M $KHCO_3$ was also used as an anolyte to feed at the inlet of the anode with the flow rate of 20 ml/min. Then applied mass transport electrolytic species concentration, electrode reaction kinetics, and charge transport electric and ionic potential to simulate and validate comparing with the experimental data. The results from validation with the experimental data showed a 20.2% average error due to competition of hydrogen production, thus ionic conducting membranes were suggested to separate the desired product.

W. Lu et al. [82] presented the direct feeding of CO_2 in the gas phase to an Ag nanocube-based membrane cathode assembly to overcome the low solubility property in CO production. The system was set with $WO_3/BiVO_4$ photoanode, $KHCO_3$ as an electrolyte under the illumination of a 300 W Xw arc lamp as simulated light intensity to vary the applied voltages. Due to high stable molecules of CO_2, the results showed the optimum applied voltage should not be lower than 1.2 V could. The energy efficiency from the system of CO_2 reduction to CO coupled with obtained Ag nanocube-based membrane cathode assembly reached 92.1% this could provide a critical factor in the scaling-up process.

C. Akan et al. [83] evaluated a 2-dimensional numerical model to produce formic from the electrolysis of CO_2 using a microfluidic cell. This system applied CO_2 in the gas phase, Bi-Sn on GDE as cathode, Pt as an anode, and an ionic liquid as electrolyte was 1-ethyl-3-methyl imidazolium tetra-fluoroborate ($[EMIM][BF_4]$) to improve the performance of the process. The microfluidic flow cell was separated into 3 portions, cathode, anode, and proton exchange membrane. The GDEs were provided for feeding CO_2 in the gas phase at the cathode and O_2 gas at the anode, GDEs were located on the top and bottom of the membrane, respectively. The model combined thermodynamics and kinetics through the calculation of species charge transport through electrochemistry, mass conservation, and momentum conservation. The results were analyzed from model validation, mass transport, and electrochemical from the process. This model obtained 60 mA/cm^2 of current density, 98% of faradaic efficiency, and 80% of CO_2 reduction to formic acid due to suppression of hydrogen evolution reaction of ionic liquid that could use as a reference in the scaling-up process through improvement of the current density of formic acid.

E. Irtem et al. [84] investigated the effect of light intensity and geometry of cathode through PEC CO_2 conversion to $HCOO^-$ and oxygen (O_2) production at the cathode and photoanode compartments, respectively that separating by the membrane. To improve concentration and mass transfer, CO_2 in the gas phase was saturated via catholyte before feeding and circulated using a pump. The catholyte and anolyte were applied to neutral the process were 0.5 M $NaHCO_3$ and 0.5 M NaOH, respectively. The PEC CO_2 conversion was evaluated through filter-press flow cell using TiO_2-photoanode coupled with deposited Sn on GDE used as cathode under back-illumination of visible light. Besides, varying the ratio of photoanode to cathode area and light intensity were investigated to define the optimum values while the effect of electrolytes, applied cell voltage, membrane, and other operating conditions was controlled. The results showed the optimum ratio of photoanode to

cathode area and light intensity could increase faradaic efficiencies (FE) to 64% for HCOO⁻ and energy efficiencies (EE) to 70% under applied external voltages 1.2 V.

X. Luo et al. [35] developed a 2-dimensional numerical model for PEC CO_2 utilization that integrated thermodynamics and kinetics of carrier charge with electrochemical for reducing CO_2 to formic acid in form of HCOO⁻ at the cathode and oxygen evolution at the anode. The PEC flow cell was designed using TiO_2 on FTO substrates as photoanode, GDE made of carbon paper as cathode, sodium bicarbonate ($NaHCO_3$) as catholyte, sodium hydroxide ($NaOH$) as anolyte, and cationic conducting membrane under light intensity, I (100 mW•cm⁻²). The results showed optimum light intensity could improve the current density of the system, and when the flow rate of CO_2 was increased, the current density also increases. On the other hand, increasing of CO_2 flow rate would decrease the conversion efficiency of CO_2 that relied on optimum operating conditions in the system. Thus, PEC cell configuration design is still a challenge for improving the performance of PEC CO_2 RR.

S. Castro et al. [85] demonstrated by applying n-type TiO_2 photoanode coupled with Cu dark cathode to produce CH_3OH and CH_5OH through membrane electrode assembly (MEA) flow cell. Under operating conditions of UV LED light illumination (100 mW•cm⁻²) to photoanode, CO_2 was circulated using a pump passing through 0.1 M KOH for saturation before being fed to the cathode channel while the same electrolyte was circulated to the anode section. TiO_2 is widely used as an n-type semiconductor due to the appropriate bandgap that can provide light adsorption in the range of ultraviolet (UV). TiO_2 is a less expensive and environmentally friendly material. In addition, Cu was reviewed as the high-performance catalyst for hydrocarbon and alcohol production. The results showed the maximum production rate, faradaic efficiency, and energy efficiency of CH_3OH equaled 9.5×10^{-6} mol/m²s, 16.2%, and 5.2%, respectively. And the maximum production rate, faradaic efficiency, and energy efficiency of CH_5OH equaled 6.8×10^{-6} mol/m²s, 23.2%, and 6.8%, respectively.

Chapter 3

METHODOLOGY

3.1 Model description of PEC cell for CO_2 RR

To evaluate the effectiveness of the geometric configuration of the PEC cell for CO_2 RR, the COMSOL Multiphysics (5.6) is used to simulate the different configurations of PEC cells. The main components of the PEC cell with specified geometry are designed and rearranged as below.

3.1.1 Microfluidic flow cell (MFC)

The MFC is designed for CO_2 RR. CO_2 in the gas phase is directly fed to SnO_2-cathode through the inlet of the gas feed channel while 0.5 M KOH and 0.5 M $KHCO_3$ are used as anolyte and catholyte which are fed to the inlet of the electrolyte channels. The inlet of electrolyte and gas flow channel are placed from the bottom to the top along the length of the cell in y-direction. The MFC is simulated using COMSOL Multiphysics (5.6) with a stationary initialization study using a finite element numerical simulation model to simulate the behavior of MFC. As shown in figure 20, the 2-dimensional model of the MFC cell can be divided into 6 domains from left to right along the width of the cell in x-direction including TiO_2-photoanode, anolyte channel, PEM, catholyte channel, SnO_2-cathode, and gas channel, respectively.
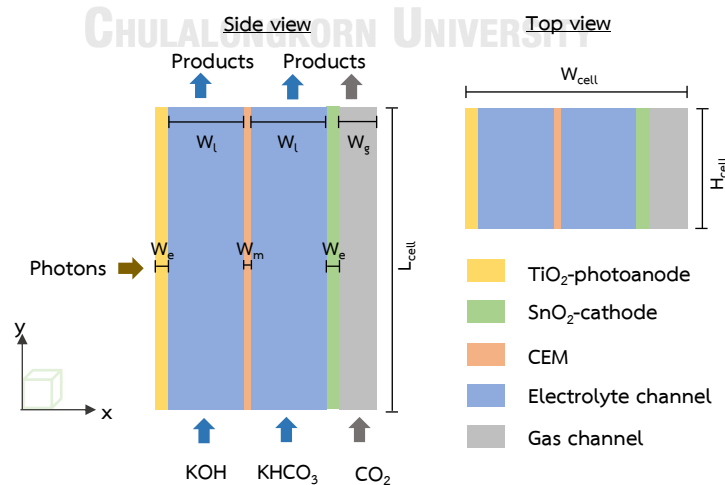
Figure 20. Schematic diagram of the microfluidic flow cell (MFC) for CO_2 RR.

The flow rate of reactants is assumed to be in the range of the laminar regime. CO_2 in the gas phase is assumed as a weakly compressible fluid while liquid electrolyte is assumed as an incompressible fluid. In addition, TiO_2 is used as a photocatalyst for a back illumination at the photoanode, SnO_2 is used as an electrocatalyst for CO_2 RR at the cathode, and Nafion 117 is used as a product separator to transfer H^+ from the anodic compartment to the cathodic compartment. Also, the CO_2 RR and OER will occur at the interface of the deposited catalyst on cathode/electrolyte and the deposited photocatalyst on anode/electrolyte, respectively. Thus, a constant flux photocurrent density is consumed to drive the reaction. The transport of concentrated species and Brinkman's equation are used to simulate the transportation of gas species in GDE. Tertiary current distribution (TCD) is used to analyze the kinetics of all charge species on the photoanode, cathode, and in electrolyte, while Secondary current distribution (SCD) is used for the PEM. To maintain the species flux of reactants and continuity of reactions, Danckwert's boundary condition is provided at the inlets of the cell. Moreover, Nernst Plank's equation and Butler-Volmer's equation are applied to simulate electric charge transport in the cell and reaction behavior on the interface electrode/electrolyte.

3.1.2 Membrane electrode assembly flow cell (MEAFC)

The MEAFC is designed for CO_2 RR. CO_2 in the gas phase is saturated in the catholyte of 0.5 M $KHCO_3$ and is fed to the inlet of the catholyte channel and circulated to avoid bubble formation using a pump. And 0.5 M KOH is used as an anolyte. The inlets of anolyte and catholyte channels are placed from the bottom to the top along the length of the cell in y-direction. Similarly, the MEAFC is simulated using COMSOL Multiphysics (5.6) with a stationary initialization study using a finite element numerical simulation model to simulate the behavior of MEAFC. As shown in figure 21, the 2-dimensional model of the MEAFC cell can be divided into 5 domains from left to right along the width of the cell in x-direction, including anolyte

channel, TiO_2-photoanode, PEM, SnO_2-cathode, catholyte channel, and gas channel, respectively.
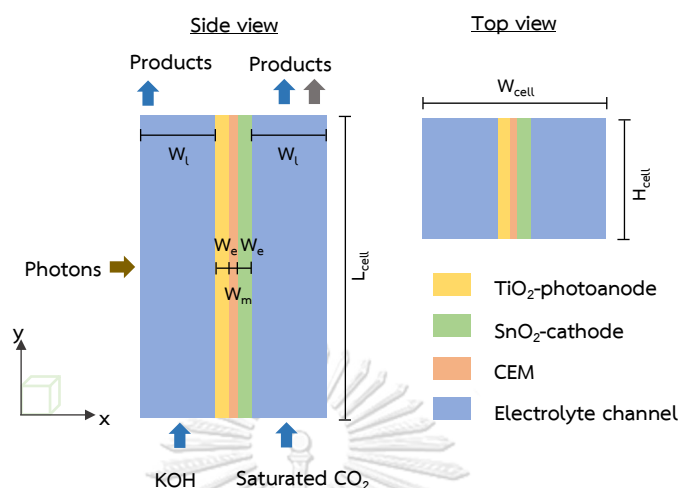
Figure 21. Schematic diagram of the membrane electrode assembly flow cell (MEAFC) for CO_2 RR.

The flow rate of reactants is assumed to be in the range of the laminar regime. CO_2 in the saturated phase and liquid electrolyte are assumed as an incompressible fluid. In addition, TiO_2 is used as a photocatalyst for a back illumination at the photoanode, SnO_2 is used as an electrocatalyst for CO_2 RR at the cathode, and Nafion 117 is used as a product separator to transfer H^+ from the anodic to the cathodic compartment. Also, the CO_2 RR and OER will occur at the interface of deposited catalyst on cathode/electrolyte and deposited photocatalyst on anode/electrolyte, respectively. A constant flux photocurrent density is consumed to drive the reaction. Tertiary current distribution (TCD) is used to analyze the kinetics of all charge species on the photoanode, cathode, and in electrolyte, while Secondary current distribution (SCD) is used for the PEM. To maintain the species flux of reactants and continuity of reactions, Danckwert's boundary condition is provided at the inlets of the cell. Moreover, Nernst Plank's equation and Butler-Volmer's equation are applied to simulate electric charge transport in the cell and reaction behavior on the interface electrode/electrolyte.

3.1.3 Microfluid flow cell (MFC) with a zero-gap anode

The MFC with a zero-gap anode is designed for CO_2 RR. CO_2 in the gas phase is directly fed to SnO_2-cathode through the inlet of the gas feed channel. 0.5 M KOH and 0.5 M $KHCO_3$, are used as anolyte and catholyte which are fed to the inlet of the electrolyte channels. The inlet of electrolyte and gas flow channel are placed from the bottom to the top along the length of the cell in y-direction. The MFC with a zero-gap anode is simulated using COMSOL Multiphysics (5.6) with a stationary initialization study using a finite element numerical simulation model to simulate the behavior of MFC with a zero-gap anode. As shown in figure 22, the 2-dimensional model of the MFC cell can be divided into 6 domains from left to right along the width of the cell in x-direction including anolyte channel, TiO_2-photoanode, PEM, catholyte channel, SnO_2-cathode, and gas channel, respectively.
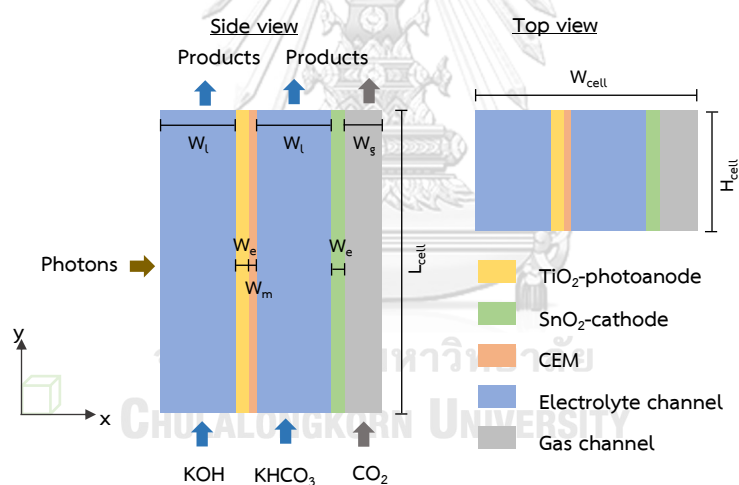
Figure 22. Schematic diagram of the microfluidic flow cell (MFC) with a zero-gap anode for CO_2 RR.

The flow rate of reactants is assumed to be in the range of the laminar regime. CO_2 in the gas phase is assumed as a weakly compressible fluid while liquid electrolyte is assumed as an incompressible fluid. In addition, TiO_2 is used as a photocatalyst for a back illumination at the photoanode, SnO_2 is used as an electrocatalyst for CO_2 RR at the cathode, and Nafion 117 is used as a product separator to transfer H^+ from the anodic to the cathodic compartment. Also, the CO_2

RR and OER will occur at the interface of deposited catalyst on cathode/electrolyte and deposited photocatalyst on anode/electrolyte, respectively. A constant flux photocurrent density is consumed to drive the reaction. The transport of concentrated species and Brinkman's equation are used to simulate the transportation of gas species in GDE. Tertiary current distribution (TCD) is used to analyze the kinetics of all charge species on the photoanode, cathode, and electrolyte, while Secondary current distribution (SCD) is used for the PEM. To maintain the species flux of reactants and continuity of reactions, Danckwert's boundary condition is provided at the inlets of the cell. Moreover, Nernst Plank's equation and Butler-Volmer's equation are applied to simulate electric charge transport in the cell and reaction behavior on the interface electrode/electrolyte.

3.2 Photoelectrochemical reactions

The PEC CO_2 RR is simulated through COMSOL Multiphysics (5.6) including the reactions at the interface of photoanode/anolyte, the interface of cathode/catholyte, and electrolyte compartments.

3.2.1 Half-cell reactions at the photoanode

1. Light absorption

For this system, the light absorption has larger energy than the bandgap of TiO_2-photoanode (3.0-3.2 eV) and is sufficient for electric species transportation to generate electron (e^-) and hole (h^+) pairs at the photoanode as shown in reaction (18).

$$\text{Light absorption:} \qquad \text{semiconductor} \rightarrow e^- + h^+ \qquad (18)$$

2. Oxygen evolution reaction (OER)

Simultaneously, the oxygen gas (O_2) and water (H_2O) were formed on the interface of photoanode/anolyte with the electrode potential (E^0) equal to 0.82 V (referred to SHE). The OER is shown as reaction (19).

$$\text{OER:} \qquad 2OH^- \rightarrow O_2 + H_2O + 2e^- \qquad (19)$$
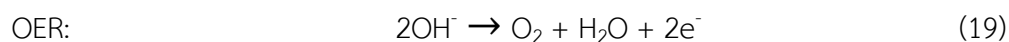
3.2.2 Half-cell reactions at the cathode

1. CO$_2$ RR

The reactions (20) and (21) show the formation of HCOO$^-$ and CO because of multi-electron consumption of CO$_2$ RR at the interface of cathode/catholyte with E^0 equal to -0.43 V and -0.53 V vs SHE, respectively.

CO$_2$ RR to HCOO$^-$:   CO$_2$ + H$_2$O + 2e$^-$ $\rightarrow$ HCOO$^-$ + OH$^-$ (20)

CO$_2$ RR to CO: CO$_2$ + H$_2$O + 2e$^-$ $\rightarrow$ CO + 2OH$^-$ (21)
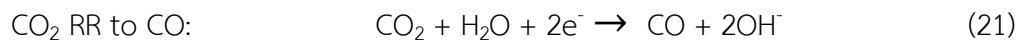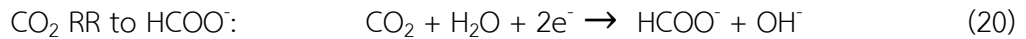
2. Hydrogen evolution reaction (HER)

The hydrogen gas (H$_2$) is the product from HER at the interface of cathode/catholyte with E^0 equal to -0.41 V vs SHE that can decrease the faradaic efficiency and current density of HCOO$^-$ and CO formation. H$_2$ formation is shown as reaction (22).

HER: 2H$_2$O + 2e$^-$ $\rightarrow$ H$_2$ + 2OH$^-$ (22)

3.2.3 Dissolution of the CO$_2$ in the aqueous electrolyte

Apart from the reactions on the electrode surface, the equilibrium reactions and rate constants of KHCO$_3$ and KOH dissociation are shown in reactions (23) to (28).

CO$_2$ + H$_2$O $\leftrightarrow$ H$^+$ + HCO$_3^-$ K_{23f} = 0.036 s^{-1} K_{23b} = 7.83x10^1 m$^3 \cdot$mol$^{-1} \cdot$s^{-1} (23)

CO$_2$ + OH$^-$ $\leftrightarrow$ HCO$_3^-$ k_{24f} = 5.93 m$^3 \cdot$mol$^{-1} \cdot$s^{-1} k_{24b} = 1.34x10^{-4} s^{-1} (24)

HCO$_3^-$ $\leftrightarrow$ H$^+$ + CO$_3^{2-}$ k_{25f} = 2.50 s^{-1} k_{25b} = 5x10^4 m$^3 \cdot$mol$^{-1} \cdot$s^{-1} (25)

HCO$_3^-$ + OH$^-$ $\leftrightarrow$ H$_2$O + CO$_3^{2-}$ k_{26f} =6x10^{6}m$^3 \cdot$mol$^{-1} \cdot$s^{-1} k_{26b} = 1.28 x10^6 s^{-1} (26)

H$_2$O $\leftrightarrow$ H$^+$ + OH$^-$ K_w = 1.00x10^8 m$^6 \cdot$mol$^{-2} \cdot$s^{-1} (27)

KOH $\rightarrow$ K$^+$ + OH$^-$ (28)
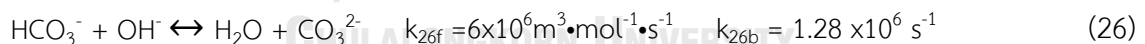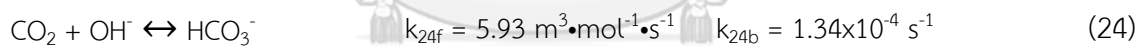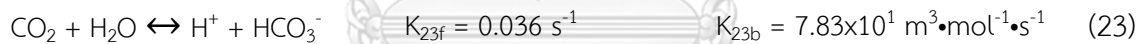
3.3 Model assumptions

The main assumptions are identified to support the physics model simulation as follows:

1. The main physics model simulation for the PEC cell is at steady-state condition. In contrast, only a few time-dependent (transient) conditions are used for comparison purposes.

2. The system is isothermal. The temperature variation across the PEC cell is relatively low because of the flowing of liquid electrolytes which is a good thermal conductor.

3. The variations across the cell height are negligible to simplify the model. The 2-dimensional model is sufficient.

4. The current collectors are treated as the interfaces between the electrode and electrolyte that occurred electrochemical reactions. Therefore, the ohmic loss across the current collectors is insignificant.

5. Butler Volmer equation is applied to describe the rate of electrochemical reactions.

6. A laminar flow regime is used for fluid flow with controlled velocity. Flow in the gas channel is weakly compressible and the flow in the electrolyte channel is incompressible.

7. The effect of bubble formation is insignificant due to the short simulation time. The effective crossover flux of gas species (CO_2, CO, H_2, O_2, and N_2) at the electrochemical interfaces is negligible.

8. The GDEs are treated as homogeneous porous media of the gas diffusion layers (GDLs) and the catalyst layers (CLs). Thus, the average porosity and permeability are used to simulate.

3.4 Modeling equations

The governing equations are applied in each domain to simulate mass balance and transportation of species, and electrochemical kinetics of ionic charge species from CO_2 RR in PEC cell. In section 3.4, the modeling equations and input parameters are presented.

3.4.1 Photocurrent density

To decrease the electrical energy consumption for CO_2 utilization, solar energy is provided in which the calculation of photocurrent density has calculated based on the correlation with a wavelength of absorbed light, as expressed in Eq. (6).

$$i = q \int_{\lambda_1}^{\lambda_2} \frac{L\lambda}{hc} \, d\lambda \qquad \text{Eq. (6)}$$

where i is the incident photocurrent density (A/m^2)

q is elementary charge (1.6022×10^{-19} C)

λ is the wavelength of absorbed light (m)

h is Planck's constant (6.626×10^{-34} m^2·kg/s)

c is light velocity (2.998×10^{8} m/s)

L is light transmission loss through the reactor materials

The correlation between the average electrode power density, electric potential, and current density is described in Eq. (7) which is integrated over the boundary to set at the interface between the electrode and the current collector.

$$\int (\phi_s - \phi_{s,ground})(i \cdot n) dS = P_{avg} A \qquad \text{Eq. (7)}$$

where P_{avg} is the average power density (W/m^2)

A is the boundary area

ϕ_s is the electric potential (V)

ϕ_s is the ground potential of the cell (V)

i is the current density vector (A/m^2)

n is the normal vector of the boundary pointing into the domain

Note that the boundary electric potential, $\phi_{s,bnd}$ is set as an initial value to support during the discharge of a PEC cell which provides a maximum power level. The decreasing of output power will occur when the power level over increasing of current which leads to a loss more voltage.

3.4.2 Fluid flow

The continuity equation and Navier-Stokes equations are used to express the mass conservation and species transport of momentum, respectively. The system is assumed to be isothermal and a steady state.

1. Gas channel

The physics models for fluid motion in gas channel include laminar flow and transport of concentrated species. The gas is assumed to be a weakly compressible fluid. The overall mass and momentum conservation equations are expressed by Eq. (8) and (9).

$$\nabla \cdot (\rho_g u_g) = 0 \qquad \text{Eq. (8)}$$

$$\rho_g u_g \cdot \nabla u_g = \rho_g g - \nabla p_g + \nabla \cdot (\mu_g(\nabla u_g + (\nabla u_g)^\tau)$$
$$- \frac{2}{3}\mu_g(\nabla \cdot u_g)I) \qquad \text{Eq. (9)}$$

where p_g is the gas pressure (Pa)

ρ_g is the gas density (kg•m^{-3})

u_g is the velocity vector (m•s^{-1})

μ_g is dynamic gas viscosity (kg•m^{-1}•s^{-1})

g is gravitational acceleration (m^2•s^{-1})

I is the identity tensor

Transport of concentration species consisting of CO_2, CO, H_2, H_2O and N_2 for cathode gas and O_2, H_2O and N_2 for anode gas. The Maxwell-Stefan equation is applied to define total mass flux species in mass conservation equation are expressed by Eq. (10) and (11).

$$\nabla \cdot n_{i,g} = 0 \qquad \text{Eq. (10)}$$

$$n_{i,g} = -\rho_g \omega_i \sum_{j=1}^{N} D_{ij} \left[\frac{M_g}{M_i} \left(\nabla \omega_j + \omega_j \frac{\nabla M_g}{M_g} \right) + (x_j - \omega_j) \frac{\nabla p_g}{p_g} \right]$$

$$+ \rho_g u_g \omega_i \qquad \text{Eq. (11)}$$

where n_i is the total mass flux of gas species

ω_i is the mass fraction

x_j is the molar fraction

M_g is molar mass of gas mixture

D_{ij} is the diffusion coefficient ($m^2 \cdot s^{-1}$)

The molar mass of gas mixture, M_g is defined as the sum of molar mass of gases in the system, as shown in Eq (12).

$$M_g = x_{CO_2} M_{CO_2} + x_{CO} M_{CO} + x_{H_2} M_{H_2} + x_{H_2O} M_{H_2O} \; x_{N_2} M_{N_2}$$

$$\text{Eq. (12)}$$

The diffusion coefficient of multicomponent can be determined using the correlation of Fuller, Schettler, and Giddings, as shown in Eq (13).

$$D_{ij} = \frac{10^{-3} T^{1.75} \left(\frac{1}{M_i} + \frac{1}{M_j} \right)^{1/2}}{p \left(v_i^{1/3} + v_j^{1/3} \right)} \qquad \text{Eq. (13)}$$

where D_{ij} is multicomponent diffusion coefficient ($cm^2 \cdot s^{-1}$)

T is temperature (K)

p is the pressure (atm)

v_i is the diffusion volume for molecule i

M_i is molecular weight of gas i ($g \cdot mol^{-1}$)

2. Gas diffusion electrode (GDE)

The physics models for reacting flow in GDE include Brinkman's equation and transport of concentrated species in porous media. The gas is assumed to be a

weakly compressible fluid, the continuity of mass and momentum balance equations are expressed by Eq. (14) and (15).

$$\nabla \cdot (\rho_g u_g) = Q \qquad \text{Eq. (14)}$$

$$\rho_g u_g \cdot \nabla u_g = \rho_g g - \nabla p_g + \nabla \cdot [\frac{1}{\varepsilon}(\mu_g(\nabla u_g + (\nabla u_g)^\tau$$
$$- \frac{2}{3}\mu_g(\nabla \cdot u_g)I)] - \left(\frac{\mu_g}{\kappa}\right)u_g \qquad \text{Eq. (15)}$$

where Q is the mass source term which presents in occurred electrochemical reaction position.

ε is porosity of GDE

τ is tortuosity

κ is permeability of the GDL or catalyst layer (m^2).

For the continuity mass flux species, the equations are expressed by Eq. (16) and (17).

$$\nabla \cdot n_{i,g} = R_{i,g} \qquad \text{Eq. (16)}$$

$$n_{i,g} = -\rho_g \omega_i \sum_{j=1}^{N} D_{ij}^{eff} \left[\frac{M_g}{M_i}\left(\nabla\omega_j + \omega_j \frac{\nabla M_g}{M_g}\right) + \left(x_j - \omega_j\right)\frac{\nabla p_g}{p_g}\right] + \rho_g u_g \omega_i \qquad \text{Eq. (17)}$$

where R_i is the reaction rate of gas species

D_{ij}^{eff} is the effective gas diffusion coefficient (m^2•s^{-1})

The effective gas diffusion coefficient of multicomponent can be determined using the Bruggeman correction is shown in Eq (18).

$$D_{ij}^{eff} = \varepsilon^{1.5}D_{ij} \qquad \text{Eq. (18)}$$

3. Electrolyte channel

For liquid electrolytes, the motion of incompressible fluid with laminar flow in electrolyte channel. The overall mass and momentum conservation equations are expressed by Eq. (19) and (20).

$$\rho_l \nabla \cdot u_l = 0 \qquad \text{Eq. (19)}$$

$$\rho_l (u_l \cdot \nabla) u_l = \rho_l g - \nabla p_l I + \nabla \cdot (\mu_l (\nabla u_l + (\nabla u_l)^T \qquad \text{Eq. (20)}$$

where p_l is the liquid electrolyte pressure (Pa)

ρ_l is the gas density (kg•m^{-3})

u_l is the velocity vector (m•s^{-1})

μ_l is dynamic gas viscosity (kg•m^{-1}•s^{-1})

To control the flow regime of fluid to be laminar flow, the inlet of fluid velocity is identified from the Reynold numbers (Re) given by Eq. (21).

$$u = \frac{\mu Re}{\rho L} \qquad \text{Eq. (21)}$$

where u is fluid velocity (m•s^{-1})

μ is dynamic fluid viscosity (kg•m^{-1}•s^{-1})

Re is Reynold numbers (Re<2000)

L is characteristic length (m)

ρ is fluid density (kg•m^{-3})

3.4.3 Charge transport/ Ionic migration

The mass transport of the dissolved species in the electrolyte or a component in a gas mixture is balanced as shown in Eq. (22).

$$\nabla \cdot n_i = R_i \qquad \text{Eq. (22)}$$

where n_i is the total mass flux of ionic species (mol/m^2•s)

R_i is the term of reaction source/sink of ionic species

The Nernst-Planck equation is applied to examine species transport in terms of diffusion, electric charge migration, and convection, as shown in Eq. (23).

$$n_i = -D_i \nabla c_i - z_i u_{mi} F c_i \nabla \phi_{l,e} + u c_i \qquad \text{Eq. (23)}$$

The dissolved species in the electrolyte consist of CO_2, K^+, HCO_3^-, H^+, OH^-, CO_3^{2-}, $HCOO^-$, CO, H_2 and O_2.

where D_i is diffusion coefficient of dissolved species ($m^2 \cdot s^{-1}$)

c_i is species concentration ($mol \cdot m^{-3}$)

z_i is charge number of dissolved species

u_{mi} is species mobility of dissolved species ($m^2 \cdot V^{-1} \cdot s^{-1}$)

F is Faraday's constant (96485 Coulomb$\cdot$mol^{-1})

$\phi_{l,e}$ is electrolyte potential (V)

Faraday's law and Ohm's law were applied to identify the charge balance in the electrolyte channel, as shown in Eq. (24).

$$i_{l,e} = F \sum_i z_i R_i \qquad \text{Eq. (24)}$$

Due to the charge conservation as Eq. (25), the current of the electrolyte is provided by Ohm's law, as shown in Eq. (26):

$$\nabla \cdot i_{l,e} = 0 \qquad \text{Eq. (25)}$$

$$i_{l,e} = F \sum_i z_i (-D_i \nabla c_i - z_i u_{mi} F c_i \nabla \phi_{l,e}) \qquad \text{Eq. (26)}$$

where $i_{l,e}$ is the current density in the electrolyte ($A \cdot m^{-2}$)

In the electrolyte channels, the electroneutrality condition is applied as described by the following Eq. (27).

$$\sum_i z_i c_i = 0 \qquad \text{Eq. (27)}$$

In the membrane, H^+ is transferred from the anode to the cathode compartment while the negative ions concentration is set as constant. Thus, the species flux of electroneutrality and electric conductivity in the membrane are expressed as Eq. (28) and (29).

$$n_{H^+} = -z_i u_{mi} F c_i \nabla \phi_{l,m} \qquad \text{Eq. (28)}$$

$$i_{l,m} = -\sigma_{l,m} \nabla \phi_{l,e} \qquad \text{Eq. (29)}$$

where $i_{l,m}$ is the current density in the membrane (A•m^{-2})

$\sigma_{l,m}$ is ionic conductivity of membrane (S•m^{-1})

For the electrodes, a gas mixture is transported by diffusion and convection by following Eq. (30) and (31) in the cathode and anode, respectively.

$$n_i = -\rho D \nabla \omega_i + \rho u \omega_i \qquad \text{Eq. (30)}$$

$$n_i = -\rho D \nabla \omega_i \qquad \text{Eq. (31)}$$

Note that the gas species at the cathode and the anode consist of CO_2, CO, H_2, H_2O, and O_2.

And the current density at the electrodes is imposed by Ohm's law, as shown in Eq. (32).

$$i_s = -\sigma_s \nabla \phi_s \qquad \text{Eq. (32)}$$

where i_s is the current density at the electrodes (A•m^{-2})

σ_s is electronic conductivity of electrodes (S•m^{-1})

3.4.4 Electrochemical kinetics

The kinetics of electrochemical reaction could be expressed using the Butler-Volmer equation. The local current density of products (i_{local}) from CO_2 RR is given by Eq. (33).

$$i_i = k_i \left[c_R \, exp\left(\frac{\alpha_a F \eta}{RT}\right) - c_O \, exp\left(\frac{-\alpha_c F \eta}{RT}\right) \right] \qquad \text{Eq. (33)}$$

where i_i is the local charge transfer current density for the reaction (A•m^{-2})

k_i is the kinetic pre-exponential parameter for specific reaction

c_R is reduced species expression

c_O is oxidized species expression

α_a is anodic charge transfer coefficient

α_c is cathodic charge transfer coefficient

R is the gas constant (8.314 J•mol^{-1}•K^{-1})

T is the operating temperature (K)

η is the overpotential (V)

The kinetic pre-exponential parameter (k_i) is obtained from laboratory experiment set up where k_i can be presented by a reference exchange current density for specific reaction (i_i^{ref}). In addition, due to the rate reactions of CO_2 RR in reactions (20) and (21) at the cathode, local concentration of CO_2 and C_R is defined to be 0. The current densities transport of HCOO$^-$ and CO are given by following Eq. (34) and (35).

$$i_{HCOO^-} = i_{HCOO^-}^{ref} \frac{c_{CO_2}}{c_{CO_2,ref}} exp\left(-\frac{2\alpha_{HCOO^-}F}{RT}\eta_{HCOO^-}\right) \qquad \text{Eq. (34)}$$

$$i_{CO} = i_{CO}^{ref} \frac{c_{CO_2}}{c_{CO_2,ref}} exp\left(-\frac{2\alpha_{CO}F}{RT}\eta_{CO}\right) \qquad \text{Eq. (35)}$$

where c_{CO_2} is the CO_2 concentrations is to be reduced.

$c_{CO_2,ref}$ is the reference CO_2 concentrations

The reactions (19) and (22) are mass transfer-independent, therefore the current densities of H_2 and O_2 can be written as following Eq. (36) and (37).

$$i_{H_2} = i_{H_2}^{ref} exp\left(-\frac{2\alpha_{H_2}F}{RT}\eta_{H_2}\right) \qquad \text{Eq. (36)}$$

$$i_{O_2} = i_{O_2}^{ref} exp\left(\frac{2\alpha_{O_2}F}{RT}\eta_{O_2}\right) \qquad \text{Eq. (37)}$$

The overpotential (η) of the species is given in correlation with cell voltage as Eq. (38) or (39).

$$V_{cell} = (E_a^0 - E_c^0) + (\eta_a + \eta_c) + \eta_{ohm} \qquad \text{Eq. (38)}$$

$$\eta = \phi_s - \phi_l - \phi_0 \qquad \text{Eq. (39)}$$

where V_{cell} is cell potential (V)

E_a^0 is equilibrium cell potential at anode (V)

E_c^0 is equilibrium cell potential at cathode (V)

η_{ohm} is ohmic drop

η_a is anodic overpotential

η_c is cathodic overpotential

ϕ_s is electric potential (V)

ϕ_l is electrolyte potential (V)

ϕ_0 is equilibrium potential (V)

Therefore, the rate of electrochemical reactions at the interface od electrodes expressed as R_i is shown in Eq. (40).

$$R_i = \frac{v_i i_i}{n_{i,e}\, F} \qquad\qquad \text{Eq. (40)}$$

where v_i is the stoichiometric coefficient of the species i in the reaction

$n_{i,e}$ is the number of the electrons

Table 13. Modeling parameters of PEC cell for CO_2 RR.

Parameters		Symbol	Value	Unit	Ref.
Operating conditions					
Temperature		T	298.15	K	
Exit pressure		P_{exit}	101.33×10^3	Pa	
Electric potential, initial value		$\phi_{s,bnd,int}$	1.5	V	
Applied photocurrent density		i_{cell}	1.0	A•m^{-2}	
Inlet electrolyte velocity		U_l	7.40×10^{-3}	m•s^{-1}	
Inlet gas velocity		U_g	7.40×10^{-3}	m•s^{-1}	
Geometric details					
Cell length		L_{cell}	0.03	m	
Cell height		H_{cell}	0.015	m	
Gas channel width		W_g	1.50×10^{-3}	m	
Electrolyte channel width		W_l	1.50×10^{-3}	m	
GDE width		W_e	3.30×10^{-4}	m	[87]
Membrane width		W_m	1.83×10^{-4}	m	[88]
Gas properties					
Gas viscosity		μ_g	1.665×10^{-5}	Pa•s	[89, 90]
Gas density		ρ_g	1.410	kg•m^{-3}	[90, 91]
Inlet CO_2 mass fraction		ω_{CO_2}	0.56	-	
Diffusion coefficient of CO_2/CO		D_{CO_2CO}	9.14×10^{-5}	m^2•s^{-1}	
Diffusion coefficient of CO_2/H_2		$D_{CO_2H_2}$	3.20×10^{-4}	m^2•s^{-1}	
Diffusion coefficient of CO_2/N_2		$D_{CO_2N_2}$	9.21×10^{-5}	m^2•s^{-1}	
Diffusion coefficient of CO_2/O_2		$D_{CO_2O_2}$	8.96×10^{-5}	m^2•s^{-1}	
Diffusion coefficient of CO_2/H_2O		$D_{CO_2H_2O}$	1.12×10^{-4}	m^2•s^{-1}	
Diffusion coefficient of CO/H_2		D_{COH_2}	3.47×10^{-4}	m^2•s^{-1}	
Diffusion coefficient of CO/N_2		D_{CON_2}	1.08×10^{-4}	m^2•s^{-1}	
Diffusion coefficient of CO/O_2		D_{COO_2}	1.06×10^{-4}	m^2•s^{-1}	
Diffusion coefficient of CO/H_2O		D_{COH_2O}	1.29×10^{-4}	m^2•s^{-1}	
Diffusion coefficient of N_2/H_2		$D_{N_2H_2}$	3.51×10^{-4}	m^2•s^{-1}	

Table 13. Modeling parameters of PEC cell for CO_2 RR (Cont.).

Parameters		Symbol	Value	Unit	Ref.
Gas properties					
Diffusion coefficient of N_2/O_2		$D_{N_2O_2}$	1.07×10^{-4}	$m^2 \cdot s^{-1}$	
Diffusion coefficient of N_2/H_2O		$D_{N_2H_2O}$	1.31×10^{-4}	$m^2 \cdot s^{-1}$	
Diffusion coefficient of H_2/H_2O		$D_{H_2H_2O}$	3.82×10^{-4}	$m^2 \cdot s^{-1}$	
Diffusion coefficient of O_2/H_2O		$D_{O_2H_2O}$	1.29×10^{-4}	$m^2 \cdot s^{-1}$	
Electrolyte properties					
Electrolyte viscosity, $KHCO_3$		$\mu_{l,c}$	0.91×10^{-3}	Pa•s	[92]
Electrolyte viscosity, KOH		$\mu_{l,a}$	0.95×10^{-3}	Pa•s	[93]
Electrolyte density, $KHCO_3$		$\rho_{l,c}$	1030.00	$kg \cdot m^{-3}$	[94]
Electrolyte density, KOH		$\rho_{l,a}$	1021.70	$kg \cdot m^{-3}$	[93]
Initial $KHCO_3$ concentration		c_{KHCO_3}	500.00	$mol \cdot m^{-3}$	
Initial KOH concentration		c_{KOH}	500.00	$mol \cdot m^{-3}$	
Initial H^+ concentration		$c_{H^+,a}$	2.04×10^{-11}	$mol \cdot m^{-3}$	
Initial OH^- concentration	Anode	$c_{OH^-,a}$	500.00	$mol \cdot m^{-3}$	
Initial K^+ concentration		$c_{K^+,a}$	500.00	$mol \cdot m^{-3}$	
Initial O_2 concentration		$c_{O_2,a}$	1.00×10^{-5}	$mol \cdot m^{-3}$	
Initial CO_2 concentration		$c_{CO_2,c}$	26.17	$mol \cdot m^{-3}$	
Initial CO_3^{2-} concentration		$c_{CO_3^{2-},c}$	9.12×10^{-1}	$mol \cdot m^{-3}$	
Initial HCO_3^- concentration		$c_{HCO_3^-,c}$	484.00	$mol \cdot m^{-3}$	
Initial H^+ concentration	Cathode	$c_{H^+,c}$	2.49×10^{-5}	$mol \cdot m^{-3}$	
Initial OH^- concentration		$c_{OH^-,c}$	4.02×10^{-4}	$mol \cdot m^{-3}$	
Initial K^+ concentration		$c_{K^+,c}$	485.82	$mol \cdot m^{-3}$	
Initial $HCOO^-$ concentration		$c_{HCOO^-,c}$	1.00×10^{-8}	$mol \cdot m^{-3}$	
Initial CO concentration		$c_{CO,c}$	1.00×10^{-8}	$mol \cdot m^{-3}$	
Initial H_2 concentration		$c_{H_2,a}$	1.00×10^{-8}	$mol \cdot m^{-3}$	
Diffusion coefficient of CO_2		D_{CO_2}	1.91×10^{-9}	$m^2 \cdot s^{-1}$	
Diffusion coefficient of CO_3^{2-}		$D_{CO_3^{2-}}$	9.23×10^{-10}	$m^2 \cdot s^{-1}$	[95]
Diffusion coefficient of HCO_3^-		$D_{HCO_3^-}$	1.19×10^{-9}	$m^2 \cdot s^{-1}$	

Table 13. Modeling parameters of PEC cell for CO_2 RR (Cont.).

Parameters		Symbol	Value	Unit	Ref.
Electrolyte properties					
Diffusion coefficient of H^+		D_{H^+}	9.30×10^{-9}	$m^2 \bullet s^{-1}$	
Diffusion coefficient of OH^-		D_{OH^-}	5.30×10^{-9}	$m^2 \bullet s^{-1}$	[95]
Diffusion coefficient of K^+		D_{K^+}	1.96×10^{-9}	$m^2 \bullet s^{-1}$	
Diffusion coefficient of $HCOO^-$		D_{HCOO^-}	1.50×10^{-9}	$m^2 \bullet s^{-1}$	
Diffusion coefficient of CO		D_{CO}	2.03×10^{-9}	$m^2 \bullet s^{-1}$	
Diffusion coefficient of H_2		D_{H_2}	4.5×10^{-9}	$m^2 \bullet s^{-1}$	[96]
Diffusion coefficient of O_2		D_{O_2}	2.01×10^{-9}	$m^2 \bullet s^{-1}$	
Membrane properties					
Diffusion coefficient of membrane		$D_{H^+,m}$	9.30×10^{-9}	$m^2 \bullet s^{-1}$	[97]
Ionic conductivity of membrane		σ_m	1.30	$S \bullet m^{-1}$	[98]
Membrane activity		$c_{H^+,m}$	1.00×10^3	$mol \bullet m^{-3}$	[99]
Electrode properties					
Resistivity of TiO_2	Anode	R_{TiO_2}	3.00×10^{-5}	$\Omega \bullet m^2$	[100]
Resistivity of SnO_2		R_{SnO_2}	6.67×10^{-7}	$\Omega \bullet m^2$	[101]
Electrode conductivity of electrode		σ_e	100.00	$S \bullet m^{-1}$	[95]
Porosity of electrode GDE	Cathode	ε_e	0.66	-	[69]
Porosity of catalyst layer		ε_{cl}	0.40	-	
Permeability of electrode GDE		κ_e	2.49×10^{-12}	m^2	
Electrochemical reaction kinetic parameters					
Equilibrium potential of half-cell reaction	Anode	$E^0_{O_2}$	0.82	V vs NHE	
	Cathode	$E^0_{HCOO^-}$	-0.61	V vs NHE	[96]
		E^0_{CO}	-0.53	V vs NHE	
		$E^0_{H_2}$	-0.41	V vs NHE	

Table 13. Modeling parameters of PEC cell for CO_2 RR (Cont.).

Parameters		Symbol	Value	Unit	Ref.
Electrochemical reaction kinetic parameters					
Equilibrium potential of half-cell reactions	Anode	$E_{O_2}^0$	0.82	V vs NHE	[96]
	Cathode	$E_{HCOO^-}^0$	-0.61	V vs NHE	
		E_{CO}^0	-0.53	V vs NHE	
		$E_{H_2}^0$	-0.41	V vs NHE	
Exchange current densities	Anode	$i_{O_2}^{ref}$	1	A•m^{-2}	
	Cathode	$i_{HCOO^-}^{ref}$	4.33×10^{-7}	A•m^{-2}	
		i_{CO}^{ref}	1.40×10^{-3}	A•m^{-2}	
		$i_{H_2}^{ref}$	6.91×10^{-7}	A•m^{-2}	
Transfer coefficients	Anode	α_{O_2}	0.5	-	
	Cathode	α_{HCOO^-}	0.472	-	
		α_{CO}	0.1946	-	
		α_{H_2}	0.3182	-	

จุฬาลงกรณ์มหาวิทยาลัย

CHULALONGKORN UNIVERSITY

Chapter 4
RESULTS AND DISCUSSION

The behavior of the PEC CO_2 RR is simulated using the physics model described in the previous section. Apart from isothermal and steady-state conditions, the simulation of time-dependent (transient) conditions was applied to compare the efficiencies of different PEC CO_2 RR systems. Many factors were identified to derive the excellent efficiency of PEC CO_2 RR for scaling up CO_2 RR in industrial production. Consequently, this study aims to evaluate some of the variables affecting PEC cells for CO_2 RR to derive the optimum performance.

4.1 Physics model validation

Prior simulation, the physics model should be validated to achieve the simulation of electrochemical CO_2 RR with high accuracy. The reducing discrepancy of the faradaic efficiency of $HCOO^-$ (FE_{HCOO^-}) between the experiment and physics model was performed by setting the controlled variables similarly. For example, cell configuration, operating temperature and pressure, pH of electrolytes, and the ratio of gas to liquid feeding (G/L). The accuracy of the physics model for electrochemical simulation was investigated following the correlation of FE and absolute cell voltage $|E_{cell}|$ curve. The FE_{HCOO^-} at various $|E_{cell}|$ between 1.5 V and 3.5 V, which were obtained from simulation of 2-dimensional MFC configuration, were compared with the experimental data reported in the literature under similar operating conditions as shown in figure 23
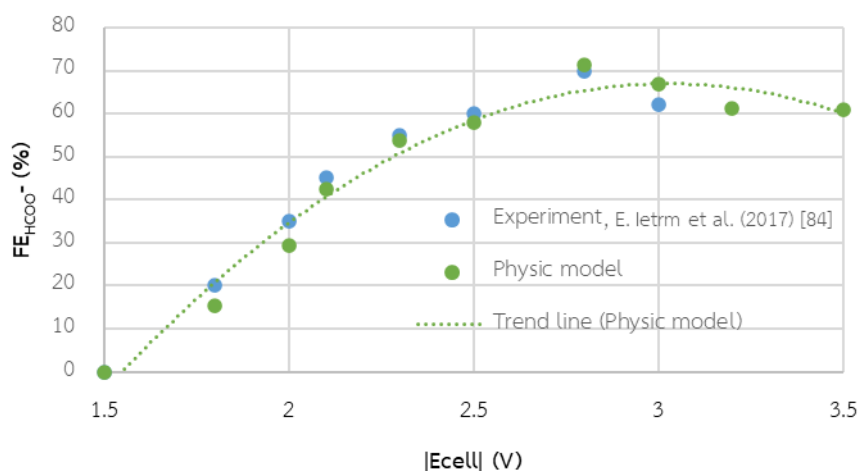
Figure 23. Comparison between the faradaic efficiencies of CO_2 RR to $HCOO^-$ (FE_{HCOO^-}) at various cell voltages, $|E_{cell}|$, between 1.5 V and 3.5 V as predicted from the physics model and experiment data reported in the literature, under similar operating conditions.

Validation of the physics model was actualized by comparing the results performance with the experimental data of I. E. Irem et al. [84], as shown in table 16. For MFC configuration, Sn based GDE cathode was used as a working-electrode operated under non-illuminated condition. The cause of fluctuation in product distribution of CO_2 RR depending on cell voltage can be described through the electrochemical process. When bias voltage applied on anode surface, the electrons would be excited across the energy band gap of the anodic semiconductor. It was found that the bottom of the conduction band (CB) and the top of the valence band (VB) would be possessed by electrons and holes, respectively. The recombination of electrons and holes could reveal on the anode. In contrast, the excited electrons would be transferred to react with CO_2 on the cathode surface while oxidized holes would provide OER on the anode surface when applied energy reached the equilibrium overpotentials.

Figure 23 shows the effect of cell voltage on product distribution of CO_2 RR which was presented by FE_{HCOO^-}. The electrochemical CO_2 reduction on the cathode

surface can be observed when the absolute applied cell voltages are higher than 1.5 V ($|E_{cell}| \geq 1.5$ V). The gradually increasing of FE_{HCOO^-} is observed when the low voltages (1.5V $\leq |E_{cell}| \leq$ 1.8V) were applied due to activation polarization. The overpotential when applying low voltages was derived from activation energy which is the minimum energy required for a chemical reaction. Consequently, the FE_{HCOO^-} disappears at the beginning of the activation polarization, in which activation overpotential was less than the equilibrium potential of CO_2 RR to $HCOO^-$. Then, the FE_{HCOO^-} is simultaneously increased to a maximum value when applied higher voltages (1.8V < $|E_{cell}| \leq$ 2.8V) because the energy for absorbed CO_2 reduction on the cathode to $HCOO^-$ was enough. However, the FE_{HCOO^-} is slightly decreased when the applied voltages become higher than the maximum point ($|E_{cell}|$ < 2.8V) because the overpotential for CO_2 RR is derived by CO_2 concentration on the cathode surface. The concentration overpotential is the potential gradient between the bulk (diffusion layer) and cathode surface which has different CO_2 concentrations between two positions. When CO_2 concentration on the cathode surface decreased, FE_{HCOO^-} would be decreased. In addition, the competition of HER would be increased when applied higher voltages.

It can also be seen that, the deviation of FE_{HCOO^-} from the physics model against experimental data shows a good agreement. The accuracy of the physic model in predicting the results was examined using the root mean square error (RMSE) which is equal to 3.36%. Therefore, validation of the physics model from COMSOL Multiphysics was confirmed for analysis of the variables affecting PEC cell for CO_2 RR to $HCOO^-$.

Regarding the activation and concentration polarizations, the ohmic polarization also affected the performance of PEC cell. The ohmic polarization is derived from the resistivity of the components such as ion-exchange membrane, electrolyte, and electrode effects on electric limitation. For this reason, the different

PEC cell configurations were simulated to define the optimum configuration in order to provide a proper environment for CO_2 RR to $HCOO^-$.

4.2 Arrangement of PEC cell configuration

To evaluate the effect of the arrangement of PEC cells on cell performance, different PEC cell configurations consisting of MFC, MEAFC, and MFC with a zero-gap anode were simulated under specific controlled variables. As the results of the physics model validation, the cathodic polarization of electrochemical CO_2 RR under dark conditions appeared when cell voltage was applied more than 1.5 V, ($|E_{cell}| > 1.5$ V). Then the illuminated simulation on TiO_2 photoanode was controlled under 1.5 V of boundary electric potential initial value, $\phi_{s,bnd,int}$ and 1.0 mA•cm^{-2} of photocurrent density. Formate ($HCOO^-$) is a liquid product from CO_2 RR which was concerned with the simulation of PEC cells for CO_2 RR.

จุฬาลงกรณ์มหาวิทยาลัย

CHULALONGKORN UNIVERSITY
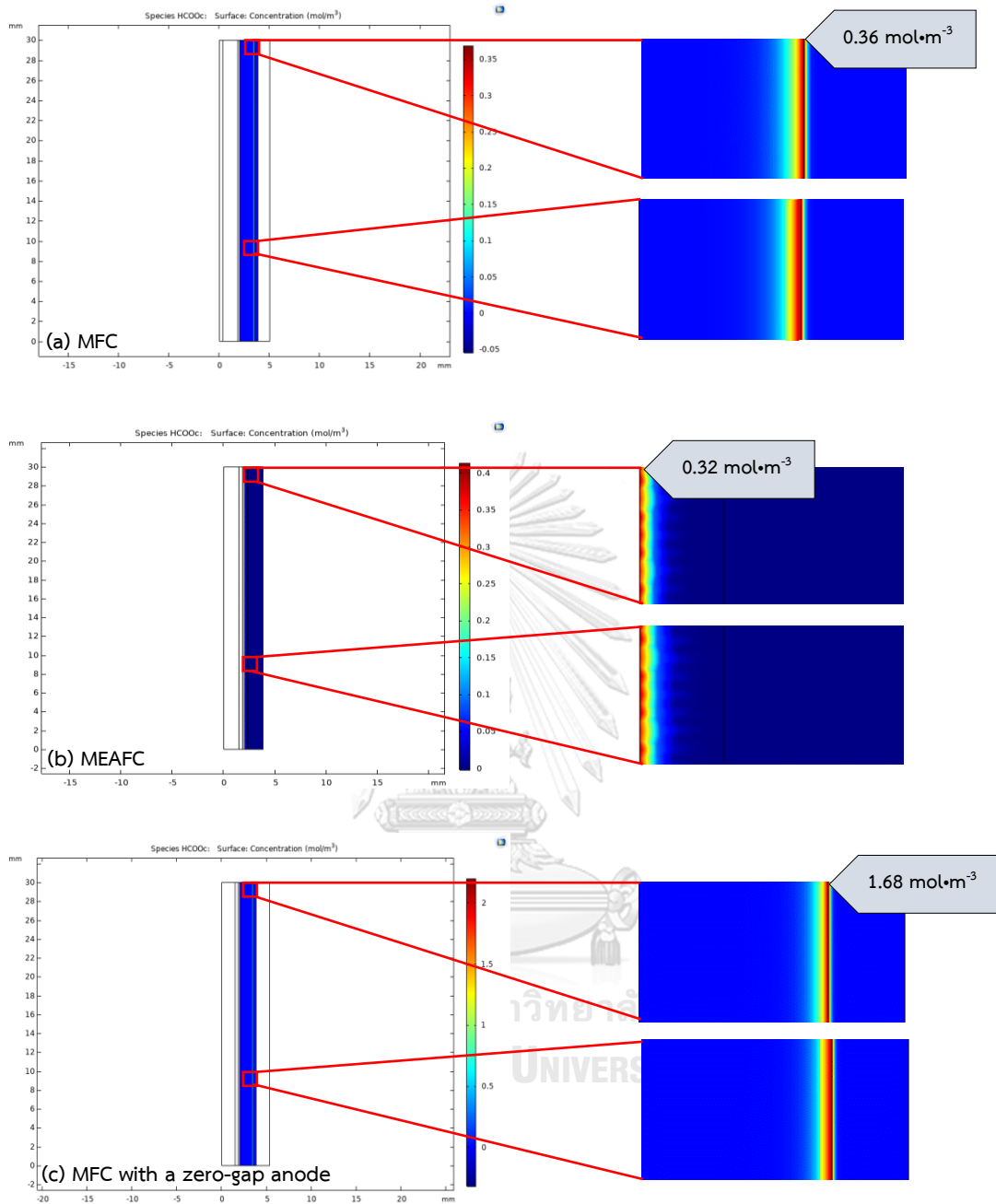
Figure 24. Concentration of HCOO$^-$ on the cathode surface of different PEC cell configurations including (a) MFC, (b) MEAFC, and (c) MFC with a zero-gap anode, with $\phi_{s,bnd,int}$ at 1.5 V and 1.0 mA•cm^{-2} photocurrent density on the TiO$_2$ photoanode.

The simulation of PEC CO_2 RR using COMSOL Multiphysics in this work mainly applied steady-state condition, while a few time-dependent simulations were required for comparison purposes.

From figure 24, the concentration gradient of $HCOO^-$, occurring on the interface between the catholyte channel and cathode GDE, was obtained from different configurations of PEC cells. The initial concentration of $HCOO^-$ appears on SnO_2-GDE and tends to decrease at the domain of electrolyte. The $HCOO^-$ is diminished because the attraction of negative ions and positive ions in an aqueous solution provides the production of HCOOH (formic acid) and HCOOK (potassium formate). Under similar controlled operating conditions, the outlet $HCOO^-$ concentrations on the interface between the catholyte channel and cathode GDE were 0.36 mol•m^{-3}, 0.32 mol•m^{-3}, and 1.68 mol•m^{-3} obtained from MFC, MEAFC, and MFC with a zero-gap anode, respectively.

The MFC, MEAFC, and MFC with a zero-gap anode were simulated and evaluated the performance through CO_2 conversion (X_{CO_2}), product selectivity (S), faradaic efficiency (FE%) and energy efficiency (EE%) as shown in figure 25 to 27, respectively.
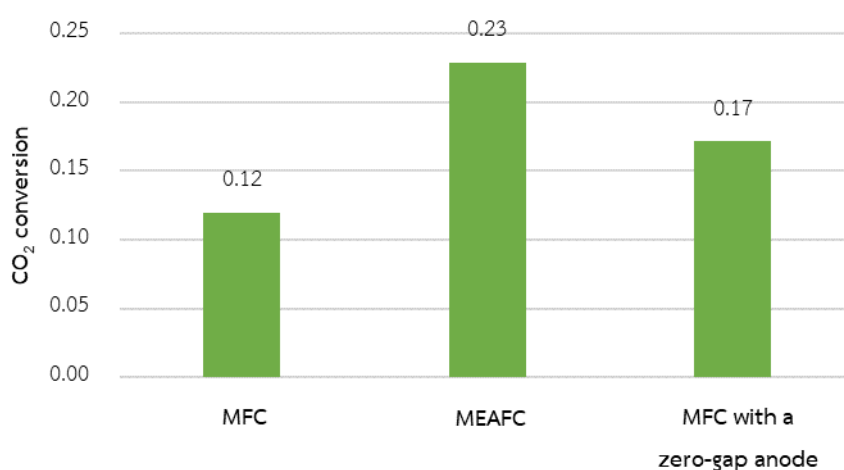
Figure 25. CO_2 conversion, X_{CO_2}, of different PEC cells configurations with applied $\phi_{s,bnd,int}$ at 1.5 V and 1.0 mA•cm^{-2} photocurrent density on the TiO_2 photoanode.

From figure 25, X_{CO_2} derived from direct gaseous CO_2 feeding should be higher than that of the dissolved CO_2 feeding because of the limitation of mass transfer. However, the highest 0.23 of X_{CO_2} was obtained from the MEAFC configuration because assumption of the saturated CO_2 in $KHCO_3$ solution could supply the maximum dissolved CO_2 under the condition at which the solution exists. Thus, the initial concentrations for saturated CO_2 in 0.5 M $KHCO_3$ were set to be in instant equilibrium. In contrast, the low value of X_{CO_2} derived from MFC and MFC with zero-gap anode configurations were calculated from simulation results of transportation of gaseous CO_2 through a porous media. Besides, the adding concentration of CO_2 for gas phase diffusion resulted in decreasing overall conversion. For this study, only a few seconds were simulated due to the limitation of memory requirement, thus, the residence time was too short to convert CO_2. The comparison of X_{CO_2} from different PEC cell configurations with different fed positions cannot be concluded. Therefore, the other indicators were presented to evaluate the cell performance.
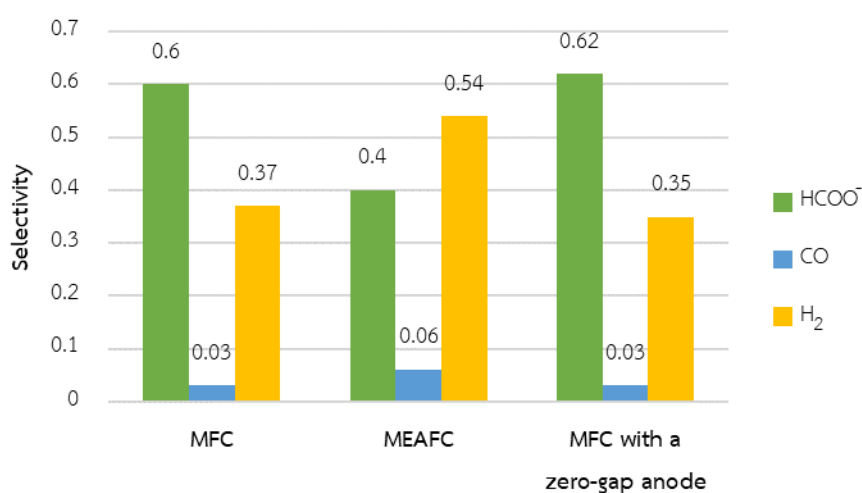
Figure 26. Product selectivity, *S*, obtained from different PEC cells configurations with $\phi_{s,bnd,int}$ at 1.5 V and 1.0 mA•cm^{-2} photocurrent density on the TiO$_2$ photoanode.

S_{HCOO^-} derived from the MFC and MFC with zero-gap anode configurations are higher than S_{HCOO^-} derived from the MEA configuration as shown in figure 26. The feeding of gaseous CO_2 could solve the limitation of mass transfer. Although X_{CO_2} derived from MEAFC configuration is high, the S_{HCOO^-} derived from MEAFC configuration is low due to the competition of other reduced species, especially 0.54 of S_{H_2} and 0.06 of S_{CO}. The 0.62 of S_{HCOO^-} derived from MFC with a zero-gap anode is higher than that of MFC due to low resistance between two electrodes, which causes enough overpotential for activating the electrochemical reactions.
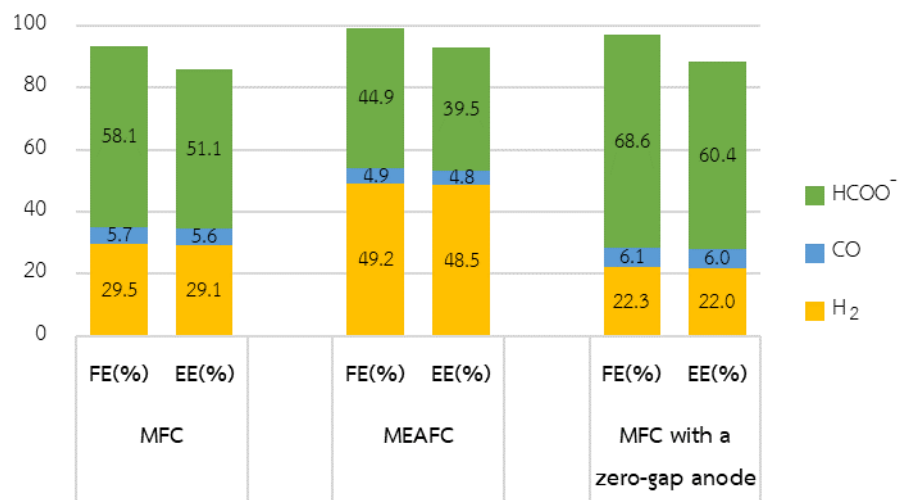
Figure 27. FE (%) and EE (%) of different PEC cells configurations with applied $\phi_{s,bnd,int}$ at 1.5 V and 1.0 mA•cm^{-2} photocurrent density on the TiO_2 photoanode.

From figure 27, the highest FE_{HCOO^-} of 68.6% was obtained from the MFC with zero-gap anode configuration because it was designed to overcome the limitation of mass transfer and ohmic overpotential loss by integrating half-cell of the MFC and MEAFC configurations. The half-cell of MFC configuration is applied on the cathodic compartment to increase CO_2 concentration, while the half-cell of the MEAFC configuration is applied on the anodic to reduce ohmic loss. The FE_{HCOO^-} of 58.1% and 44.9% obtained from the MFC and MEAFC are lower than that of the MFC with a zero-gap anode due to the fact that the ohmic polarization or potential drop

occurs as a result of product reduction performed from film covering on the cathode surface.

The EE_{HCOO^-} is the ratio of thermoneutral energy to applied energy of FE%, hence, EE% is directly proportional to FE%. The EE_{HCOO^-} of MFC, MEAFC, and MFC with a zero-gap anode were 51.1%, 39.5%, and 60.4%, respectively.

The PEC cell for CO_2 RR to $HCOO^-$ should provide high X_{CO_2}, and S_{HCOO^-} for saving capital costs as well as high FE_{HCOO^-} and EE_{HCOO^-} for saving operating cost. Under controlled similarly operating conditions, the MFC with a zero-gap anode configuration was chosen as a PEC cell simulation. Besides, other variables affecting cell performance were also studied to improve the performance of PEC cells.

4.3 Light intensity

To evaluate the effect of energy consumption on cell performance, light intensity (mW•cm^{-2}) was applied in a form of photocurrent density of 0.1, 0.5, 1.0, 5.0, 10.0, and 15.0 mA•cm^{-2} with specific boundary electric potential initial value. The MFC with a zero-gap anode was simulated at various current densities to evaluate the X_{CO_2}, S, FE%, and EE% as performance indicators.
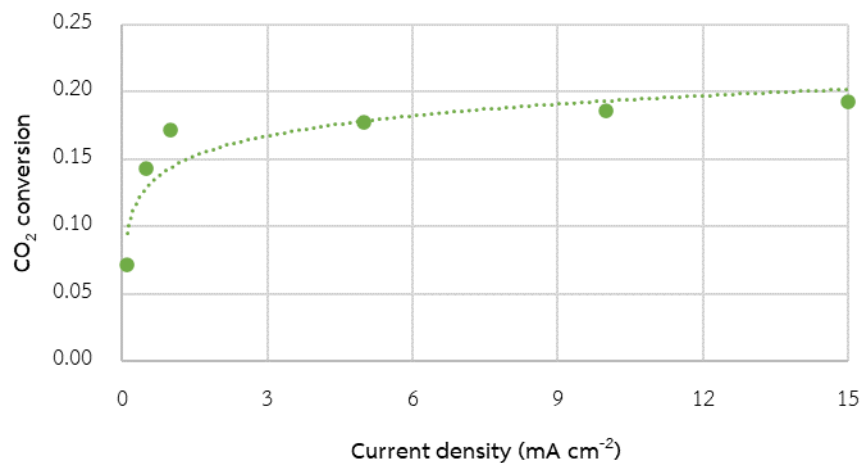
Figure 28. CO_2 conversion, X_{CO_2}, obtained at various applied current densities using MFC with a zero-gap anode with $\phi_{s,bnd,int}$ at 1.5 V on the TiO_2 photoanode.

The overpotential of the working cathode should be directly proportional to the amount of applied current density. The excited electrons derived from the activation of applied bias would be transferred to reduce CO_2 on the cathode surface. Then, a constant increase of X_{CO_2} was demonstrated when higher current densities were applied to TiO_2-photoanode as shown in figure 28. From the results, 0.19 of X_{CO_2} was achieved when 15 mA•cm^{-2} of current density was applied.
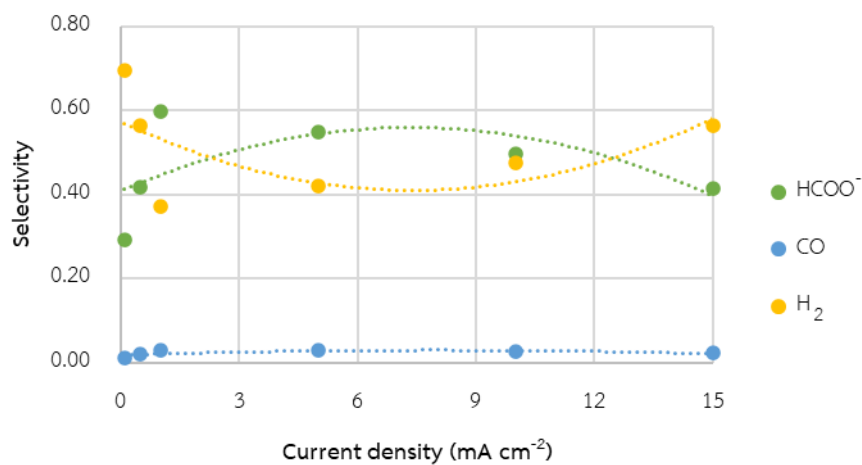
Figure 29. Product selectivity, S, obtained at various applied current densities using MFC with a zero-gap anode with $\phi_{s,bnd,int}$ at 1.5 V on the TiO_2 photoanode.

Figure 29 reveals the product distribution of CO_2 reduction at various applied current densities. When current densities were applied to TiO_2-photoanode enough to activate CO_2 RR, S_{HCOO^-} and S_{CO} increased dramatically to the highest value. In contrast, S_{H_2} decreased dramatically when CO_2 RR occurred. Then, the depletion of CO_2 on the cathode surface caused the competition of HER and decreasing CO_2 reduction. Therefore, the optimum applied current density required for CO_2 RR to achieve high S_{HCOO^-} was 0.6 when 1.0 mA•cm^{-2} of current density was applied.

The results given above can use to insist on the dependence of CO_2 concentration on the active interface (three-phase boundary) of reaction kinetics of CO_2 reduction, as described in mass-dependent equation of Butler-Volmer shown in Eq. (34) and (35). Besides, the reaction kinetics of HER were independent of CO_2

concentration, as described in mass-independent equation of Butler-Volmer shown in Eq. (36).

$$i_{HCOO^-} = i_{HCOO^-}^{ref} \frac{c_{CO_2}}{c_{CO_2,ref}} exp\left(-\frac{2\alpha_{HCOO^-}F}{RT}\eta_{HCOO^-}\right) \qquad \text{Eq. (34)}$$

$$i_{CO} = i_{CO}^{ref} \frac{c_{CO_2}}{c_{CO_2,ref}} exp\left(-\frac{2\alpha_{CO}F}{RT}\eta_{CO}\right) \qquad \text{Eq. (35)}$$

$$i_{H_2} = i_{H_2}^{ref} exp\left(-\frac{2\alpha_{H_2}F}{RT}\eta_{H_2}\right) \qquad \text{Eq. (36)}$$
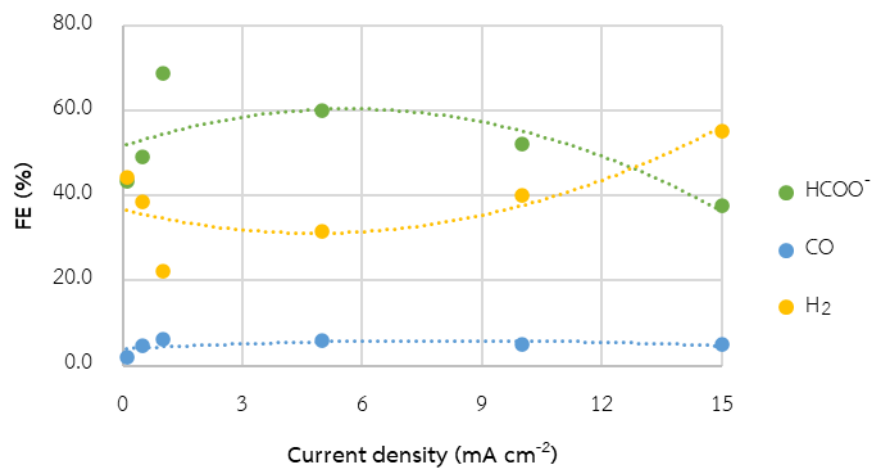
Figure 30. FE (%) obtained at various applied current densities using MFC with a zero-gap anode with applied $|E_{cell}|$ at 1.5 V on the TiO_2 photoanode
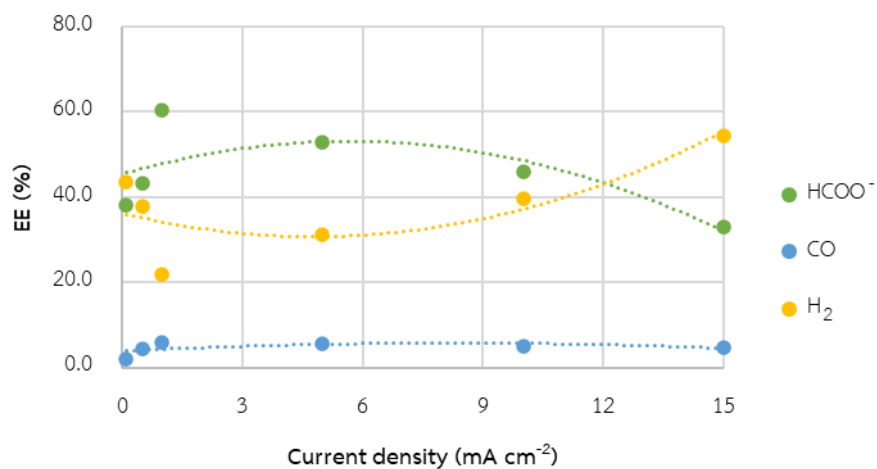
Figure 31. EE (%) obtained at various applied current densities using MFC with a zero-gap anode with applied $|E_{cell}|$ at 1.5 V on the TiO_2 photoanode.

The FE% can be derived from the amount of energy to drive electrochemical production. However, FE% of the product displays a similar trend as selectivity due to the electrons which are transferred to reduce CO_2 on the cathode being directly proportional to the applied current density. The EE% is constant with respect to FE% so the deviations of FE%, and EE% from applied various current densities show similar trends in figures 30 and 31. Therefore, when 1.0 mA•cm^{-2} of current density was applied, the highest values of 68.7% of FE_{HCOO^-} and 60.4% of EE_{HCOO^-} were obtained.

4.4 PEC cell length

To evaluate the effect of the surface area of PEC cell on cell performance, PEC cell lengths of 1.0, 1.5, 3.0, 4.0, 6.0, 8.0, and 10.0 cm were varied with specific controlled PEC cell height. The MFC with a zero-gap anode was simulated at various PEC cell lengths to evaluate the X_{CO_2}, S, FE%, and EE% as performance indicators.
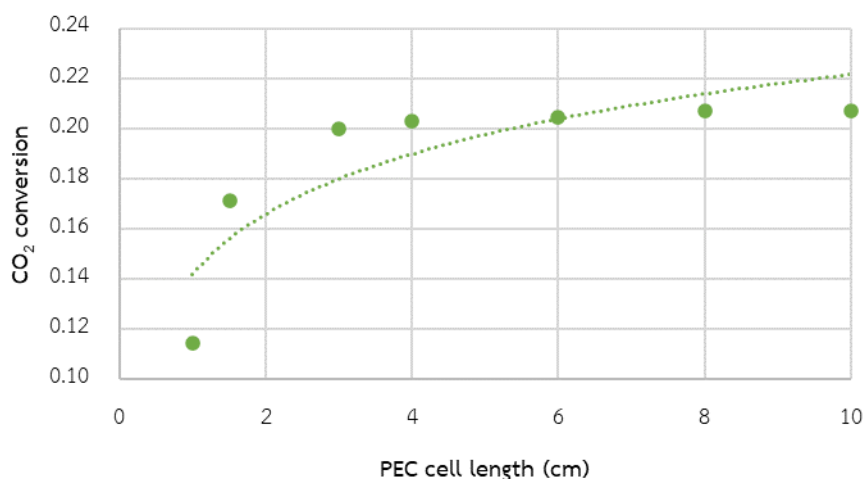
Figure 32. CO_2 conversion, X_{CO_2}, obtained at various PEC cell length using MFC with a zero-gap anode with $\phi_{s,bnd,int}$ at 1.5 V and 1.0 mA•cm^{-2} photocurrent density on the TiO_2 photoanode

From figure 32, the various cell lengths were simulated to observe the effect on X_{CO_2}. The results show that the increase X_{CO_2} ranged from 0.11 to 0.21 when the cell length was increased from 0.1 cm to 1.0 cm. The increasing cell length can

provide a larger surface area to absorb CO_2 on the electrode surface for electrochemical reactions.
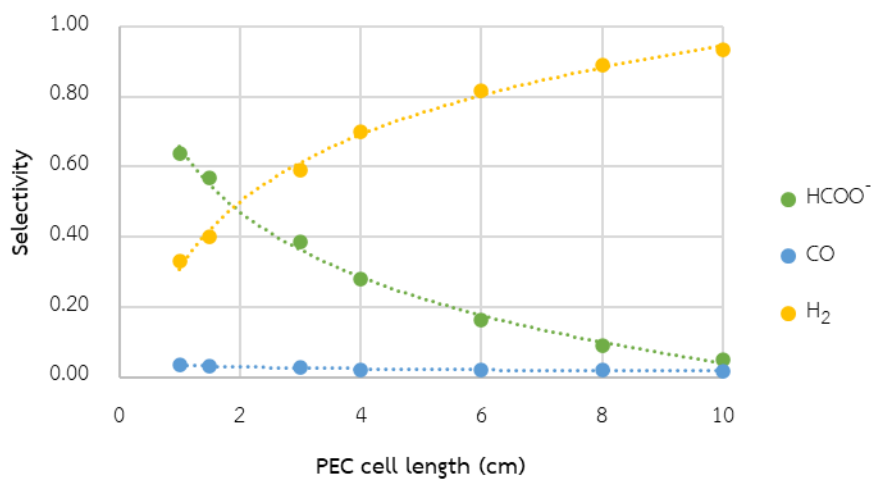
Figure 33. Product selectivity, *S*, obtained at various PEC cell length using MFC with a zero-gap anode with $\phi_{s,bnd,int}$ at 1.5 V and 1.0 mA•cm^{-2} photocurrent density on the TiO_2 photoanode.
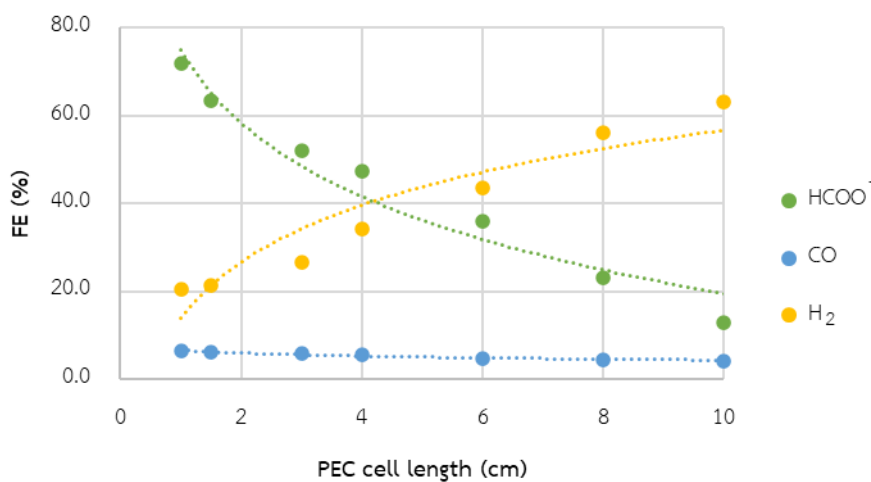
Figure 34. FE (%) obtained at various PEC cell length using MFC with a zero-gap anode with $\phi_{s,bnd,int}$ at 1.5 V and 1.0 mA•cm^{-2} photocurrent density on the TiO_2 photoanode.
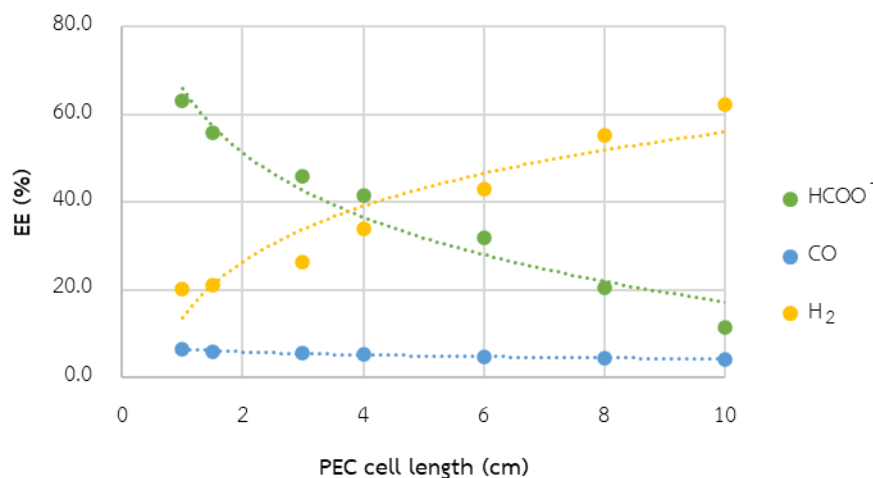
Figure 35. EE (%) obtained at various PEC cell length using MFC with a zero-gap anode with $\phi_{s,bnd,int}$ at 1.5 V and 1.0 mA•cm^{-2} photocurrent density on the TiO$_2$ photoanode.

However, the lack of average CO$_2$ concentration could occur when the longer PEC cell was used, resulting in continuous decreasing S_{HCOO^-}, FE$_{HCOO^-}$ and EE$_{HCOO^-}$ as shown in figures 33 to 35, respectively. Another problem is the increase of the HER which can produce H$_2$, regardless the concentration of ion species in the cell. Hence, diminished average CO$_2$ concentration and competition of HER would decrease the current density for HCOO$^-$ formation which is the cause of decreasing S_{HCOO^-}, FE$_{HCOO^-}$ and EE$_{HCOO^-}$.

According to above results, the minimum PEC cell length with acceptable X_{CO_2} is essential to define for PEC CO$_2$ RR simulation. The minimum PEC cell length for this study which still obtains high FE% and EE% for HCOO$^-$ production is required. At 1.5 cm of PEC cell length achieved 0.17 of X_{CO_2}, 0.57 of S_{HCOO^-}, 63.3% of FE$_{HCOO^-}$, and 55.7% of EE$_{HCOO^-}$.Thus, the other geometric variables of the PEC cell were studied to guide the scaling-up PEC cell for CO$_2$ conversion industry.

4.5 Gas channel width

      To evaluate the effect of geometric configuration of the PEC cell on cell performance, gas channel widths of 1.0, 1.5, 2.0, 3.0, 4.0, 5.0, 6.0, and 8.0 mm were varied with a specific controlled surface area of the PEC cell. The MFC with a zero-gap anode was simulated at various PEC cell lengths to evaluate X_{CO_2}, S, FE%, and EE% as performance indicators.
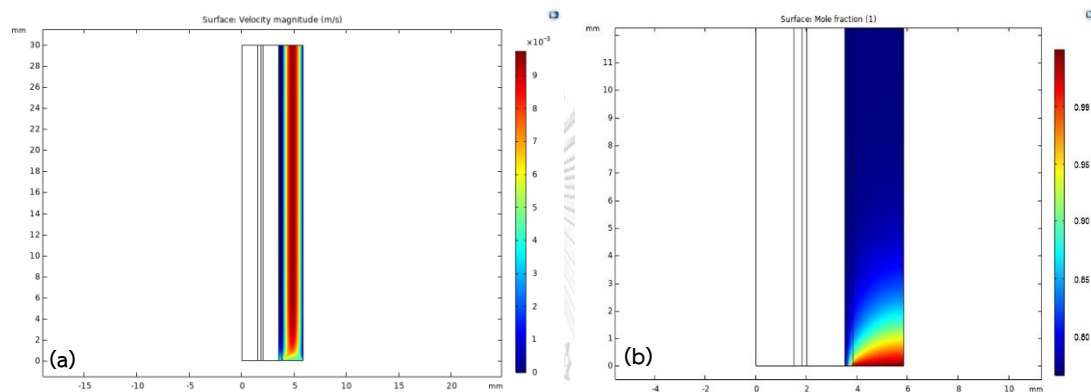
Figure 36. (a) The flow velocity and (b) mole fraction of CO_2 inside the gas channel with the width, W_g, of 2 mm, using MFC with a zero-gap anode with $\phi_{s,bnd,int}$ at 1.5 V and 1.0 mA•cm^{-2} photocurrent density on the TiO_2 photoanode.

      From figure 36(a), the outlet boundary of the gas channel was set as a fully developed laminar flow to sustain the continuous flow of gas in the channel. The mole fraction of CO_2 inside the gas channel can be used to evaluate the diffusion of CO_2 from the gas channel to the active site on the GDE, as shown in figure 36(b).
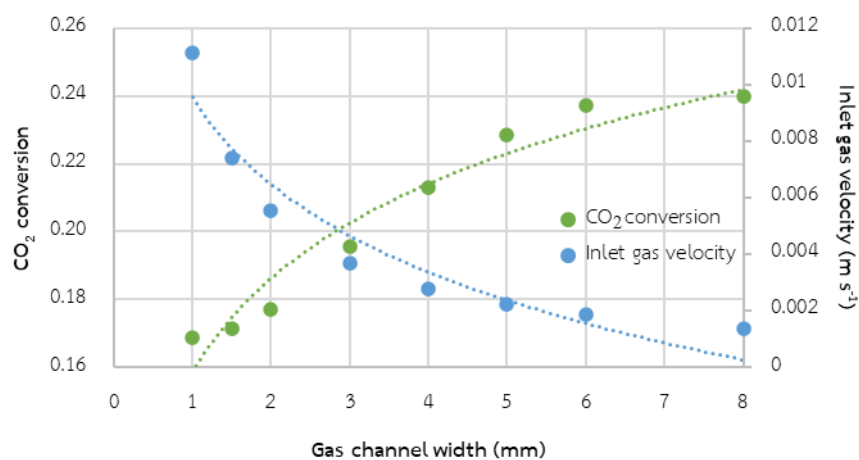
Figure 37. CO_2 conversion, X_{CO_2} and inlet gas velocity at various gas channel widths using MFC with a zero-gap anode with $\phi_{s,bnd,int}$ at 1.5 V and 1.0 mA•cm^{-2} photocurrent density on the TiO_2 photoanode.

Figure 37 presents the effect of variation of gas channel widths on the inlet gas velocity. When wider gas channels were simulated, the inlet gas velocity was lowered. The decreasing inlet gas velocity provided longer residence time for electrochemical reactions which resulted in an improvement of X_{CO_2}. For this reason, X_{CO_2} was increased when wider gas channel was simulated, as shown in figure 37. X_{CO_2} of 0.24 as obtained when 8 mm of gas channel width was used for simulation.
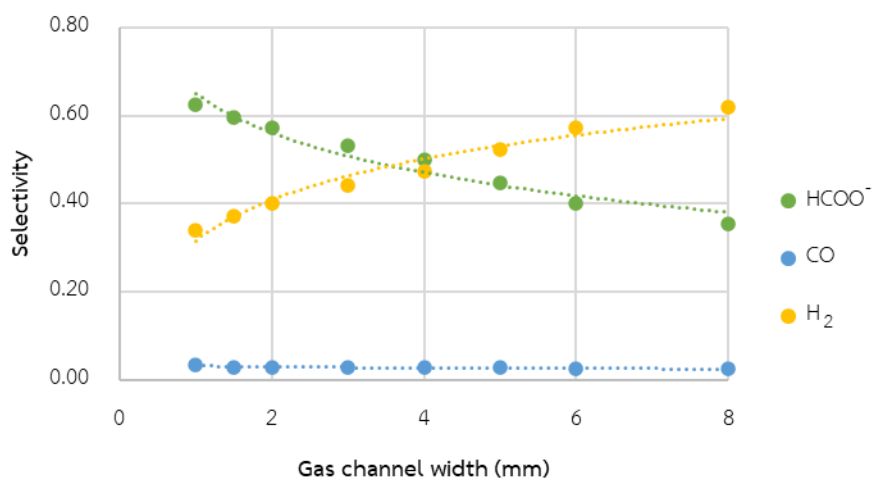
Figure 38. Product selectivity, *S*, obtained at various gas channel widths using MFC with a zero-gap anode with $\phi_{s,bnd,int}$ at 1.5 V and 1.0 mA•cm^{-2} photocurrent density on the TiO$_2$ photoanode.
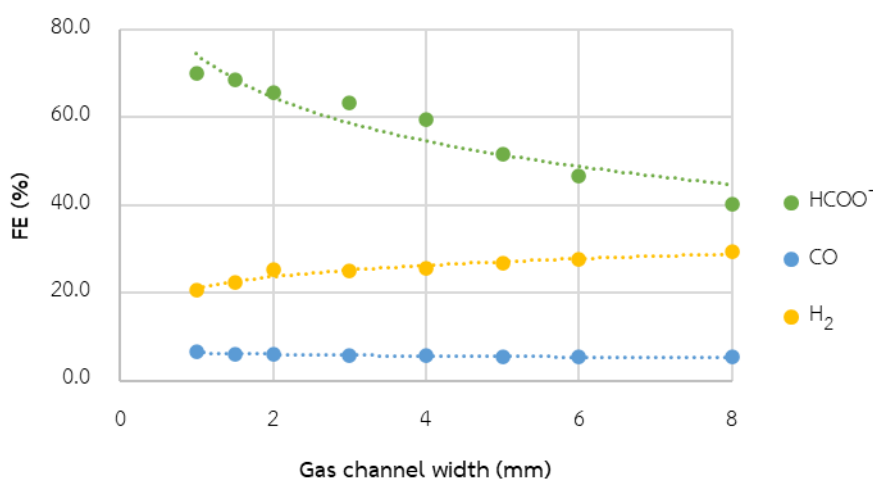
Figure 39. FE (%) obtained at various gas channel widths using MFC with a zero-gap anode with $\phi_{s,bnd,int}$ at 1.5 V and 1.0 mA•cm^{-2} photocurrent density on the TiO$_2$ photoanode.

Figure 40. EE (%) obtained at various gas channel widths using MFC with a zero-gap anode with $\phi_{s,bnd,int}$ at 1.5 V and 1.0 mA•cm^{-2} photocurrent density on the TiO$_2$ photoanode.

From figures 38 to 40, the high value of S_{HCOO^-}, FE$_{HCOO^-}$ and EE$_{HCOO^-}$ were obtained when a narrow gas channel was used for PEC CO$_2$ RR. When a narrow gas channel was used, faster inlet gas velocity appeared, which could enhance the CO$_2$ concentration on the active surface. Hence, the accumulation of CO$_2$ on the active area motivated the increase of current density and rate of reaction. In addition, S_{HCOO^-}, FE$_{HCOO^-}$ and EE$_{HCOO^-}$ tended to decrease when using the wider gas channel, which the diffusion and accumulation of CO$_2$ on the active area are low.

However, the reaction kinetics were independent of CO$_2$ concentration on the active interface when narrower gas channel was used, which provided very fast inlet gas velocity.

Consequently, the optimum gas channel width for this study is required to achieve high S_{HCOO^-}, FE$_{HCOO^-}$ and EE$_{HCOO^-}$ with acceptable X_{CO_2}. Using the gas channel width 1.5 mm achieved 0.17 of X_{CO_2}, 0.60 of S_{HCOO^-}, 68.7% of FE$_{HCOO^-}$, and 60.4% of EE$_{HCOO^-}$. Next, the effects of various electrolyte channel widths were analyzed on PEC cell performance.

4.6 Electrolyte channel width

To evaluate the effect of the geometric configuration of the PEC cell on cell performance, electrolyte channel widths of 1.0, 1.5, 2.0, 2.5, 3.0, 4.0, 6.0, and 8.0 mm were varied with a specific controlled surface area of the PEC cell. The MFC with a zero-gap anode was simulated at various electrolyte channel widths to evaluate X_{CO_2}, S, FE%, and EE% as performance indicators.
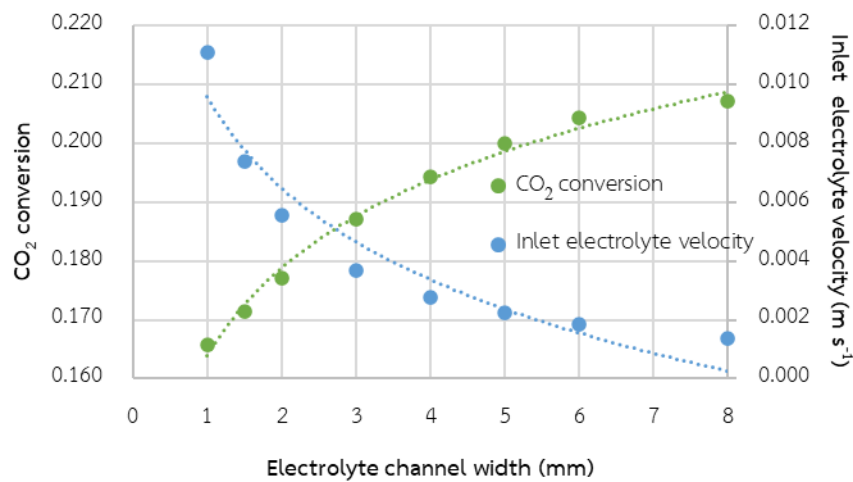

Figure 41. CO_2 conversion, X_{CO_2}, and inlet electrolyte velocity at various electrolyte channel widths using MFC with a zero-gap anode with $\phi_{s,bnd,int}$ at 1.5 V and 1.0 mA•cm^{-2} photocurrent density on the TiO_2 photoanode.

Figure 41 presents the variation of electrolyte channel width effects on the inlet electrolyte velocity. When wider electrolyte channels were simulated, the inlet electrolyte velocity was lowered. Decreasing inlet electrolyte velocity provided longer residence time for electrochemical reactions which resulted in improvement of X_{CO_2}. For this reason, X_{CO_2} was increased when wider electrolyte channel was simulated, as shown in figure 41. X_{CO_2} of 0.21 was obtained when 8.0 mm of electrolyte channel width was used for simulation.
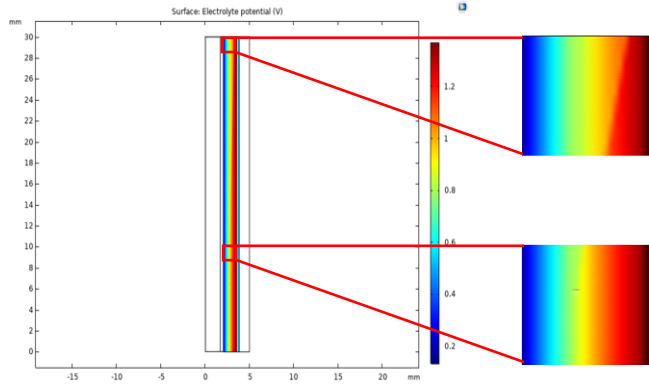
Figure 42. Electrolyte potential inside catholyte channel with the width, W_l, of 2 mm, using MFC with a zero-gap anode with $\phi_{s,bnd,int}$ at 1.5 V and 1.0 mA•cm^{-2} photocurrent density on the TiO$_2$ photoanode.

The rate of electrochemical reaction is given by Eq. (40) derived from the local current density and overpotential which are described in the Butler-Volmer equation as following Eq. (33) and (39).

$$i_i = k_i \left[c_R \, exp\left(\frac{\alpha_a F\eta}{RT}\right) - c_O \, exp\left(\frac{-\alpha_c F\eta}{RT}\right) \right] \qquad \text{Eq. (33)}$$

$$\eta = \phi_s - \phi_l - \phi_0 \qquad \text{Eq. (39)}$$

$$R_i = \frac{v_i i_i}{n_{i,e} \, F} \qquad \text{Eq. (40)}$$

From figure 42, the electrolyte potential (ϕ_l) inside the catholyte channel decreased along the cell length which was in line with the rate of reaction according to the rate of the electrochemical reactions and are described as a function of the overpotential (η).

In addition, charge transport which is described in the Nernst-Planck's equation resulted from the diffusion, migration, and convection of ionic species as shown in Eq. (22) and (23). Therefore, the electrolyte width that affects the rate of ionic diffusion also affects the rate of electrochemical reactions.

$$\nabla \cdot n_i = R_i \qquad \text{Eq. (22)}$$

$$n_i = -D_i \nabla c_i - z_i u_{mi} F c_i \nabla \phi_{l,e} + u c_i \qquad \text{Eq. (23)}$$
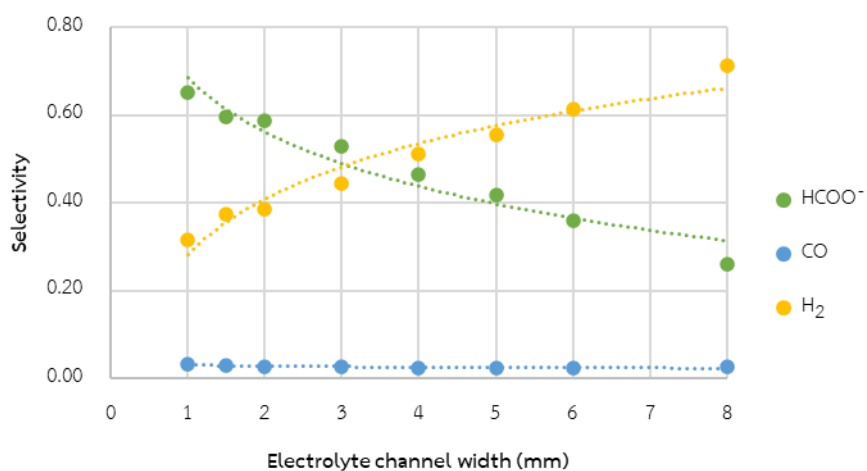
Figure 43. Product selectivity, *S*, obtained at various electrolyte channel widths using MFC with a zero-gap anode with $\phi_{s,bnd,int}$ at 1.5 V and 1.0 mA•cm^{-2} photocurrent density on the TiO$_2$ photoanode.
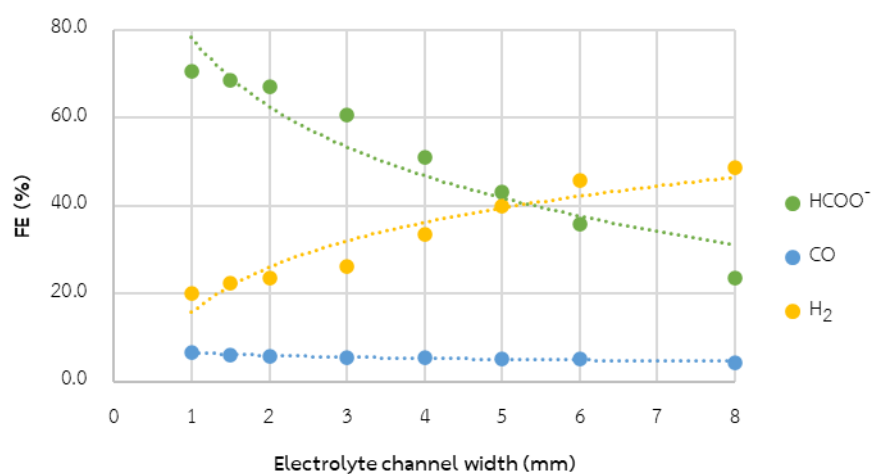
Figure 44. FE (%) obtained at various electrolyte channel widths using MFC with a zero-gap anode with $\phi_{s,bnd,int}$ at 1.5 V and v photocurrent density on the TiO$_2$ photoanode.
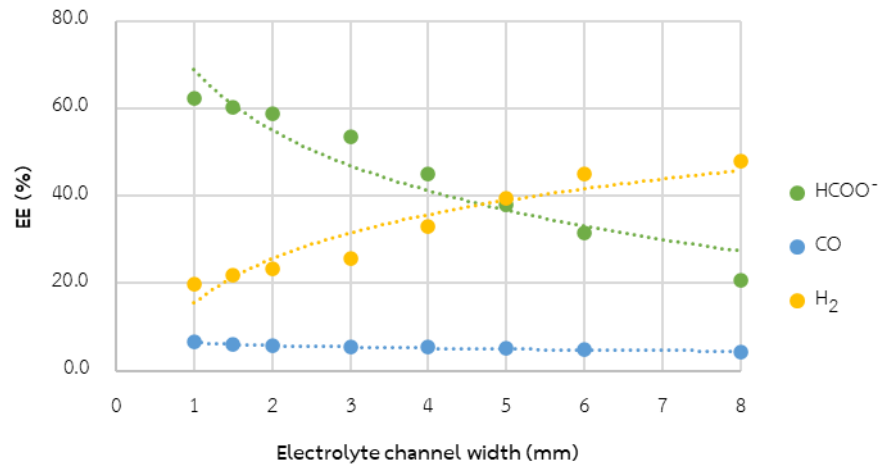
Figure 45. EE (%) obtained at various electrolyte channel widths using MFC with a zero-gap anode with $\phi_{s,bnd,int}$ at 1.5 V and 1.0 mA•cm^{-2} photocurrent density on the TiO$_2$ photoanode.
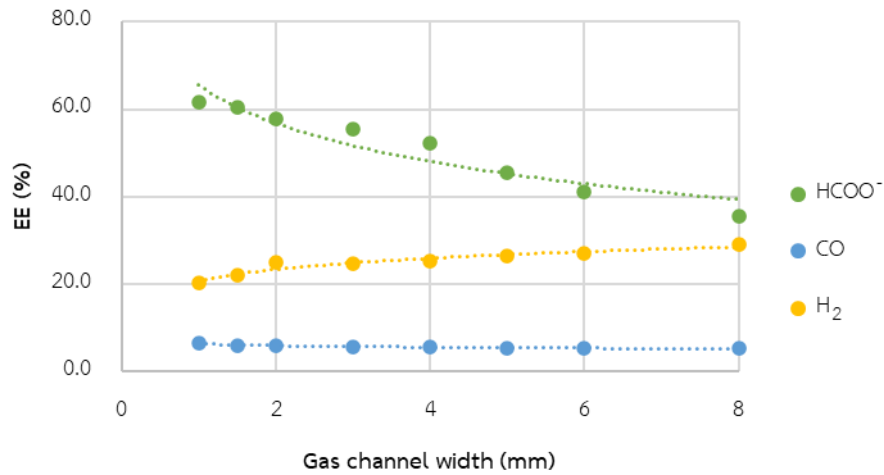
From figures 43 to 45, the high values of S_{HCOO^-}, FE$_{HCOO^-}$ and EE$_{HCOO^-}$ were obtained when a narrow electrolyte channel was used for PEC CO$_2$ RR. When narrow electrolyte channel was used, faster transport of ionic species appeared which could enhance the rate of electrochemical reaction. The average CO$_2$ concentration also motivated the increase of partial current density and rate of electrochemical reactions. However, S_{HCOO^-}, FE$_{HCOO^-}$ and EE$_{HCOO^-}$ tended to decrease when using wider electrolyte channel. Therefore, the H$_2$ competition increased when using wider electrolyte channel which provided lower transport of ionic species. These results can be concluded that the ohmic loss increased when wider electrolyte channel was used.

Consequently, the maximum electrolyte channel width for this study is required to achieve high S_{HCOO^-}, FE$_{HCOO^-}$ and EE$_{HCOO^-}$ with acceptable X_{CO_2}. Using electrolyte channel width of 2.0 mm achieved 0.18 of X_{CO_2}, 0.59 of S_{HCOO^-}, 67.0% of FE$_{HCOO^-}$, and 59.0% of EE$_{HCOO^-}$.

According to the simulation results of PEC cell, it is evident that the arrangement and geometric design of cell components play important roles in the

cell performance. The reasons for performance variation are derived from the overpotential of activation energy, CO_2 concentration on the active site, and resistivity of each component. Thus, the optimum geometric design of a specific system should be concerned to achieve the maximum performance of the PEC cell.

จุฬาลงกรณ์มหาวิทยาลัย
CHULALONGKORN UNIVERSITY

Chapter 5

CONCLUSIONS

5.1 Conclusions

In this study, a simulation of CO_2 utilization was performed through a 2-dimensional PEC cell applying the physics model in COMSOL Multiphysics. The numerical analysis from COMSOL Multiphysics assembled physics models which included tertiary current distribution (TCD), secondary current distribution (SCD), laminar flow, and transport of concentrated species in porous media described the behavior of the PEC process for CO_2 RR to CO and $HCOO^-$.

Besides, the aim is to evaluate the affecting variables of PEC cells through physics model simulation; thus, a steady-state and a few time-dependent conditions were simulated. After the simulation of specific systems, it was found that the results of the present study can be concluded as follows:

1. MEAFC configuration provides the value of X_{CO_2} higher than that of MFC and MFC with zero-gap anode configurations because the MEAFC feeding is a reactant in form of saturated CO_2 in 0.5 M $KHCO_3$ while adding a concentration of gaseous CO_2 of MFC and MFC with a zero-gap anode can decrease overall conversion.

2. The MFC with a zero-gap anode configuration which is designed to overcome the mass transfer limitation of MEAFC configuration and ohmic loss polarization of MFC configuration. Therefore, this design configuration provides high values of the product selectivity, FE, and EE of CO_2 RR.

3. Applied current density not only directly affects X_{CO_2} but also directly affects product selectivity, FE, and EE of CO_2 RR of the activation of applied bias would excite electrons to reduce CO_2 on the cathode surface. However, the excess applied current densities cause product selectivity, FE, and EE of CO_2 RR tended to decrease due to the competition of HER.

4. 4.The optimum PEC cell length should be concerned, although longer cells can provide the increase in X_{CO_2} from a larger surface area for electrochemical reactions. In contrast, when the PEC cell length is too long, it can cause a diminished average CO_2 concentration in the cell which results in continuously decreasing product selectivity, FE, and EE of CO_2 RR.

5. Similarly, the optimum width of the fluid channels should be concerned. The wider fluid channels can improve X_{CO_2} from a longer residence time for electrochemical reactions. Regarding the product selectivity, FE, and EE of CO_2 RR tends to decrease when using wider fluid channels since the loss of ohmic from the product accumulation on the electrode surface.

5.2 Recommendations for the future work

1. Investigate the effect of the pH of electrolyte solution to estimate the optimal electrochemical environment for CO_2 RR to CO and $HCOO^-$.

2. Investigate and simulate another type of ion-exchange membrane for the PEC cell model, such as an anion exchange membrane (AEM) and bipolar exchange membrane, to determine the best performance of PEC cell for CO_2 RR to CO and $HCOO^-$.

APPENDIX

Appendix A: Calculation of diffusion coefficient of multicomponent

The diffusion coefficient of the multicomponent can be determined using the correlation of Fuller, Schettler, and Giddings, as shown in Eq (13) [69].

$$D_{ij} = \frac{10^{-3}T^{1.75}\left(\frac{1}{M_i} + \frac{1}{M_j}\right)^{1/2}}{p\left(v_i^{1/3} + v_j^{1/3}\right)}$$

Eq. (13)

where D_{ij} is multicomponent diffusion coefficient (cm^2•s^{-1})

T is temperature (K)

p is the pressure (atm)

v_i is the diffusion volume for molecule i

M_i is molecular weight of gas i (g•mol^{-1})

Table 14. The diffusion volume for molecule i

Parameters of gas i	Symbol	Value	Unit	Ref.
Molecular weight of CO$_2$	M_{CO_2}	44.01	g•mol^{-1}	[102]
Molecular weight of CO	M_{CO}	28.01	g•mol^{-1}	
Molecular weight of H$_2$	M_{H_2}	2.02	g•mol^{-1}	
Molecular weight of N$_2$	M_{N_2}	28.01	g•mol^{-1}	
Molecular weight of O$_2$	M_{O_2}	32.00	g•mol^{-1}	
Molecular weight of H$_2$O	M_{H_2O}	18.02	g•mol^{-1}	
Diffusion volume of CO$_2$	v_{CO_2}	26.9	cm^3•mol^{-1}	[69]
Diffusion volume of CO	v_{CO}	18.9	cm^3•mol^{-1}	
Diffusion volume of H$_2$	v_{H_2}	6.12	cm^3•mol^{-1}	
Diffusion volume of N$_2$	v_{N_2}	17.9	cm^3•mol^{-1}	
Diffusion volume of O$_2$	v_{O_2}	16.6	cm^3•mol^{-1}	
Diffusion volume of H$_2$O	v_{H_2O}	12.7	cm^3•mol^{-1}	

The multicomponent diffusion coefficients, D_{ij} are defined as using Eq. (13).

$$D_{CO_2CO} = \frac{10^{-3}(298.15^{1.75})\left(\frac{1}{44.01} + \frac{1}{28.01}\right)^{1/2}}{\left(26.9^{1/3}+18.9^{1/3}\right)} = 9.14 \times 10^{-5} \text{ m}^2\text{•s}^{-1}$$

$$D_{CO_2H_2} = \frac{10^{-3}(298.15^{1.75})\left(\frac{1}{44.01} + \frac{1}{2.02}\right)^{1/2}}{\left(26.9^{1/3}+6.12^{1/3}\right)} = 3.20 \times 10^{-4} \text{ m}^2\text{•s}^{-1}$$

$$D_{CO_2N_2} = \frac{10^{-3}(298.15^{1.75})\left(\frac{1}{44.01} + \frac{1}{28.01}\right)^{1/2}}{\left(26.9^{1/3}+17.9^{1/3}\right)} = 9.21 \times 10^{-5} \text{ m}^2\text{•s}^{-1}$$

$$D_{CO_2O_2} = \frac{10^{-3}(298.15^{1.75})\left(\frac{1}{44.01} + \frac{1}{32.00}\right)^{1/2}}{\left(26.9^{1/3}+16.6^{1/3}\right)} = 1.12 \times 10^{-4} \text{ m}^2\text{•s}^{-1}$$

$$D_{CO_2H_2O} = \frac{10^{-3}(298.15^{1.75})\left(\frac{1}{44.01} + \frac{1}{18.02}\right)^{1/2}}{\left(26.9^{1/3}+12.7^{1/3}\right)} = 8.96 \times 10^{-5} \text{ m}^2\text{•s}^{-1}$$

$$D_{COH_2} = \frac{10^{-3}(298.15^{1.75})\left(\frac{1}{28.01} + \frac{1}{2.02}\right)^{1/2}}{\left(18.9^{1/3}+6.12^{1/3}\right)} = 3.47 \times 10^{-4} \text{ m}^2\text{•s}^{-1}$$

$$D_{CON_2} = \frac{10^{-3}(298.15^{1.75})\left(\frac{1}{28.01} + \frac{1}{28.01}\right)^{1/2}}{\left(18.9^{1/3}+17.9^{1/3}\right)} = 1.08 \times 10^{-4} \text{ m}^2\text{•s}^{-1}$$

$$D_{COO_2} = \frac{10^{-3}(298.15^{1.75})\left(\frac{1}{28.01} + \frac{1}{32.00}\right)^{1/2}}{\left(18.9^{1/3}+16.6^{1/3}\right)} = 1.06 \times 10^{-4} \text{ m}^2\text{•s}^{-1}$$

$$D_{COH_2O} = \frac{10^{-3}(298.15^{1.75})\left(\frac{1}{28.01} + \frac{1}{18.02}\right)^{1/2}}{\left(18.9^{1/3}+12.7^{1/3}\right)} = 1.29 \times 10^{-4} \text{ m}^2\text{•s}^{-1}$$

$$D_{N_2H_2} = \frac{10^{-3}(298.15^{1.75})\left(\frac{1}{28.01} + \frac{1}{2.02}\right)^{1/2}}{\left(17.9^{1/3}+6.12^{1/3}\right)} = 3.51 \times 10^{-4} \text{ m}^2\text{•s}^{-1}$$

$$D_{N_2O_2} = \frac{10^{-3}(298.15^{1.75})\left(\frac{1}{28.01} \frac{1}{32.00}\right)^{1/2}}{\left(17.9^{1/3}+16.6^{1/3}\right)} = 1.07 \times 10^{-4} \text{ m}^2\text{•s}^{-1}$$

$$D_{N_2H_2O} = \frac{10^{-3}(298.15^{1.75})\left(\frac{1}{28.01} + \frac{1}{18.02}\right)^{1/2}}{\left(17.9^{1/3}+12.7^{1/3}\right)} = 3.82 \times 10^{-4} \text{ m}^2\text{•s}^{-1}$$

$$D_{H_2H_2O} = \frac{10^{-3}(298.15^{1.75})\left(\frac{1}{2.02} + \frac{1}{18.02}\right)^{1/2}}{\left(6.12^{1/3}+12.7^{1/3}\right)} = 3.82 \times 10^{-4} \text{ m}^2\text{•s}^{-1}$$

$$D_{O_2H_2O} = \frac{10^{-3}(298.15^{1.75})\left(\frac{1}{32.00}+\frac{1}{18.02}\right)^{1/2}}{\left(16.6^{1/3}+12.7^{1/3}\right)} = 1.29 \times 10^{-4} \text{ m}^2\cdot\text{s}^{-1}$$

Appendix B: Calculation of permeability of GDE

The permeability of GDE is the average permeability of a porous medium consisting of a catalyst layer (CL) and a diffusion layer (GDL). The predicted model of Tomadakis-Sotirchos is used to identify the permeability of GDE as following Eq. (41) [69].

$$K = \frac{\varepsilon}{8ln^2\varepsilon} \frac{(\varepsilon-\varepsilon_p)^{\alpha+2}\, r_f^2}{(1-\varepsilon_p)^{\alpha}[(\alpha+1)(\varepsilon-\varepsilon_p)]^2} \qquad \text{Eq. (41)}$$

where K is the average permeability of the porous medium

ε is the average porosity

ε_p is the percolation threshold porosity (ε_p = 0.11)

α Is the fitting parameter for trough-plan diffusion (α = 0.785)

r_f is the carbon fiber radius (r_f = 4.6 × 10^{-6} m)

Besides, the average porosity of GDE can be defined following Eq. (42).

$$\varepsilon = \frac{\varepsilon_{cl}+\varepsilon_{gdl}}{2} \qquad \text{Eq. (42)}$$

where ε_{cl} is the porosity of catalyst layer (ε_{cl} = 0.4)

ε_{gdl} is the porosity of gas diffusion layer (ε_{gdl} = 0.663)

Therefore, the parameter values are substituted to specify the average permeability of the porous medium as follows.

$$\varepsilon = \frac{0.4+0.663}{2} = 0.5315$$

$$K = \frac{0.5315}{8ln^2(0.5315)} \frac{(0.5315-0.11)^{0.785+2}\,(4.6 \times 10^{-6} \text{ m})^2}{(1-0.11)^{0.785}[(1-0.11)\,(0.5315-0.11)]^2}$$

$$K = 2.47 \times 10^{-12} \text{ m}^2$$

Appendix C: Calculation of fluid velocity

The flow regime of fluid is assumed to be laminar flow which depends on the range of Reynold's number (Re). The correlation between the inlet of fluid velocity and Re is identified as following Eq. (21).

$$u = \frac{\mu Re}{\rho L}$$

<div align="right">Eq. (21)</div>

where u is fluid velocity (m•s^{-1})

μ is dynamic fluid viscosity (kg•m^{-1}•s^{-1})

Re is Reynold numbers (Re<2000)

L is characteristic length (m)

ρ is fluid density (kg•m^{-3})

However, the characteristic length, L replies to the geometry of reactors. The fluid flow channels of the 2-dimensional model of PEC are designed to be rectangular ducts so L can be defined from the hydraulic diameter, D_h as Eq. (43).

$$D_h = \frac{4ab}{2(a+b)} = \frac{2ab}{a+b}$$

<div align="right">Eq. (43)</div>

where a is channel width and is b channel height (m)

For electrolyte channels, the hydraulic diameter, D_h defined as:
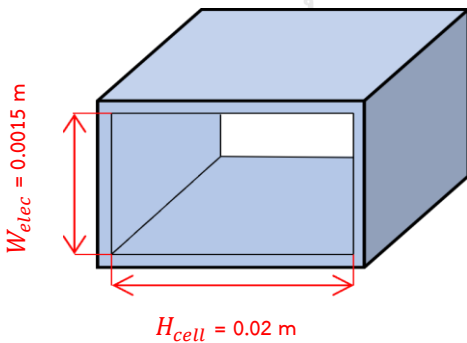
$$D_{h,elec} = \frac{2(0.0015 \text{ m} \times 0.015 \text{ m})}{0.0015 \text{ m} + 0.015 \text{ m}} = 0.0027 \text{ m}$$

The inlet of electrolyte velocity when Re < 2000:

$$u_{elec} = \frac{\mu_l Re}{\rho_l D_{h,elec}}$$

<div align="right">Eq. (44)</div>

$$u_{elec} = \frac{(1.07 \times 10^{-3} \text{ kg·m}^{-1}\text{s}^{-1})(2000)}{(1030 \text{ kg·m}^{-3})(0.0027 \text{ m})} = 0.8 \text{ m·s}^{-1}$$

Also, the inlet of electrolyte velocity, u_{elec} is set to less than 0.8 m·s^{-1} to control the laminar flow regime of the electrolyte.

For gas channel, the hydraulic diameter, D_h defined as:
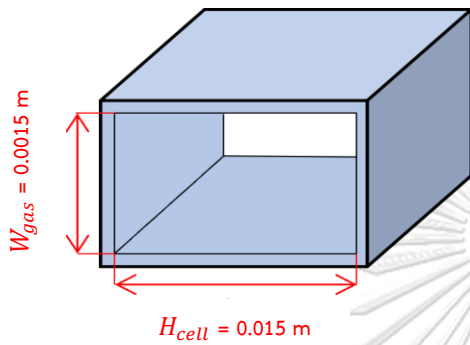
$$D_{h,gas} = \frac{2(0.0015 \text{ m} \times 0.015 \text{ m})}{0.0015 \text{ m} + 0.015 \text{ m}} = 0.0027 \text{ m}$$

The inlet of gas velocity when $Re < 2000$:

$$u_{gas} = \frac{\mu_g Re}{\rho_g D_{h,gas}} \qquad \text{Eq. (45)}$$

$$u_{gas} = \frac{(1.665 \times 10^{-5} \text{ kg·m}^{-1}\text{s}^{-1})(2000)}{(1.410 \text{ kg·m}^{-3})(0.0027 \text{ m})} = 8.7 \text{ m·s}^{-1}$$

Also, the inlet of electrolyte velocity, u_{gas} is set to less than 8.7 m·s^{-1} to control the laminar flow regime of the electrolyte.

Appendix D: Calculation initial concentration of dissolved species

In order to simulate the electrochemical reduction reaction of CO_2 to desired products at the interface of electrolyte/electrode, initial concentrations of dissolved species are required. The solubility of gaseous CO_2 in the aqueous electrolyte solution are necessary to study because concentration of salt of electrolyte can affect to mass transfer in CO_2 RR. The solubility of CO_2 in salt solution can apply the Schump relation which describes effect of moderate to high salt concentration on gas solubility as Eq. (46).

$$\log\left(\frac{c_{G,0}}{c_G}\right) = \sum(h_i + h_G)c_i \qquad \text{Eq. (46)}$$

where $c_{G,0}$ is the concentration dissolved gas in pure water

($c_{G,0}$ at 298 K is 33.95 mol•m^{-3})

c_G is the concentration dissolved gas in salt solution (mol•m^{-3})

c_i is the concentration of ion or dissolved species

(c_i of 0.5 M $KHCO_3$ is 500 mol•m^{-3})

h_i is the ion specific parameter (m^3•mol^{-1})

h_G is the gas specific parameter (m^3•mol^{-1})

The specific parameters of gas (h_G) depends on temperature, therefore, h_G can be defined by following Eq. (47).

$$h_G = h_{G,0} + h_T(T-298.15 \text{ K}) \qquad \text{Eq. (47)}$$

where $h_{G,0}$ is the gas specific parameter at reference temperature (m^3•mol^{-1})

h_T is the gas specific parameter for the temperature effect (m^3•mol^{-1}•K^{-1})

T is temperature (K)

Table 15. The specific parameters for calculation of the solubility of gases in aqueous electrolyte [44].

Parameters	Dissolved species	Value	Unit
$h_{G,0}$	CO_2	-1.83×10^{-5}	$m^3 \cdot mol^{-1}$
h_T at 273-313 K		-3.38×10^{-7}	$m^3 \cdot mol^{-1} \cdot K^{-1}$
h_i	CO_3^{2-}	14.23×10^{-4}	$m^3 \cdot mol^{-1}$
	HCO_3^-	13.72×10^{-5}	$m^3 \cdot mol^{-1}$
	H^+	0.00	$m^3 \cdot mol^{-1}$
	OH^-	8.39×10^{-5}	$m^3 \cdot mol^{-1}$
	K^+	9.59×10^{-5}	$m^3 \cdot mol^{-1}$

For this system, the solubility of CO_2 at 298.15 K in 0.5 M $KHCO_3$:

$$h_G = -1.83 \times 10^{-5} - 3.38 \times 10^{-7}(298.15 - 298.15) = -1.83 \times 10^{-5} \ m^3 \cdot mol^{-1}$$

$$\log\left(\frac{c_{G,0}}{c_G}\right) = (500 \ mol \cdot m^{-3})(13.72 \times 10^{-5} - 1.83 \times 10^{-5} \ m^3 \cdot mol^{-1}) \qquad (HCO_3^{1-})$$

$$+ (500 \ mol \cdot m^{-3})(9.59 \times 10^{-5} - 1.83 \times 10^{-5} \ m^3 \cdot mol^{-1}) \qquad (K^+)$$

$$= 0.0983$$

At 298.15 K, concentration of dissolved CO_2 in pure water is 33.95 $mol \cdot m^{-3}$, so concentration of CO_2 in 0.5 M $KHCO_3$ is:

$$\log\left(\frac{33.95}{c_G}\right) = 0.0983, \quad c_G = 27.08 \ mol \cdot m^{-3}$$

The value of c_G is substituted as concentration of dissolved CO_2 in the 0.5 M $KHCO_3$ at 25 °C, $[CO_{2(diss)}]$. Besides, the initial conditions for electrolyte without CO_2 saturated, the concentration of dissolved CO_2 is assumed to be 1 $mol \cdot m^{-3}$. The other dissolved species or ionic species in the electrolyte can specify by using a concentration of dissolved CO_2 in the electrolyte solution and equilibrium constants for the absorption of CO_2 in 0.5 M $KHCO_3$ at 25 °C.

To obtain the initial conditions of dissolved species, the equilibrium constants which performed in neutral to alkaline solution in reactions (23), (26) and (27) are rearranged as Eq. (48) to (50).

$$K_{3.6} = \frac{k_{23f}}{k_{23b}} = \frac{[H^+][HCO_3^-]}{[CO_{2(L)}]} = 4.60 \times 10^{-4} \text{ mol} \cdot \text{m}^{-3} \qquad \text{Eq. (48)}$$

$$K_{3.9} = \frac{k_{26f}}{k_{26b}} = \frac{[CO_3^{2-}]}{[HCO_3^-][OH^-]} = 4.69 \text{ m}^3 \cdot \text{mol}^{-1} \qquad \text{Eq. (49)}$$

$$K_W = [H^+][OH^-] = 1.00 \times 10^8 \text{ m}^6 \cdot \text{mol}^{-2} \qquad \text{Eq. (50)}$$

Rearrange equations as:

$$[H^+][HCO_3^-] = K_{3.6}[CO_{2(L)}] \qquad \text{Eq. (48)}$$

$$[CO_3^{2-}] = K_{3.9}[HCO_3^-][OH^-] \qquad \text{Eq. (49)}$$

$$K_W[H^+][OH^-] = 1 \qquad \text{Eq. (50)}$$

In addition, equations from CO_2 balance and electroneutrality condition are applied to solve the initial condition as following Eq (51) to (53).

$$[CO_{2(diss)}] + [HCO_3^-] = [CO_{2(L)}] + [HCO_3^-] + [CO_3^{2-}] \qquad \text{Eq. (51)}$$

$$[K^+] + [H^+] = [OH^-] + [HCO_3^-] + 2[CO_3^{2-}] \qquad \text{Eq. (52)}$$

$$[K^+] + \frac{K_W}{[OH^-]} = [OH^-] + K_{3.6}[CO_{2(L)}][OH^-] + 2K_{3.6}K_{3.9}[CO_{2(L)}][OH^-]^2 \qquad \text{Eq. (53)}$$

The electroneutrality condition is provided in Eq. (53) is applied for iteration method for solving $[OH^-]$ The initial concentrations of dissolved species are substituted in physics modeling of PEC CO_2 RR as shown in table 13.

Appendix E: The results data for physics model validation and RMSE calculation

The FE of CO_2 conversion to $HCOO^-$ as a function of the cell voltage was compared with the experimental results of I. E. Irem et al [84] as shown in table 16. The MFC configuration with assembling of Sn based GDE cathode as a working-electrode and dimensional stable anode (DSA) as a counter-electrode simulated full cell of electrochemical CO_2 RR to $HCOO^-$ under controlled operating conditions. Similarly operating conditions such as operating temperature and pressure at ambient conditions, pH range of electrolyte in alkaline conditions, and equality of gas to liquid feeding (G/L: 1) were set to achieve the optimum performance of the physics model. The supplied electric of CO_2 conversion to $HCOO^-$ for experimental quantification was as 4 $C\bullet ml^{-1}$ of catholyte. Calculation FE of $HCOO^-$ was used as the performance indicator following Eq. (4).

$$FE(\%) = \frac{e_{output}}{e_{input}} \times 100\%$$

$$= \frac{n\,(mol) \times y}{\frac{Q\,(Coulomb)}{F(\frac{Coulomb}{mol})}} \times 100\% \qquad \text{Eq. (4)}$$

where n = the number of moles of the desired product

y = the number of electrons needed to convert CO_2 into the desired product

Q = the calculated electric charge (Coulomb)

F = the Faraday constant (96485 Coulombs/mols of desired product)

Obviously, the root mean square error (RMSE) is calculated to represent the discrepancy of FE_{HCOO^-} between the experiment and physics model as a function of cell voltage 1.5 to 3.0 V from following Eq. (54).

$$RMSE = \sqrt{\frac{1}{F}\ \sum_{i=1}^{F} (y_i - \hat{y}_i)^2} \qquad \text{Eq. (54)}$$

where RMSE is root mean square error

F is the number of data point

y_i is the actual data or results data from experiment

$\hat{y}_i$ is the predicted value or results data from physics model

Table 16. The results data of CO_2 conversion to $HCOO^-$ as a function of the cell voltage for physics model validation. Volumetric flow rate: 10 ml·min^{-1}.

$|E_{cell}|$ (V)	Current density (mA·cm^{-2})	HCOO$^-$ concentration (mmol·m^{-3})	(mg·L^{-1})	HCOO$^-$ rate (mmol·m^{-2}s^{-1})	FE$_{HCOO^-}$ (%)	FE$_{HCOO^-}$ from experiment (%)	Root means square error (RMSE)
		Physics model					
1.5	2.3	0	0	0	0	0	
1.8	5.0	5.40	0.24	0.04	15.4	20.0	
2.0	8.1	16.60	0.70	0.12	29.3	34.5	
2.1	16.2	48.20	2.17	0.36	42.5	43.0	
2.3	30.9	116.40	5.24	0.86	53.8	55.0	3.36
2.5	68.2	276.70	12.46	2.05	58.0	60.0	
2.8	70.3	350.30	15.77	2.59	71.2	68.5	
3.0	70.6	330.40	14.87	24.45	66.9	65.0	
3.2	70.3	301.10	13.56	2.23	61.2		
3.5	70.0	299.00	13.46	2.21	61.1		

Appendix F: The results data for study variables affecting PEC CO$_2$ RR.

The performance indicators are used to define the effect of variables affecting PEC CO$_2$ RR, calculation of CO$_2$ conversion (X_{CO_2}), selectivity (S), and energy efficiency following Eq. (2), (3), and (5).

$$X_{CO_2} = \frac{F_{CO_2,0} - F_{CO_2}}{F_{CO_2,0}} \qquad \text{Eq. (2)}$$

where $F_{CO_2,0}$ is the initial molar flow rate of CO$_2$ (mol/s)

F_{CO_2} is the final molar flow rate of CO$_2$ (mol/s)

$$S = \frac{\text{Moles formed of interested product}}{\text{Moles formed of overall products}} \qquad \text{Eq. (3)}$$

$$EE(\%) = \frac{\text{Productivity (mol s}^{-1}) \cdot \Delta H^{\circ}_{comb}(\text{J mol}^{-1})}{I_{cell}(A) \cdot E_{cell}(V)} \times 100$$

$$= FE(\%) \times \frac{E_{therm}(V)}{E_{cell}(V)} \qquad \text{Eq. (5)}$$

where ΔH°_{comb} is the combustion energy under standard conditions

E_{therm} is the thermoneutral voltage

Table 17. The combustion energy and thermoneutral voltage of various products at standard conditions [103].

Products	ΔH°_{comb} (kJ mol^{-1})	E_{therm} (V)
HCOO$^-$	254.6	1.32
CO	282.9	1.47
H$_2$	241.8	1.48

Table 18. The results data of different configurations of PEC cells for CO_2 reduction from the physics model simulation with $\phi_{s,bnd,int}$ at 1.5 V and 1.0 mA•cm^{-2} photocurrent density on the TiO_2 photoanode.

PEC cells / Performance indicators		MFC	MEAFC	MFC with a zero-gap anode
HCOO$^-$ concentration (mol•m^{-3})		0.36	0.32	1.78
Current density (mA•cm^{-2})		87.8	69.9	349.8
X_{CO_2}		0.12	0.23	0.17
S	HCOO$^-$	0.60	0.40	0.62
	CO	0.03	0.06	0.03
	H$_2$	0.37	0.54	0.35
FE (%)	HCOO$^-$	58.1	44.9	68.6
	CO	5.7	4.9	6.1
	H$_2$	29.5	49.2	22.3
EE (%)	HCOO$^-$	51.1	39.5	60.4
	CO	5.6	4.8	6.0
	H$_2$	29.1	48.5	22.0

จุฬาลงกรณ์มหาวิทยาลัย

CHULALONGKORN UNIVERSITY

Table 19. The results data of various applied photocurrent density of PEC cells for CO_2 reduction from the physics model simulation with $\phi_{s,bnd,int}$ at 1.5 V photocurrent density on the TiO_2 photoanode.

Performance indicators		Photocurrent density (mA•cm^{-2})					
		0.1	0.5	1.0	5.0	10.0	15.0
Current density (mA•cm^{-2})		154.6	238.1	349.8	350.4	352.9	357.6
X_{CO_2}		0.07	0.14	0.17	0.18	0.19	0.19
S	HCOO$^-$	0.29	0.42	0.60	0.55	0.50	0.41
	CO	0.01	0.02	0.03	0.03	0.03	0.02
	H$_2$	0.70	0.56	0.37	0.42	0.48	0.56
FE (%)	HCOO$^-$	43.5	49.2	68.7	60.0	52.3	37.6
	CO	2.1	4.6	6.1	5.8	5.1	4.9
	H$_2$	44.2	38.4	22.3	31.5	40.1	55.1
EE (%)	HCOO$^-$	38.2	43.3	60.4	52.8	46.0	33.1
	CO	2.1	4.5	6.0	5.7	5.0	4.8
	H$_2$	43.6	37.9	22.0	31.1	39.6	54.4

จุฬาลงกรณ์มหาวิทยาลัย

CHULALONGKORN UNIVERSITY

Table 20. The results data of various length of PEC cells for CO_2 reduction from the physics model simulation with $\phi_{s,bnd,int}$ at 1.5 V and 1.0 mA•cm^{-2} photocurrent density on the TiO_2 photoanode.

Performance indicators		PEC cell length (cm)						
		1.0	1.5	3.0	4.0	6.0	8.0	10.0
Surface area (cm^2)		1.5	2.3	4.5	6.0	9.0	12.0	15.0
Current density (mA•cm^{-2})		376.5	333.8	296.8	254.3	182.3	154.6	154.3
X_{CO_2}		0.11	0.17	0.20	0.20	0.20	0.21	0.21
S	HCOO$^-$	0.64	0.57	0.38	0.28	0.16	0.09	0.05
	CO	0.03	0.03	0.03	0.02	0.02	0.02	0.02
	H$_2$	0.33	0.40	0.59	0.70	0.82	0.89	0.93
FE (%)	HCOO$^-$	71.8	63.3	52.0	47.2	36.1	23.1	13.0
	CO	6.5	6.1	5.8	5.4	4.7	4.5	4.2
	H$_2$	20.4	21.3	26.5	34.2	43.5	56.1	63.2
EE (%)	HCOO$^-$	63.1	55.7	45..8	41.6	31.7	20.3	11.4
	CO	6.4	6.0	5.7	5.3	4.6	4.4	4.1
	H$_2$	20.1	21.0	26.1	33.7	42.9	55.4	62.4

จุฬาลงกรณ์มหาวิทยาลัย

CHULALONGKORN UNIVERSITY

Table 21. The results data of various gas channel width of PEC cells for CO_2 reduction from the physics model simulation with $\phi_{s,bnd,int}$ at 1.5 V and 1.0 mA•cm^{-2} photocurrent density on the TiO_2 photoanode.

Performance indicators		Gas channel width (mm)							
		1.0	1.5	2.0	3.0	4.0	5.0	6.0	8.0
Gas velocity(mm•s^{-1})		11.11	7.41	5.56	3.70	2.78	2.22	1.85	1.39
Current density (mA•cm^{-2})		352.8	349.8	347.8	343.9	341.2	340.2	340.2	340.2
X_{CO_2}		0.17	0.17	0.18	0.20	0.21	0.23	0.24	0.24
S	HCOO$^-$	0.63	0.60	0.57	0.53	0.50	0.45	0.40	0.36
	CO	0.034	0.030	0.029	0.028	0.027	0.027	0.026	0.026
	H$_2$	0.34	0.37	0.40	0.44	0.47	0.52	0.57	0.62
FE (%)	HCOO$^-$	70.1	68.7	65.8	63.2	59.5	51.7	46.6	40.3
	CO	6.5	6.1	5.9	5.8	5.6	5.5	5.4	5.3
	H$_2$	20.6	22.3	25.2	25.1	25.7	26.8	27.5	29.3
EE (%)	HCOO$^-$	61.7	60.4	57.9	55.6	52.4	45.5	41.0	35.5
	CO	6.4	6.0	5.8	5.7	5.5	5.4	5.3	5.2
	H$_2$	20.3	22.0	24.9	24.8	25.4	26.4	27.1	28.9

จุฬาลงกรณ์มหาวิทยาลัย

CHULALONGKORN UNIVERSITY

Table 22. The results data of various electrolyte channel width of PEC cells for CO_2 reduction from the physics model simulation with $\phi_{s,bnd,int}$ at 1.5 V and 10 A•m^{-2} photocurrent density on the TiO_2 photoanode.

Performance indicators		Electrolyte channel width (mm)							
		1.0	1.5	2.0	3.0	4.0	5.0	6.0	8.0
Electrolyte velocity(m•s^{-1})		11.11	7.41	5.56	3.70	2.78	2.22	1.85	1.39
Current density (mA•cm^{-2})		351.8	349.8	347.8	343.5	341.6	340.2	340.2	340.0
X_{CO_2}		0.17	0.17	0.18	0.19	0.19	0.20	0.20	0.21
S	HCOO$^-$	0.65	0.60	0.59	0.53	0.46	0.42	0.36	0.26
	CO	0.03	0.03	0.03	0.03	0.02	0.03	0.02	0.03
	H$_2$	0.32	0.37	0.39	0.45	0.51	0.56	0.61	0.71
FE (%)	HCOO$^-$	70.7	78.7	67.0	60.8	51.1	43.3	35.7	23.5
	CO	6.7	6.1	5.8	5.5	5.5	5.2	5.1	4.3
	H$_2$	20.0	22.3	23.6	26.1	33.5	40.0	45.8	48.6
EE (%)	HCOO$^-$	62.2	60.4	59.0	53.5	44.9	38.1	31.4	20.7
	CO	6.6	6.0	5.7	5.4	5.4	5.1	5.0	4.2
	H$_2$	19.7	22.0	23.3	25.8	33.1	39.5	45.2	48.0

REFERENCES

[1]   A. Mikhaylov, N. Moiseev, K. Aleshin, and T. Burkhardt, "Global climate change and greenhouse effect," *Entrepreneurship and Sustainability Issues,* vol. 7, no. 4, p. 2897, 2020.

[2]   H. R. Roser and Max. "CO_2 and Greenhouse Gas Emissions." @OurWorldInData. https://ourworldindata.org/co2-and-other-greenhouse-gas-emissions (accessed Feb 14, 2022).

[3]   S. Nitopi *et al.,* "Progress and perspectives of electrochemical CO_2 reduction on copper in aqueous electrolyte," *Chemical reviews,* vol. 119, no. 12, pp. 7610-7672, 2019.

[4]   N. Zhang, R. Long, C. Gao, and Y. Xiong, "Recent progress on advanced design for photoelectrochemical reduction of CO_2 to fuels," *Science China Materials,* vol. 61, no. 6, pp. 771-805, 2018, doi: 10.1007/s40843-017-9151-y.

[5]   L. Xu, Y. Xiu, F. Liu, Y. Liang, and S. Wang, "Research Progress in Conversion of CO_2 to Valuable Fuels," *Molecules,* vol. 25, no. 16, Aug 11 2020, doi: 10.3390/molecules25163653.

[6]   V. Kumaravel, J. Bartlett, and S. C. Pillai, "Photoelectrochemical Conversion of Carbon Dioxide (CO_2) into Fuels and Value-Added Products," *ACS Energy Letters,* vol. 5, no. 2, pp. 486-519, 2020, doi: 10.1021/acsenergylett.9b02585.

[7]   E. Kalamaras, M. M. Maroto-Valer, M. Shao, J. Xuan, and H. Wang, "Solar carbon fuel via photoelectrochemistry," *Catalysis Today,* vol. 317, pp. 56-75, 2018, doi: 10.1016/j.cattod.2018.02.045.

[8]   B. Endrodi *et al.,* "Multilayer electrolyzer stack converts carbon dioxide to gas products at high pressure with high efficiency," *ACS energy letters,* vol. 4, no. 7, pp. 1770-1777, 2019.

[9]   N. O. G. A. Schmidt. "Data.GISS: GISTEMP : Additional Analysis Plots." Option:. https://data.giss.nasa.gov/gistemp/graphs_v4/customize.html (accessed Feb 14, 2022).

[10]   Niehs. "Climate Change and Human Health Research." @NIEHS. https://www.ncbi.nlm.nih.gov/pubmed/ (accessed Feb 14, 2022).

[11]   R. Cassia, M. Nocioni, N. Correa-Aragunde, and L. Lamattina, "Climate change and the impact of greenhouse gasses: CO_2 and NO, friends and foes of plant oxidative stress," *Frontiers in plant science,* vol. 9, p. 273, 2018.

[12]   J. Friedrich. "World Greenhouse Gas Emissions: 2018." https://www.wri.org/data/world-greenhouse-gas-emissions-2018 (accessed 14, 2022).

[13]   vizzuality. "| Greenhouse Gas (GHG) Emissions | Climate Watch." https://www.climatewatchdata.org/ghg-emissions?breakBy=gas&end_year=2018&gases=all-ghg&start_year=1990 (accessed Feb 14, 2022).

[14]   e. U. S. E. I. Administration. "Where greenhouse gases come from - U.S. Energy Information Administration (EIA)." U.S. Energy Information Administration (EIA). https://www.eia.gov/energyexplained/energy-and-the-environment/where-greenhouse-gases-come-from.php (accessed Feb 14, 2022).

[15]   O. A. R. Us Epa, "Sources of Greenhouse Gas Emissions," (in en), Overviews and Factsheets 2022-07-27 2022. [Online]. Available: https://www.epa.gov/ghgemissions/sources-greenhouse-gas-emissions.

[16]   S. R. D. Nist Chemistry WebBook. "Carbon dioxide." National Institute of Standards and Technology. https://webbook.nist.gov/cgi/cbook.cgi?ID=C124389&Units=SI (accessed Feb 14, 2022).

[17]   R. A. Tufa *et al.,* "Towards highly efficient electrochemical CO_2 reduction: Cell designs, membranes and electrocatalysts," *Applied Energy,* vol. 277, p. 115557, 2020.

[18]   N. Bhuvanendran, S. Ravichandran, Q. Xu, T. Maiyalagan, and H. Su, "A quick guide to the assessment of key electrochemical performance indicators for the oxygen reduction reaction: A comprehensive review," *International Journal of Hydrogen Energy,* 2022.

[19]   M. Jouny, W. Luc, and F. Jiao, "General techno-economic analysis of CO_2 electrolysis systems," *Industrial & Engineering Chemistry Research,* vol. 57, no. 6, pp. 2165-2177, 2018.

[20] S. Liang, N. Altaf, L. Huang, Y. Gao, and Q. Wang, "Electrolytic cell design for electrochemical CO_2 reduction," *Journal of CO_2 Utilization,* vol. 35, pp. 90-105, 2020.

[21] Technavio. "Carbon Monoxide Alarm Market to Accelerate at a CAGR of Almost 8% During 2021-2025 | Technavio | Business Wire." @businesswire. https://www.businesswire.com/news/home/20210122005188/en/Carbon-Monoxide-Alarm-Market-to-Accelerate-at-a-CAGR-of-Almost-8-During-2021-2025-Technavio (accessed Feb 14, 2022).

[22] M. Jouny, G. S. Hutchings, and F. Jiao, "Carbon monoxide electroreduction as an emerging platform for carbon utilization," *Nature Catalysis,* vol. 2, no. 12, pp. 1062-1070, 2019.

[23] M. R. Future. "Formic Acid Market Size, Share, Growth | Report, 2030." @MRFRresearch. https://www.marketresearchfuture.com/reports/formic-acid-market-1132 (accessed Feb 14, 2022).

[24] S. Castro, J. Albo, and A. Irabien, "Photoelectrochemical Reactors for CO_2 Utilization," *ACS Sustainable Chemistry & Engineering,* vol. 6, no. 12, pp. 15877-15894, 2018/12/03 2018, doi: 10.1021/acssuschemeng.8b03706.

[25] B. M. Tackett, E. Gomez, and J. G. Chen, "Net Reduction of CO_2 via Its Thermocatalytic and Electrocatalytic Transformation Reactions in Standard and Hybrid Processes," *Nat. Catal.,* vol. 2, p. 381, 2019.

[26] X. Jiang, X. Nie, X. Guo, C. Song, and J. G. Chen, "Recent Advances in Carbon Dioxide Hydrogenation to Methanol via Heterogeneous Catalysis," *Chemical Reviews,* vol. 120, no. 15, pp. 7984-8034, 2020/08/12 2020, doi: 10.1021/acs.chemrev.9b00723.

[27] J.-M. Lavoie, "Review on dry reforming of methane, a potentially more environmentally-friendly approach to the increasing natural gas exploitation," *Frontiers in chemistry,* vol. 2, p. 81, 2014.

[28] R. M. Cuéllar-Franca and A. Azapagic, "Carbon capture, storage and utilisation technologies: A critical analysis and comparison of their life cycle environmental impacts," *Journal of CO_2 utilization,* vol. 9, pp. 82-102, 2015.

[29] A. Tavasoli and G. Ozin, "Green syngas by solar dry reforming," *Joule,* vol. 2, no. 4, pp. 571-575, 2018.

[30] L. P., "Radiation Reduction of Carbon Dioxide: A New Chemical Industry?," *Journal of Earth Science & Climate Change" 2020 11.2,* 2020, doi: 10.26434/chemrxiv.12609815.v1.

[31] J. Meng, W. Liao, and G. Zhang, "Emerging CO_2-mineralization technologies for co-utilization of industrial solid waste and carbon resources in China," *Minerals,* vol. 11, no. 3, p. 274, 2021.

[32] C. D. Hills, N. Tripathi, and P. J. Carey, "Mineralization technology for carbon capture, utilization, and storage," *Frontiers in Energy Research,* p. 142, 2020.

[33] X. Chang, T. Wang, and J. Gong, "CO_2 photo-reduction: insights into CO_2 activation and reaction on surfaces of photocatalysts," *Energy & Environmental Science,* 10.1039/C6EE00383D vol. 9, no. 7, pp. 2177-2196, 2016, doi: 10.1039/C6EE00383D.

[34] J. Wu, Y. Huang, W. Ye, and Y. Li, "CO_2 reduction: from the electrochemical to photochemical approach," *Advanced Science,* vol. 4, no. 11, p. 1700194, 2017.

[35] X. Luo, J. Xuan, E. S. Fernandez, and M. M. Maroto-Valer, "Modeling and simulation for PEC CO_2 utilization," *Energy Procedia,* vol. 158, pp. 809-815, 2019, doi: 10.1016/j.egypro.2019.01.213.

[36] Z. Zheng and I. M. Lo, "Multifunctional photoelectrochemical systems for coupled water treatment and high-value product generation: current status, mechanisms, remaining challenges, and future opportunities," *Current Opinion in Chemical Engineering,* vol. 34, p. 100711, 2021.

[37] J. Milano *et al.,* "Microalgae biofuels as an alternative to fossil fuel for power generation," *Renewable and Sustainable Energy Reviews,* vol. 58, pp. 180-197, 2016.

[38] J. Shaya, H. Srour, and I. Karamé, "Introductory Chapter: An Outline of Carbon Dioxide Chemistry, Uses and Technology," in *Carbon dioxide chemistry, capture and oil recovery*: IntechOpen, 2018.

[39]   P. Yaashikaa, P. S. Kumar, S. J. Varjani, and A. Saravanan, "A review on photochemical, biochemical and electrochemical transformation of CO_2 into value-added products," *Journal of CO_2 Utilization,* vol. 33, pp. 131-147, 2019.

[40]   F. E. Bedoya-Lora, A. Hankin, and G. H. Kelsall, "En Route to a Unified Model for Photoelectrochemical Reactor Optimization. II–Geometric Optimization of Perforated Photoelectrodes," (in English), *Frontiers in Chemical Engineering,* Original Research vol. 3, no. 47, 2021-September-10 2021, doi: 10.3389/fceng.2021.749058.

[41]   Y. Yang and F. Li, "Reactor design for electrochemical CO_2 conversion toward large-scale applications," *Current Opinion in Green and Sustainable Chemistry,* vol. 27, 2021, doi: 10.1016/j.cogsc.2020.100419.

[42]   K. P. Kuhl, E. R. Cave, D. N. Abram, and T. F. Jaramillo, "New insights into the electrochemical reduction of carbon dioxide on metallic copper surfaces," *Energy & Environmental Science,* vol. 5, no. 5, pp. 7050-7059, 2012.

[43]   S. Hernandez-Aldave and E. Andreoli, "Fundamentals of gas diffusion electrodes and electrolysers for carbon dioxide utilisation: Challenges and opportunities," *Catalysts,* vol. 10, no. 6, p. 713, 2020.

[44]   C. M. Gabardo *et al.,* "Continuous carbon dioxide electroreduction to concentrated multi-carbon products using a membrane electrode assembly," *Joule,* vol. 3, no. 11, pp. 2777-2791, 2019.

[45]   F. Li *et al.,* "Molecular tuning of CO_2-to-ethylene conversion," *Nature,* vol. 577, no. 7791, pp. 509-513, 2020.

[46]   N. S. Spinner, J. A. Vega, and W. E. Mustain, "Recent progress in the electrochemical conversion and utilization of CO_2," *Catalysis Science & Technology,* vol. 2, no. 1, pp. 19-28, 2012.

[47]   R. Lin, J. Guo, X. Li, P. Patel, and A. Seifitokaldani, "Electrochemical reactors for CO_2 conversion," *Catalysts,* vol. 10, no. 5, p. 473, 2020.

[48]   H. H.-T. Corporation. "Properties of semiconductors : Hitachi High-Tech Corporation." https://www.hitachi-hightech.com/global/en/knowledge/semiconductor/room/about/properties.html (accessed 14 Feb, 2022).

[49]   S. Kaneco, H. Katsumata, T. Suzuki, and K. Ohta, "Photoelectrochemical reduction of carbon dioxide at p-type gallium arsenide and p-type indium phosphide electrodes in methanol," *Chemical Engineering Journal,* vol. 116, no. 3, pp. 227-231, 2006/03/01/ 2006, doi: https://doi.org/10.1016/j.cej.2005.12.014.

[50]   X. Huang, Q. Shen, J. Liu, N. Yang, and G. Zhao, "A CO_2 adsorption-enhanced semiconductor/metal-complex hybrid photoelectrocatalytic interface for efficient formate production," *Energy & Environmental Science,* 10.1039/C6EE00968A vol. 9, no. 10, pp. 3161-3171, 2016, doi: 10.1039/C6EE00968A.

[51]   G. Magesh *et al.*, "A versatile photoanode-driven photoelectrochemical system for conversion of CO_2 to fuels with high faradaic efficiencies at low bias potentials," *Journal of Materials Chemistry A,* 10.1039/C3TA14408A vol. 2, no. 7, pp. 2044-2049, 2014, doi: 10.1039/C3TA14408A.

[52]   d. E. Universitat de Barcelona. Departament d'Enginyeries: Secció *et al.*, "Production of Solar Fuels by Photoelectrochemical Conversion of Carbon Dioxide," (in eng), *TDX (Tesis Doctorals en Xarxa),* info:eu-repo/semantics/publishedVersion 2017-05-04 2017, doi: http://hdl.handle.net/10803/404018.

[53]   Y. W. Song *et al.*, "A study on tandem photoanode and photocathode for photocatalytic formaldehyde fuel cell," *Electrochimica Acta,* vol. 352, 20 August 2020 2020, doi: https://doi.org/10.1016/j.electacta.2020.136476.

[54]   T. Morikawa *et al.*, "Selective CO_2 reduction conjugated with H_2O oxidation utilizing semiconductor/metal-complex hybrid photocatalysts," 2013, doi: https://doi.org/10.1063/1.4848080. [Online]. Available: https://aip.scitation.org/doi/abs/10.1063/1.4848080

[55]   B. Weng, W. Wei, Yiliguma, H. Wu, A. M. Alenizi, and G. Zheng, "Bifunctional CoP and CoN porous nanocatalysts derived from ZIF-67 in situ grown on nanowire photoelectrodes for efficient photoelectrochemical water splitting and CO_2 reduction," *Journal of Materials Chemistry A,* 10.1039/C6TA06841C vol. 4, no. 40, pp. 15353-15360, 2016, doi: 10.1039/C6TA06841C.

[56]   K. Kobayashi, S. N. Lou, Y. Takatsuji, T. Haruyama, Y. Shimizu, and T. Ohno, "Photoelectrochemical reduction of CO_2 using a TiO_2 photoanode and a gas diffusion electrode modified with a metal phthalocyanine catalyst," *Electrochimica Acta,* vol. 338, p. 135805, 2020/04/01/ 2020, doi: https://doi.org/10.1016/j.electacta.2020.135805.

[57]   P. Chakthranont, "Chapter 7 - Photoelectrochemical processes for energy applications," in *Handbook of Nanotechnology Applications*. National Nanotechnology Center (NANOTEC), National Science and Technology

Development Agency (NSTDA), Pathum Thani, Thailand, 2021, ch. 7, pp. 169-194.

[58]   S. Kment *et al.*, "Photoanodes based on TiO_2 and α-Fe_2O_3 for solar water splitting – superior role of 1D nanoarchitectures and of combined heterostructures," *Chemical Society Reviews,* 10.1039/C6CS00015K vol. 46, no. 12, pp. 3716-3769, 2017, doi: 10.1039/C6CS00015K.

[59]   A. Awsha, S. Alazoumi, and B. Elhub, "A Review on the development of TiO2 photoanode for Solar Applications," vol. 2, no. 2, pp. 9-16, 08/01 2021.

[60]   J. Z. Liu, C. Weizheng, H. Fang Xin, Y. Hongbin, and Bin, "Recent advances in single atom catalysts for the electrochemical carbon dioxide reduction reaction," (in en), *Chemical Science,* no. 20, 2021/04/26 2021, doi: 10.1039/D1SC01375K.

[61]   M. Bevilacqua, J. Filippi, H. A. Miller, and F. Vizza, "Recent Technological Progress in CO2 Electroreduction to Fuels and Energy Carriers in Aqueous Environments - Bevilacqua - 2015 - Energy Technology - Wiley Online Library," *Energy Technology,* vol. 3, no. 3, pp. 197-210, 2022, doi: 10.1002/ente.201402166.

[62]   B. Kumar *et al.*, "New trends in the development of heterogeneous catalysts for electrochemical CO2 reduction," *Catalysis Today,* vol. 270, pp. 19-30, 2016, doi: https://doi.org/10.1016/j.cattod.2016.02.006.

[63]   D. Kopljar, A. Inan, P. Vindayer, N. Wagner, and E. Klemm, "Electrochemical reduction of CO_2 to formate at high current density using gas diffusion

electrodes," *Journal of Applied Electrochemistry,* vol. 44, no. 10, pp. 1107-1116, 2014/10/01 2014, doi: 10.1007/s10800-014-0731-x.

[64]   T.-D. Nguyen-Phan *et al.,* "High current density electroreduction of CO_2 into formate with tin oxide nanospheres," *Scientific Reports,* vol. 12, 05/19 2022, doi: 10.1038/s41598-022-11890-6.

[65]   D. H. Weber, H. Christopher, X. Chengxiang, F. J. Thomas, and Z. Adam, "Gas-Diffusion Electrodes for Carbon Dioxide Reduction: A New Paradigm," (in en), *ACs Energy Letters,* review-article December 14, 2018 2018, doi: 10.1021/acsenergylett.8b02035.

[66]   H. R. Yuan, G. Lei, Z. Xueqin, H. Shihu, L. Mengran, and Zhiguo, "Gas diffusion electrodes (GDEs) for electrochemical reduction of carbon dioxide, carbon monoxide, and dinitrogen to value-added products: a review," (in en), *Energy&Environmental Science,* no. 4, 2021/03/04 2021, doi: 10.1039/D0EE03756G.

[67]   Vitobelgium. "Gas diffusion electrodes." https://vito.be/en/product/gas-diffusion-electrodes (accessed Feb 14, 2022).

[68]   H. Rabiee *et al.,* "Regulating the reaction zone of electrochemical CO2 reduction on gas-diffusion electrodes by distinctive hydrophilic-hydrophobic catalyst layers," *Applied Catalysis B: Environmental,* vol. 310, p. 121362, 03/01 2022, doi: 10.1016/j.apcatb.2022.121362.

[69]   K. Wu, E. Birgersson, B. Kim, P. J. A. Kenis, and I. A. Karimi, "Modeling and Experimental Validation of Electrochemical Reduction of CO_2 to CO in a Microfluidic Cell," *Journal of The Electrochemical Society,* vol. 162, no. 1, p. F23, 2014/11/04 2015, doi: 10.1149/2.1021414jes.

[70]   Y. Fu *et al.,* "Novel hierarchical SnO_2 microsphere catalyst coated on gas diffusion electrode for enhancing energy efficiency of CO_2 reduction to formate fuel," *Applied Energy,* vol. 175, pp. 536-544, 2016/08/01/ 2016, doi: https://doi.org/10.1016/j.apenergy.2016.03.115.

[71]   H. Yang, J. Kaczur, S. D. Sajjad, and R. I. Masel, "Electrochemical conversion of CO_2 to formic acid utilizing Sustainion™ membranes," *Journal of CO 2 Utilization,* vol. 20, pp. 208-217, 2017, doi: 10.1016/J.JCOU.2017.04.011.

[72]   J. L. Cheng, Y. Shenglin, Z. Chunxiao, H. Qing, and Zhenmin, "Electroreduction of CO_2 toward High Current Density," *undefined,* 2022. [Online]. Available: https://pdfs.semanticscholar.org/1b9b/8be1dd1337e91c4238e08cf2b9e19696f c12.pdf.

[73]   M. d. S. P. M. and Kortlever, "Electrolyte Effects on the Electrochemical Reduction of CO_2," *Chemphyschem : a European journal of chemical physics and physical chemistry,* vol. 20, no. 22, pp. 2926-2935, 11/19/2019 2019, doi: 10.1002/cphc.201900680.

[74]   Q. Wang, H. Dong, and H. Yu, "Development of rolling tin gas diffusion electrode for carbon dioxide electrochemical reduction to produce formate in aqueous electrolyte," *Journal of Power Sources,* vol. 271, pp. 278-284, 2014/12/20/ 2014, doi: https://doi.org/10.1016/j.jpowsour.2014.08.017.

[75]   S. V. Kenis, L. Xun, M. Sichao, I. M. Richard, and J. A. Paul, "The effect of electrolyte composition on the electroreduction of CO_2 to CO on Ag based gas diffusion electrodes," (in en), *Physical Chemistry Chemical Physiccs,* no. 10, 2015/11/23 2016, doi: 10.1039/C5CP05665A.

[76]   J.-B. Vennekötter, T. Scheuermann, R. Sengpiel, and M. Wessling, "The electrolyte matters: Stable systems for high rate electrochemical CO_2 reduction," *Journal of CO_2 Utilization,* vol. 32, pp. 202-213, 2019, doi: https://doi.org/10.1016/j.jcou.2019.04.007.

[77]   J. Resasco *et al.,* "Promoter Effects of Alkali Metal Cations on the Electrochemical Reduction of Carbon Dioxide," *Journal of the American Chemical Society,* vol. 139, no. 32, pp. 11277-11287, 2017/08/16 2017, doi: 10.1021/jacs.7b06765.

[78]   S. Sato, K. Saita, K. Sekizawa, S. Maeda, and T. Morikawa, "Low-Energy Electrocatalytic CO_2 Reduction in Water over Mn-Complex Catalyst Electrode Aided by a Nanocarbon Support and K^+ Cations," *ACS Catalysis,* vol. 8, pp. 4452-4458, 2018, doi: 10.1021/ACSCATAL.8B01068.

[79]   S. S. Bhargava *et al.,* "System Design Rules for Intensifying the Electrochemical Reduction of CO_2 to CO on Ag Nanoparticles," *ChemElectroChem,* vol. 7, no. 9, pp. 2001-2011, 2020, doi: https://doi.org/10.1002/celc.202000089.

[80] M. N. Jackson, O. Jung, H. C. Lamotte, and Y. Surendranath, "Donor-Dependent Promotion of Interfacial Proton-Coupled Electron Transfer in Aqueous Electrocatalysis," *ACS Catalysis,* vol. 9, no. 4, pp. 3737-3743, 2019/04/05 2019, doi: 10.1021/acscatal.9b00056.

[81] Y. Kotb, S.-E. K. Fateen, J. Albo, and I. Ismail, "Modeling of a Microfluidic Electrochemical Cell for the Electro-Reduction of CO_2 to CH_3OH," *Journal of The Electrochemical Society,* vol. 164, no. 13, pp. E391-E400, 2017, doi: 10.1149/2.0741713jes.

[82] W. Lu, Y. Zhang, J. Zhang, and P. Xu, "Reduction of gas CO_2 to CO with high selectivity by Ag nanocube-based membrane cathodes in a photoelectrochemical system," *Industrial & Engineering Chemistry Research,* vol. 59, no. 13, pp. 5536-5545, 2020.

[83] A. C. Offong, E. J. Anthony, and V. Manovic. "Modelling and Simulating CO_2 Electro-Reduction to Formic Acid using MEC- Microfluidic Electrolytic Cells." https://www.comsol.com/paper/modelling-and-simulating-co2-electro-reduction-to-formic-acid-using-mec-microflu-82001 (accessed Feb 10, 2022).

[84] E. Irtem *et al.,* "A photoelectrochemical flow cell design for the efficient CO_2 conversion to fuels," *Electrochimica Acta,* vol. 240, pp. 225-230, 2017, doi: 10.1016/j.electacta.2017.04.072.

[85] S. Castro, J. Albo, and A. Irabien, "Continuous conversion of CO_2 to alcohols in a TiO_2 photoanode-driven photoelectrochemical system," *Journal of Chemical Technology & Biotechnology,* vol. 95, no. 7, pp. 1876-1882, 2020.

[86] T. Arai, S. Tajima, S. Sato, K. Uemura, T. Morikawa, and T. Kajino, "Selective CO_2 conversion to formate in water using a CZTS photocathode modified with a ruthenium complex polymer," *Chem. Commun.,* vol. 47, p. 12664, 2011.

[87] F. e. Store. "CT Carbon Cloth without MPL - W0S1009." https://www.fuelcellstore.com/carbon-cloth-without-mpl (accessed 14 Feb, 2022).

[88] F. C. Etc. "Nafion™ Membrane Comparison Table." https://fuelcellsetc.com/helpful-tools/nafion-membrane-comparison-table/ (accessed Feb 14, 2022).

[89]   T. E. ToolBox. "Gases - Dynamic Viscosities." https://www.engineeringtoolbox.com/gases-absolute-dynamic-viscosity-d_1888.html (accessed 14 Feb, 2022).

[90]   PubChem. "Carbon Dioxide." https://www.ncbi.nlm.nih.gov/pubmed/ (accessed 14 Feb, 2022).

[91]   T. E. ToolBox. "Carbon dioxide - Density and Specific Weight vs. Temperature and Pressure." https://www.engineeringtoolbox.com/carbon-dioxide-density-specific-weight-temperature-pressure-d_2018.html (accessed 14 Feb, 2022).

[92]   N. Gupta, M. Gattrell, and B. MacDougall, "Calculation for the cathode surface concentrations in the electrochemical reduction of CO2 in KHCO3 solutions," *Journal of Applied Electrochemistry,* vol. 36, no. 2, pp. 161-172, 2006/02/01 2006, doi: 10.1007/s10800-005-9058-y.

[93]   Y.-j. Guo, H.-b. Xu, F. Guo, S.-l. Zheng, and Y. Zhang, "Density and viscosity of aqueous solution of K_2CrO_4/KOH mixed electrolytes," *Transactions of Nonferrous Metals Society of China,* vol. 20, pp. s32-s36, 2010/05/01/ 2010, doi: https://doi.org/10.1016/S1003-6326(10)60007-6.

[94]   T. E. ToolBox. "Densities of Aqueous Solutions of Inorganic Potassium Salts." https://www.engineeringtoolbox.com/density-aqueous-solution-inorganic-potassium-salt-concentration-d_1956.html (accessed 14 Feb, 2022).

[95]   J. He and C. Janaky, "Recent Advances in Solar-Driven Carbon Dioxide Conversion: Expectations versus Reality," *ACS Energy Lett.,* vol. 5, no. 6, p. 1996, 2020.

[96]   N. Gadgil, "Modeling a Flow-Cell for Electrochemical Reduction of Carbon Dioxide to Formate," Delft University of Technology, TU Delft Mechanical, Maritime and Materials Engineering, The Delft University of Technology, 2018. [Online]. Available: http://resolver.tudelft.nl/uuid:885c941e-f98a-4761-9e09-c62071773af5

[97]   R. Kas, K. Yang, G. P. Yewale, A. Crow, T. Burdyny, and W. A. Smith, "Modeling the Local Environment within Porous Electrode during Electrochemical Reduction of Bicarbonate," *Industrial & Engineering Chemistry Research,* vol. 61, no. 29, pp. 10461-10473, 2022/07/27 2022, doi: 10.1021/acs.iecr.2c00352.

[98]   A. B. Yaroslavtsev, Y. A. Dobrovolsky, N. S. Shaglaeva, L. A. Frolova, E. V. Gerasimova, and E. A. Sanginov, "Nanostructured materials for low-temperature fuel cells†," *Russian Chemical Reviews,* vol. 81, no. 3, p. 191, 2012/03/31 2012, doi: 10.1070/RC2012v081n03ABEH004290.

[99]   M. Umeda, K. Sayama, T. Maruta, and M. Inoue, "Proton activity of Nafion 117 membrane measured from potential difference of hydrogen electrodes," *Ionics,* vol. 19, no. 4, pp. 623-627, 2013/04/01 2013, doi: 10.1007/s11581-012-0791-z.

[100]   N. Chaisubanan, K. Pruksathorn, H. Vergnes, and M. Hunsom, "Effect of the TiO_2 phase and loading on oxygen reduction reaction activity of PtCo/C catalysts in proton exchange membrane fuel cells," *Korean Journal of Chemical Engineering,* vol. 32, no. 7, pp. 1305-1313, 2015/07/01 2015, doi: 10.1007/s11814-014-0340-8.

[101]   A. Behrendt *et al.*, "Highly Robust Transparent and Conductive Gas Diffusion Barriers Based on Tin Oxide," *Advanced Materials,* vol. 27, no. 39, pp. 5961-5967, 2015, doi: https://doi.org/10.1002/adma.201502973.

[102]   P. E. s. Tools, "Molecular masses table of common gases," 2022. [Online]. Available:https://powderprocess.net/Tools_html/Data_Diagrams/Tools_Molecular_weight.html.

[103]   M. R. Singh, E. L. Clark, and A. T. Bell, "Thermodynamic and achievable efficiencies for solar-driven electrochemical reduction of carbon dioxide to transportation fuels," *Proceedings of the National Academy of Sciences,* vol. 112, no. 45, pp. E6111-E6118, 2015, doi: doi:10.1073/pnas.1519212112.

VITA

NAME	Aroonroj Chaosukho
DATE OF BIRTH	17 March 1998
PLACE OF BIRTH	Sakon Nakhon, Thailand
INSTITUTIONS ATTENDED	Chulalongkorn University
HOME ADDRESS	250 Village No. 4, Dong Phatthana Village, That Na Weng Sub-district, Mueang Sakon Nakhon District, Sakon Nakhon, 47000

จุฬาลงกรณ์มหาวิทยาลัย
CHULALONGKORN UNIVERSITY